NUMERICAL SIMULATION OF PRECAST CONCRETE LOAD-BEARING WALLS EXPOSED TO FIRE

Mr. Soklin Chou

A Dissertation Submitted in Partial Fulfillment of the Requirements
for the Degree of Doctor of Philosophy Program in Civil Engineering
Department of Civil Engineering
Faculty of Engineering
Chulalongkorn University
Academic Year 2014

การจำลองเชิงตัวเลขของผนังคอนกรีตหล่อสำเร็จรองรับน้ำหนักบรรทุกที่สัมผัสเพลิงไหม้

นายซกลิน ชู

วิทยานิพนธ์นี้เป็นส่วนหนึ่งของการศึกษาตามหลักสูตรปริญญาวิศวกรรมศาสตรดุษฎีบัณฑิต
สาขาวิชาวิศวกรรมโยธา ภาควิชาวิศวกรรมโยธา
คณะวิศวกรรมศาสตร์ จุฬาลงกรณ์มหาวิทยาลัย
ปีการศึกษา 2557

Thesis Title	NUMERICAL SIMULATION OF PRECAST CONCRETE LOAD-BEARING WALLS EXPOSED TO FIRE
By	Mr. Soklin Chou
Field of Study	Civil Engineering
Thesis Advisor	Associate Professor Thanyawat Pothisiri, Ph.D.
Thesis Co-Advisor	Associate Professor Anil C. Wijeyewickrema, Ph.D.

Accepted by the Faculty of Engineering, Chulalongkorn University in Partial Fulfillment of the Requirements for the Doctoral Degree

.....Dean of the Faculty of Engineering
(Professor Bundhit Eua-arporn, Ph.D.)

THESIS COMMITTEE

.....Chairman
(Professor Thaksin Thepchatri, Ph.D.)

.....Thesis Advisor
(Associate Professor Thanyawat Pothisiri, Ph.D.)

.....Thesis Co-Advisor
(Associate Professor Anil C. Wijeyewickrema, Ph.D.)

.....Examiner
(Assistant Professor Withit Pansuk, Ph.D.)

.....External Examiner
(Assistant Professor Taweechai Sumranwanich, Ph.D.)

ซกลิน ชู : การจำลองเชิงตัวเลขของผนังคอนกรีตหล่อสำเร็จรองรับน้ำหนักบรรทุกที่สัมผัสเพลิงไหม้ (NUMERICAL SIMULATION OF PRECAST CONCRETE LOAD-BEARING WALLS EXPOSED TO FIRE) อ.ที่ปรึกษาวิทยานิพนธ์หลัก: ธัญวัฒน์ โพธิศิริ, อ.ที่ปรึกษาวิทยานิพนธ์ร่วม: เอนิล ไวเจวิเครมา, 110 หน้า.

งานวิจัยนี้ศึกษาสมรรถนะของผนังคอนกรีตหล่อสำเร็จรองรับน้ำหนักบรรทุกที่สัมผัสเพลิงไหม้โดยใช้แบบจำลองเชิงความร้อนและแบบจำลองโครงสร้าง 3 มิติ โดยที่แบบจำลองเชิงความร้อนใช้ในการวิเคราะห์การเปลี่ยนแปลงอุณหภูมิซึ่งพิจารณาให้กระทำต่อแบบจำลองโครงสร้างในรูปของแรงภายในเนื่องจากความร้อนเพื่อทำนายการกระจัด รูปแบบการแตกร้าว และเสถียรภาพของผนัง การตรวจสอบความถูกต้องของแบบจำลองเชิงความร้อนดำเนินการโดยเปรียบเทียบค่าอุณหภูมิที่ได้จากแบบจำลองกับข้อมูลจากการทดสอบอัตราการทนไฟ รวมทั้งงานวิจัยที่ผ่านมา ในขณะที่การตรวจสอบความถูกต้องของแบบจำลองโครงสร้างดำเนินการโดยเปรียบเทียบค่าการกระจัดและรูปแบบการแตกร้าวที่ทำนายได้กับข้อมูลจากการทดสอบอัตราการทนไฟ จากการศึกษาพบว่าผลที่ได้จากแบบจำลองเชิงความร้อนและแบบจำลองโครงสร้างสอดคล้องกับข้อมูลการทดสอบ แบบจำลองที่ได้ผ่านการตรวจสอบความถูกต้องแล้วถูกนำมาใช้สำหรับการศึกษาผลกระทบของระดับน้ำหนักบรรทุก อัตราส่วนชะลูด และเงื่อนไขขอบเขต ต่อสมรรถนะการทนไฟของผนัง ซึ่งจากการศึกษาพบว่าอัตราการทนไฟของผนังที่มีความหนา 120 มม. ลดลงสูงสุดถึง 90% ภายใต้แรงกระทำที่เพิ่มขึ้น และลดลงสูงสุดถึง 93% เมื่อเพิ่มอัตราส่วนชะลูด ในขณะที่อัตราการทนไฟของผนังเพิ่มขึ้นสูงสุดถึง 94% เมื่อมีการเหนี่ยวรั้งเชิงการหมุนที่บริเวณปลายของผนัง โดยที่งานวิจัยนี้ได้นำเสนอสมการอย่างง่ายสำหรับการประมาณค่าอัตราการทนไฟของผนังโดยใช้วิธีกำลังสองน้อยสุด สุดท้ายนี้ งานวิจัยนี้ได้ศึกษาสมรรถนะการทนไฟของผนังที่มีการเหนี่ยวรั้งแบบไม่สมมาตรและผนังที่มีช่องเปิด ซึ่งจากการศึกษาพบว่าการกระจัดตามแนวราบที่กึ่งกลางผนังซึ่งมีฐานรองรับอย่างง่ายมีค่าลดลงสูงสุดถึง 6% เมื่อมีการเหนี่ยวรั้งเพิ่มเติมบนขอบผนังตามแนวดิ่งหนึ่งด้าน และมีค่าเพิ่มขึ้นสูงสุดถึง 36% เมื่อผนังมีช่องเปิด ดังนั้นจึงควรมีการศึกษาเพิ่มเติมถึงผลกระทบของการเหนี่ยวรั้งแบบไม่สมมาตร และช่องเปิดของผนังในรูปแบบต่างๆ

ภาควิชา วิศวกรรมโยธา ลายมือชื่อนิสิต .....

สาขาวิชา วิศวกรรมโยธา ลายมือชื่อ อ.ที่ปรึกษาหลัก .....

ปีการศึกษา 2557 ลายมือชื่อ อ.ที่ปรึกษาร่วม .....

5471461021 : MAJOR CIVIL ENGINEERING
KEYWORDS: FIRE RESISTANCE / PRECAST CONCRETE / LOAD-BEARING WALLS / FINITE ELEMENT MODEL

SOKLIN CHOU: NUMERICAL SIMULATION OF PRECAST CONCRETE LOAD-BEARING WALLS EXPOSED TO FIRE. ADVISOR: ASSOC. PROF. THANYAWAT POTHISIRI, Ph.D., CO-ADVISOR: ASSOC. PROF. ANIL C. WIJEYEWICKREMA, Ph.D., 110 pp.

The performance of precast concrete load-bearing walls exposed to fire is investigated using 3-D thermal and structural models. The thermal model is used to obtain the temperature history, which is input as the thermal body load for the structural model in order to predict displacements, crack patterns and stability of the wall. The thermal model is validated by comparing the predicted temperatures with measured data from the fire tests and previous experimental studies, while the structural model is verified by comparing the predicted displacements and crack patterns with those taken from the fire tests. It is found that the results obtained from the thermal and the structural models are in line with the experimental data. The validated model is used to study the effect of load levels, slenderness ratios and boundary conditions on the fire performance of the walls. It is found that the fire resistance rating of the 120 mm thick load-bearing walls decreases by up to 90% with increasing load levels and 93% with increasing slenderness ratios, while the fire resistance rating of the walls increases by up to 94% when the rotational restraints are imposed at the ends of the walls. Simplified equations are also derived for estimating the fire resistance rating of the walls based on the least-squares method. Finally, the fire performance of walls with unsymmetrical restraints and openings are investigated. It is found that the horizontal displacements of the simply supported wall decrease by up to 6% at the center of the wall when the translational restraint is imposed on a vertical edge and increase by up to 36% at the center of the wall when a wall opening is included. Further studies are recommended to investigate the effects of unsymmetrical restraints and openings on the walls with varying configurations.

Department:	Civil Engineering	Student's Signature	.....
Field of Study:	Civil Engineering	Advisor's Signature	.....
Academic Year:	2014	Co-Advisor's Signature	.....

ACKNOWLEDGEMENTS

First and foremost I would like to express my sincerest and deepest gratitude to my advisor, Associate Professor Dr. Thanyawat Pothisiri, for his excellent guidance, encouragement, assistance and constant support throughout my research work at Chulalongkorn University. I also wish to express my great appreciation and gratitude to my co-advisor, Associate Professor Dr. Anil C. Wijeyewickrema for his kindness and invaluable advice on my research work during my short term study at Tokyo Institute of Technology (TIT) from August 2013 to March 2014.

I would like to express my sincere gratitude to ASEAN University Network-Southeast Asia Engineering Education Development Network Project (AUN/SEED-Net) for providing me the financial support to pursue a Doctoral Degree in Civil Engineering in the field of Structural Engineering at Chulalongkorn University.

My sincere thanks are also extended to all committee members, namely, Professor Dr. Thaksin Thepchatri, Assistant Professor Dr. Withit Pansuk, Assistant Professor Dr. Taweechai Sumranwanich for their invaluable suggestions and comments on my research work.

Finally, I would like to thank my parents, my brothers and my wife, for their endless love and efforts that encouraged me to succeed in this research work.

CONTENTS

Page

Page

Page

LIST OF TABLES

Page

LIST OF FIGURES

CHAPTER 1
INTRODUCTION

1.1 Background

Precast concrete load-bearing walls have been widely used in building construction due to the advantages in light weight, low on–site labor cost and high level of quality control. In the event of fire, precast concrete walls can also serve as a fire barrier as shown in Figure 1.1 (a) (Lie and Kodur 1996). The dominant factors that affect the performance of a wall exposed to fire are the thermal, physical and chemical properties of the materials (i.e., concrete and reinforcing steel), the dimensions of the wall, the end restraints and the loading condition. The function of a precast concrete load-bearing wall in a fire situation is generally seen to be threefold. Firstly, a precast concrete load-bearing wall must preserve structural stability to prevent collapse. Secondly, the wall is required to maintain integrity, i.e. preventing the spread of flame from one side of the wall to the other side. Finally, the wall must provide adequate insulation to prevent excessive temperature rise on the unexposed face.

For the separation elements, such as concrete walls, one side of the elements is usually exposed to fire. Because of the low thermal conductivity of concrete, thermal gradients tend to be produced over the cross-section of the walls causing differential thermal expansion and thermal bowing. Since the exposed face of the wall expands more quickly than the unexposed side, the wall tends to bow toward the fire as can be seen in Figure 1.1(b). The degradation of material properties on the fire exposed face of the walls can be considered as the reduction in thickness of the heated surface. The change in thickness of the walls is recognized as having the advantageous effect of maintaining structural stability by counteracting thermal bowing due to the shift of the applied load to the fire exposed face (Cooke and Morgan 1988).

The increasing deformation caused by additional moment from the applied load to that from thermal bowing can induce geometrical nonlinearity. The incorporation of this geometrical nonlinearity with the reduction of mechanical properties of materials at elevated temperatures complicates the evaluation of the fire

resisting performance of precast concrete load-bearing walls. In order to examine the performance of precast concrete load-bearing walls exposed to fire with respect to different parameters, e.g. support conditions, slenderness ratios, and load levels, numerical simulation can be adopted as a powerful tool as an alternative to extensive experimental investigations.

Numerical simulation of precast concrete load-bearing walls exposed to fire involves analyses of time-dependent temperatures and structural stability of the walls by using thermal and structural models. The key concerns in the thermal model are the variation of thermal properties of concrete and steel rebar at elevated temperatures while in the structural model the degradation of mechanical properties of the materials needs to be taken into account.

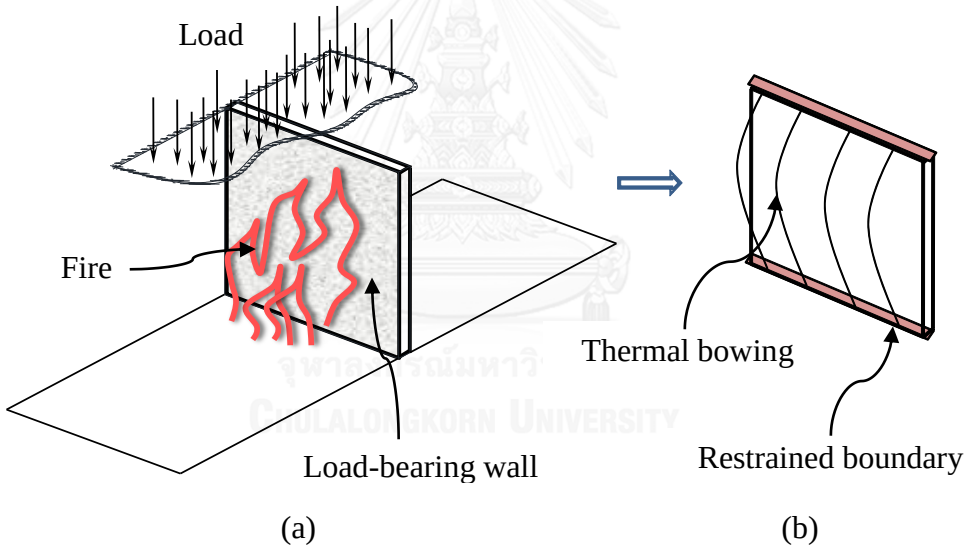

Figure 1.1: (a) Functions of a wall in a fire, (b) Thermal bowing toward the fire.

1.2 Statement of Research Problem

The precast concrete walls used as building elements in buildings are required to maintain the structural stability and integrity in the event of fire to allow the building occupants with sufficient time to escape. A number of experimental studies have been conducted on the performance of concrete walls exposed to fire (Crozier and Sanjayan 2000, Guerrieri and Fragomeni 2010, Go, Tang et al. 2012, Lee and Lee 2013). However, the results are highly dependent on the experimental set up and the size of the wall specimens is limited to fit the furnace, which may not represent the actual walls used in practice. Theoretical models have also been proposed in the literature for reinforced concrete walls with one-sided fire exposure (O'Meagher and Bennetts 1991, Lim 2000). The model proposed by O'Meagher and Bennetts (1991) is capable of taking into account material as well as geometric nonlinearity, while the model proposed by Lim (2000) can incorporate material nonlinearity. However, both models are based on the two dimensional analysis which cannot capture the out-of-plane behavior of the walls exposed to fire.

1.3 Research Objectives

The current study is aimed to create a three dimensional model to predict the structural behavior of precast concrete load-bearing walls exposed to fire with respect to several varying parameters, such as load levels, slenderness ratios and boundary conditions. Experimental results are used to verify the efficacy of the proposed model.

1.4 Scope of Research

In order to examine the behavior of precast concrete load-bearing walls at elevated temperatures, three-dimensional thermal and structural models are created using a commercial finite-element program ANSYS. The thermal model is employed to capture the temperature distribution within the wall with respect to time. The temperature history obtained from the thermal model is used as input for the structural model to evaluate displacements, cracking and the structural stability of the walls. The models are verified against the experimental data by comparing the predicted temperatures, displacements and crack patterns with the measured ones from the fire

test. Parametric studies are carried out for walls with varying boundary conditions, slenderness ratios and load levels. A set of simplified equations is also derived by using the data obtained from the proposed model in order to estimate the fire resistance rating of the walls based on the load levels and slenderness ratios. Finally, further capabilities of the proposed model are illustrated for walls with unsymmetrical restraint and opening.

1.5 Research Methodology

The framework of this study includes numerical and experimental studies on the behavior of precast concrete load-bearing wall exposed to fire. The research method can be summarized as follows:

(i) Review previous theoretical and experimental studies related to the behavior of non-load bearing or load-bearing concrete walls exposed to fire, e.g. cracking and crushing of concrete, failure modes, thermal and mechanical properties of concrete and steel rebar, etc.

(ii) Conduct the fire tests on two full scale walls in order to obtain the temperature distribution, horizontal displacements, and crack patterns of the walls. The experimental data will be used to validate the proposed model.

(ii) Create a thermal model for predicting the temperature distribution inside the wall with respect to time and validate the model by comparing the estimated temperatures with the measured ones as well as those from the previous studies.

(iii) Create a structural model in which the temperature history obtained from the thermal model is used as the thermal body load. The structural model is validated by comparing the predicted horizontal displacements and crack patterns with the experimental data obtained from the fire tests.

(iv) Derive a set of simplified equations for estimating the fire resistance rating of the walls with varying load levels and slenderness ratios. The simplified equations are obtained based on the least-squares method.

(v) Illustrate further capabilities of the model in dealing with unsymmetrical restraints and wall openings.

1.6 Research Significance

A three dimensional model for precast concrete load-bearing walls exposed to fire has been proposed in the current study. The model is capable of taking into account material and geometric nonlinearity, as well as unsymmetrical boundaries and wall openings. The model has been validated against the experimental data for its efficacy in predicting the temperature distribution, horizontal displacements and crack patterns of precast concrete load-bearing walls with one-sided fire exposure. Based on the proposed model, simplified equations have been derived for predicting the fire resistance of concrete load-bearing walls with different boundary conditions. The proposed model is deemed a more efficient alternative to extensive experimental investigations.

1.7 Outline of Dissertation

This dissertation is divided into six chapters as described below.

Chapter 1 introduces the functions of the precast concrete load-bearing walls in the event of fire; and states the research problem, the research objective, the research scope, the research methodology and the research significance.

Chapter 2 provides an extensive literature review on numerical and experimental studies on load-bearing and non-load bearing concrete walls exposed to fire, finite element modeling of RC beams, composite beam-slab assemblies and bridge girders exposed to fire using ANSYS, and thermal and mechanical properties of concrete and steel rebar.

Chapter 3 describes the proposed finite element model; presents thermal and mechanical properties, and material modeling of concrete and steel rebar which are

implemented in ANSYS; and illustrates the 3-D elements used to model concrete and steel rebar, as well as the loading and boundary conditions imposed at the walls.

Chapter 4 describes the fire tests conducted on the precast concrete load-bearing walls which are used to validate the proposed model and the convergence check of the finite element model; describes the thermal model and its validation by comparing the predicted temperatures with the measured data obtained from the fire tests and the previous studies; and describes the structural model and its validation by comparing the predicted horizontal displacements and crack patterns of the walls with those taken during the fire test.

Chapter 5 examines the effect of load level, slenderness ratio and boundary condition on the fire performance of the walls; presents the simplified equations for estimating the fire resistance rating of the walls based on the load level and slenderness ratio for different boundary conditions, i.e. walls with no rotational restraint, walls with one end fixed and walls with both ends fixed; examines the effect of wall thickness; and presents further capabilities of the model in handling unsymmetrical restraint and opening.

Chapter 6 presents the conclusions; describes the limitations of the present study; and provides recommendations for future research.

CHAPTER 2
LITERATURE REVIEW

2.1 Behavior of Reinforced Concrete Walls at Elevated Temperatures

O'Meagher and Bennetts (1991) have developed a theoretical fiber model for analyzing reinforced concrete walls with one-sided fire exposure. The model can incorporate material as well as geometric nonlinearity. Their theoretical study shows that the behavior of the reinforced concrete walls exposed to fire on one side is significantly influenced by height to thickness ratio, amount and location of reinforcement and end restraint. The load capacity of the walls reduces significantly with the increasing height to thickness ratio while the walls with greater cover to reinforcement perform better.

Crozier and Sanjayan (2000) have tested eighteen large–scale slenderness reinforced concrete walls exposed to fire on one side. Based on their experimental results, centrally reinforced walls with the same amount of reinforcement behave better in fire than the doubly reinforced walls. Further, walls with smaller thermal bowing due to smaller in-plane load perform better than the ones with larger thermal bowing due to larger in-plane load. The authors have also concluded that concrete spalling is more likely to occur on the fire-exposed surface of the walls with little or no flexural cracking than the ones with significant flexural cracking while the concrete strength seems to have little influence on the in-plane load capacity of the walls.

Lim (2000) has conducted a theoretical investigation on the behavior of slender cantilever concrete walls and concrete walls in steel frames (propped cantilever walls) exposed to elevated temperatures on one side. The analysis was carried out using finite element program SAFIR. It has been found that the fire performance of slender cantilever concrete walls is very sensitive to their slenderness ratios. The slender cantilever walls with higher slenderness ratios show larger deflection as a result of thermal bowing and P-delta effects.

Guerrieri and Fragomeni (2010) have conducted standard fire tests on four slender concrete walls subjected to one-sided fire exposure. The experimental study shows that explosive spalling occur on the walls loaded by only their own weight while no spalling occur on the walls loaded by their own weight and in-plane load. The results also show that the pore pressure build-up and the flexural cracking are very sensitive to the support conditions of the walls.

Go, Tang et al. (2012) have conducted an experimental study on the fire resistance of reinforced lightweight aggregate concrete walls. The fire resistance performance and mechanical behavior of the reinforced lightweight aggregate concrete walls are investigated under a lateral horizontal load. The experimental results show that the reinforced lightweight aggregate concrete wall is superior to the reinforced normal weight aggregate concrete wall in terms of yield load, ultimate load, crack load, stiffness, ductility and inter-story drift after the fire-resistance test. In addition, the smaller the steel spacing in lightweight aggregate concrete the higher yielding and ultimate strength and the lower ductility.

Lee and Lee (2013) have carried out an experimental and theoretical investigation on the fire resistance of concentrically loaded reinforced concrete walls exposed to fire on both sides. The results from their theoretical study show that the fire resistance of the concrete walls is significantly affected by the wall thickness and the load level rather than by the concrete compressive strength and the vertical reinforcement ratio.

Previous studies (Hawileh, Naser et al. 2009, Hawileh and Naser 2012, Aziz and Kodur 2013, Kodur, Naser et al. 2013) have investigated the response of RC beams, composite beam-slab assemblies and bridge girders exposed to fire using finite element program ANSYS. Nevertheless, there has been virtually no study on modeling RC walls exposed to fire taking into account the out-of-plane structural behavior. Therefore, the current research proposes to develop a three dimensional model of precast concrete load-bearing walls exposed to fire by using ANSYS. The model is aimed to be capable of taking into account the effect of varying support conditions, slenderness ratios and load levels.

In order to evaluate the behavior of concrete load-bearing walls exposed to fire, the properties of concrete and reinforcing steel at elevated temperatures are required to be used as input in the numerical models.

2.2 Concrete at Elevated Temperatures

Concrete has been widely used as a primary structural material in construction due mainly to its durability, strength, ease of fabrication and noncombustibility. Furthermore, concrete generally provides excellent fire resistance due to a chemical combination of cement, water and aggregates to form a material that is inert and has low thermal conductivity, high heat capacity and slow strength degradation (Kodur and Raut 2010).The fire response of concrete structures is influenced by the thermal and mechanical properties of the material. These properties vary as a function of temperature and depend on the characteristics and composition of concrete. The material properties at elevated temperatures and a defined temperature-time exposure allow numerical models to evaluate the temperature distribution, the fire resistance and the behavior of concrete members (Kodur, Wang et al. 2004, Hawileh, Naser et al. 2009, Hawileh and Naser 2012, Aziz and Kodur 2013, Kodur, Naser et al. 2013).

2.2.1 Thermal Properties of Concrete

The thermal properties that govern the temperature distribution and rise in the concrete structures are thermal conductivity, specific heat and density. These properties depend mainly on the aggregate type, moisture content, and composition of concrete mix. Many researchers (Lie and Kodur 1995, Van Geem, Gajda et al. 1997, Shin, Kim et al. 2002, Kodur and Sultan 2003, Eurocode2 2004) have conducted the fire tests to characterize the thermal properties of concrete at elevated temperatures. For the current study the thermal conductivity, specific heat and density of concrete based on Eurocode2 (2004) are adopted.

The thermal conductivity of concrete is significantly influenced by its moisture content, type of aggregate, test conditions, and measurement techniques used in experiments (Harmathy and Allen 1973, Schaffer 1992, Bazant and Kaplan 1996,

Phan 1996, Kodur and Sultan 2003). Eurocode2 (2004) has proposed lower and upper limit equations to determine the thermal conductivity that accounts for these factors. At room temperature, the thermal conductivity of conventional normal strength concrete (NSC) is in the range of 1.4 and 3.6 W/m-K while at elevated temperature the thermal conductivity of concrete decreases gradually (Bazant and Kaplan 1996).

Specific heat is often expressed in terms of thermal capacity which is the product of specific heat and density. The specific heat of concrete is significantly influenced by the aggregate type, moisture content and density (Harmathy and Allen 1973, Phan 1996, Kodur and Sultan 1998). Furthermore, the specific heat is sensitive to various chemical and physical transformations in concrete at elevated temperatures–i.e., the vaporization of free water at about 100 ^{o}C, the dissociation of $Ca(OH)_2$ into CaO and H_2O between 400–500 ^{o}C, and the quartz transformation of some aggregates above 600 ^{o}C (Harmathy 1970). In addition, the specific heat mainly depends on moisture content and considerably increases with higher water to cement ratio. According to Schaffer (1992), the aggregate type also has a significant influence on the specific heat (thermal capacity) of concrete in which carbonate aggregate concrete has higher specific heat (heat capacity) in the 600–800 ^{o}C temperature range due to endothermic reaction which results from the decomposition of dolomite and absorbs a large amount of energy (Kodur and Harmathy 2008). The high heat capacity in carbonate aggregate concrete results in lower concrete spalling and better fire resistance of structural members. Nevertheless, Eurocode2 (2004) considers the specific heat of concrete as a linear function of temperature without taking into account the type of aggregates (see Table 2.1).

Density is the mass of a unit volume of the material, comprising the solid part and the air-filled pores. At elevated temperatures, concrete with high moisture content will experience a loss of mass resulting from evaporation of moisture due to heat. The mass loss of concrete at elevated temperatures is significantly influenced by the type of aggregates (Lie and Kodur 1996, Kodur and Sultan 1998). However, Eurocode2 (2004) has stated that the variation of density of concrete at elevated temperature is influenced mainly by water loss. Depending on the density, concrete are categorized

into two groups: (1) lightweight concrete with a density in the range of 1350 and 1850 kg/m^3; (2) normal-weight concrete with a density in the range of 2150 to 2450 kg/m^3.

Table 2.1 Variation of thermal properties of concrete with temperature (Eurocode2 2004)

Properties	Function of temperature
Thermal conductivity, $k_{c,T}$	Lower limit: $k_{c,T}^{L} = 1.36 - 0.136(T/100) + 0.0057(T/100)^2$ $\quad 20\,^{o}\mathrm{C} \le T \le 1200\,^{o}\mathrm{C}$ Upper limit: $k_{c,T}^{U} = 2 - 0.2451(T/100) + 0.0107(T/100)^2$ $\quad 20\,^{o}\mathrm{C} \le T \le 1200\,^{o}\mathrm{C}$
Specific heat, $c_{c,T}$	$c_{c,T} = \begin{cases} 900\ [\mathrm{J/kg\,K}] & 20 \le T < 100\,^{o}\mathrm{C} \\ 900 + (T-100)\ [\mathrm{J/kg\,K}] & 100\,^{o}\mathrm{C} \le T < 200\,^{o}\mathrm{C} \\ 1000 + (T-200)/2\ [\mathrm{J/kg\,K}] & 200\,^{o}\mathrm{C} \le T < 400\,^{o}\mathrm{C} \\ 1100\ [\mathrm{J/kg\,K}] & 400\,^{o}\mathrm{C} \le T < 1200\,^{o}\mathrm{C} \end{cases}$
Density, $\rho_{c,T}$	$\rho_{c,T} = \begin{cases} \rho_c(20^{o}\mathrm{C}) & T \le 115\,^{o}\mathrm{C} \\ \rho_c(20^{o}\mathrm{C})(1 - 0.02(T-115)/85) & 115\,^{o}\mathrm{C} < T \le 200\,^{o}\mathrm{C} \\ \rho_c(20^{o}\mathrm{C})(0.98 - 0.03(T-200)/200) & 200\,^{o}\mathrm{C} < T \le 400\,^{o}\mathrm{C} \\ \rho_c(20^{o}\mathrm{C})(0.95 - 0.07(T-400)/800) & 400\,^{o}\mathrm{C} < T \le 1200\,^{o}\mathrm{C} \end{cases}$ Where $\rho_c(20^{o}\mathrm{C}) = 2300\,\mathrm{kg/m^3}$

2.2.2 Mechanical Properties of Concrete

The mechanical properties of concrete required to be used as input data in the structural models in ANSYS are compressive strength, tensile strength, elastic modulus, thermal strain, Poisson's ratio and compressive stress-strain relationship. A wide range of data on the mechanical properties of concrete at elevated temperatures is available in the literature (Li, Qian et al. 2004, Noumowe 2005, Khoury 2008, Kodur and Harmathy 2008, Tang and Lo 2009). Due to a lack of standardized test specifications for undertaking high temperature mechanical property tests, these tests are usually carried out on a wide range of specimen sizes (Rilemtc129-Mht, De La Rilem et al. 1995). The mechanical properties of concrete at elevated temperatures used in the current study are obtained from Eurocode2 (2004).

The compressive strength of concrete is the key mechanical parameter. It is used to identify the strength grade and quality index of the concrete, and to determine the values of other mechanical properties such as tensile strength, elastic modulus, and peak strain. The factors affecting compressive strength at elevated temperatures are initial curing, moisture content at the time of testing, and the addition of admixtures and silica fume to the concrete mix (Dias, Khoury et al. 1990, Furumura, Abe et al. 1995, Felicetti and Gambarova 1998, Sideris 2007, Fares, Remond et al. 2010). According to Eurocode2 (2004), the compressive strength of concrete at elevated temperatures varies with aggregate types. The siliceous aggregate concrete provides higher relative compressive strength, $f_{c,T}/f_c(20^oC)$, than that of carbonate aggregate concrete as shown in Table 2.2. Note that only the carbonate aggregate concrete is considered herein.

As compared with the compressive strength, the tensile strength of concrete is much lower and is often neglected in strength calculations at room and elevated temperatures. However, the tensile strength of concrete is an important property in the fire resistance point of view. This is because cracking in concrete is generally due to tensile stresses and the structural damage of the member in tension is often generated by progression in microcracking (Mindess, Young et al. 2003). In the event of fire, the tensile strength of concrete plays an even more important role in cases where fire induced spalling occurs in concrete members (Khaliq and Kodur 2012). The tensile

strength of concrete at elevated temperatures proposed by Bazant and Chern (1987) is adopted for the current study.

The modulus of elasticity of concrete is required in the structural analysis to determine the strain distributions and displacements. At room temperature, the elastic modulus of concrete varies over a range from 5.0×103 to 35.0×103 MPa, and is dependent mainly on the water to cement ratio in the mixture, the age of concrete, the method of conditioning, and the amount and nature of the aggregates. Under fire condition, the modulus of elasticity of concrete influences the fire resistance of the concrete structures since it decreases at elevated temperature. The decrease in the elastic modulus of concrete is due to disintegration of hydrated cement products and breakage of bonds in the microstructure of cement paste which depends on moisture loss, high temperature creep, and type of aggregate (Cruz 1966). Eurocode2 (2004) has proposed a model to evaluate the modulus of elasticity of concrete at elevated temperature as a function of the compressive strength of concrete taking into account variation of the aggregate type.

Thermal strain is the expansion or shrinkage of a material caused by heating and is defined as the expansion or shrinkage of a unit length of a material when the temperature is raised by one degree. The thermal strain is considered to be positive (expansion) when the material elongates and negative (shrinkage) when the material shortens. Thermal strains are used to predict thermal stresses that generate in a structural member under fire condition and are evaluated through the dilatometric curve which is a record of the fractional change of a linear dimension of a solid at a steadily increasing or decreasing temperature (Harmathy 1970). The thermal strain of concrete is generally influenced by temperature, aggregate and cement type, water content, and age (Bazant and Chern 1987, Schaffer 1992). Other factors that influence the thermal expansion of concrete are additional volume changes caused by creep and microcracking resulting from nonuniform thermal stresses, by variation in moisture content, and by chemical reactions (dehydration, change of composition) (Bazant and Kaplan 1996). In some cases, the loss of water content due to heating results in a negative volume change, that is, shrinkage rather than expansion. Eurocode2 (2004) takes into account the effect of type of aggregates on the variation of thermal

expansion of concrete with temperature. The thermal expansion of siliceous aggregate concrete is higher than that of carbonate aggregate concrete.

The mechanical response of concrete at elevated temperatures is usually expressed in the form of stress-strain relations as a function of temperature. The stress-strain relation is used as input in the mathematical models for evaluating the fire resistance of concrete structural members. The compressive strength of concrete at elevated temperatures has a significant influence on the stress-strain response both at room and elevated temperatures. Eurocode2 (2004) has proposed a stress-strain relationship for concrete with parabolic ascending and linear descending branches. The model is defined by the ultimate compressive strength ($f_{c,T}$), the strain at peak stress ($\varepsilon_{cp,T}$) and ultimate strain ($\varepsilon_{cu,T}$) taken from Table 2.2 as a function of temperature as shown in Table 2.3.

Table 2.2 Variation of relative compressive strength, peak strain and ultimate strain of concrete with temperature

Temperature, T (^{o}C)	Siliceous aggregates			Calcareous aggregates		
	$f_{c,T}$ / f_c(20^{o}C)	$\varepsilon_{cp,T}$	$\varepsilon_{cu,T}$	$f_{c,T}$ / f_c(20^{o}C)	$\varepsilon_{cp,T}$	$\varepsilon_{cu,T}$
20	1.00	0.0025	0.0200	1.00	0.0025	0.0200
100	1.00	0.0040	0.0225	1.00	0.0040	0.0225
200	0.95	0.0055	0.0250	0.97	0.0055	0.0250
300	0.85	0.0070	0.0275	0.91	0.0070	0.0275
400	0.75	0.0100	0.0300	0.85	0.0100	0.0300
500	0.60	0.0150	0.0325	0.74	0.0150	0.0325
600	0.45	0.0250	0.0350	0.60	0.0250	0.0350
700	0.30	0.0250	0.0375	0.43	0.0250	0.0375
800	0.15	0.0250	0.0400	0.27	0.0250	0.0400
900	0.08	0.0250	0.0425	0.15	0.0250	0.0425
1000	0.04	0.0250	0.0450	0.06	0.0250	0.0450

Table 2.3 Variation of mechanical properties of concrete with temperature

Properties	Function of temperature	References
Tensile strength, $f_{ct,T}$	$f_{ct,T}=\begin{cases} f_{ct}(20^{o}\text{C})(1.01052-0.000526T) & 20\,^{o}\text{C}\le T\le 400\,^{o}\text{C} \\ f_{ct}(20^{o}\text{C})(1.8-0.0025T) & 400\,^{o}\text{C}< T\le 600\,^{o}\text{C} \end{cases}$ where $f_{ct}(20^{o}\text{C})=0.62\sqrt{f_{c}(20^{o}\text{C})}$	Bazant and Chern (1987)
Poisson's ratio, ν_c	$\nu_c=\begin{cases} 0 & \text{for cracked concrete} \\ 0.2 & \text{for uncraked concrete} \end{cases}$	Eurocode2 (2004)
Thermal strain, $\varepsilon_{c,T}^{th}$	Siliceous aggregates: $\varepsilon_{c,T}^{th}=\begin{cases} 2.3\times10^{-11}T^{3}+9\times10^{-6}T-1.8\times10^{-4} & 20\,^{o}\text{C}\le T\le 700\,^{o}\text{C} \\ 14\times10^{-3} & 700\,^{o}\text{C}< T\le 1200\,^{o}\text{C} \end{cases}$ Calcareous aggregates: $\varepsilon_{c,T}^{th}=\begin{cases} 1.4\times10^{-11}T^{3}+6\times10^{-6}T-1.2\times10^{-4} & 20\,^{o}\text{C}\le T\le 805\,^{o}\text{C} \\ 12\times10^{-3} & 805\,^{o}\text{C}< T\le 1200\,^{o}\text{C} \end{cases}$	Eurocode2 (2004)
Compressive stress-strain relationship, $\sigma_{c,T}-\varepsilon_{c,T}$	$\sigma_{c,T}=\begin{cases} \dfrac{3.\varepsilon_{c,T}\cdot f_{c,T}}{\varepsilon_{cp,T}\cdot\left[2+\left(\dfrac{\varepsilon_{c,T}}{\varepsilon_{cp,T}}\right)^{3}\right]} & \text{for } \varepsilon_{c,T}\le\varepsilon_{cp,T} \\ f_{c,T}\cdot\left(1-\dfrac{\varepsilon_{c,T}-\varepsilon_{cp,T}}{\varepsilon_{cu,T}-\varepsilon_{cp,T}}\right) & \text{for } \varepsilon_{cp,T}<\varepsilon_{c,T}\le\varepsilon_{cu,T} \end{cases}$	Eurocode2 (2004)

2.3 Reinforcing Steel at Elevated Temperatures

2.3.1 Thermal Properties of Reinforcing Steel

The thermal properties of reinforcing steel (i.e., thermal conductivity, specific heat and density) are required in the heat transfer model to obtain the temperature distribution in the fire-exposed RC members. According to Eurocode3 (2005), the thermal conductivity of reinforcing steel varies linearly with temperature as shown in Table 2.4 while the density of reinforcing steel remains constant with the value of 7850 kg/m^3.

2.3.2 Mechanical Properties of Reinforcing Steel

In order to evaluate the behavior of RC structures exposed to fire, certain mechanical properties of reinforcing steel–i.e., yield and proportional limit strength, thermal strain, Poisson's ratio, modulus of elasticity and stress-related strain–are required as input in the structural model. These properties are taken from Eurocode3 (2005) as shown in Table 2.5-2.6. The drop of the strength and stiffness and the increase in thermal expansion of reinforcing steel at elevated temperature can lead to excessive displacements which may in turn contribute to the failure of RC structures.

Table 2.4 Variation of thermal properties of reinforcing steel with temperature (Eurocode3 2005)

Properties	Function of temperature
Thermal conductivity, $k_{s,T}$	$k_{s,T} = \begin{cases} 54 - 3.33\times10^{-2}T \ \text{[W/m.K]} & 20^{o}\text{C} \le T < 800^{o}\text{C} \\ 27.3 \ \text{[W/m.K]} & 800^{o}\text{C} \le T \le 1200^{o}\text{C} \end{cases}$
Specific heat, $c_{s,T}$	$c_{s,T} = \begin{cases} 425 + 7.73\times10^{-1}T - 1.69\times10^{-3}T^{2} + 2.22\times10^{-6}T^{3} \ \text{[J/kg K]} & \\ \quad (20\,^{o}\text{C} \le T < 600\,^{o}\text{C}) & \\ 900 + (T - 100) \ \text{[J/kg K]} & (600\,^{o}\text{C} \le T < 735\,^{o}\text{C}) \\ 1000 + (T - 200)/2 \ \text{[J/kg K]} & (735^{o}\text{C} \le T < 900\,^{o}\text{C}) \\ 1100 \ \text{[J/kg K]} & (900\,^{o}\text{C} \le T < 1200\,^{o}\text{C}) \end{cases}$

Table 2.5 Variation of relative factors for effective yield strength, proportional limit, and the slope of the linear elastic range with temperature (Eurocode3 2005)

Temperature $T(^{o}\text{C})$	Relative factor for effective yield strength $\frac{f_{y,T}}{f_{y}(20^{o}\text{C})}$	Relative factor for proportional limit $\frac{f_{p,T}}{f_{y}(20^{o}\text{C})}$	Relative factor for the slope of the linear elastic $\frac{E_{s,T}}{E_{s}(20^{o}\text{C})}$
20	1.000	1.000	1.000
100	1.000	1.000	1.000
200	1.000	0.807	0.900
300	1.000	0.613	0.800
400	1.000	0.420	0.700
500	0.780	0.360	0.600
600	0.470	0.180	0.310
700	0.230	0.075	0.130
800	0.110	0.050	0.090
900	0.060	0.0375	0.0675
1000	0.040	0.0250	0.0450

Table 2.6 Variation of mechanical properties of reinforcing steel with temperature (Eurocode3 2005)

Properties	Function of temperature
Poisson's ratio, ν_s	$\nu_s = 0.3$
Thermal strain, $\varepsilon_{s,T}^{th}$	$\varepsilon_{s,T}^{th} = \begin{cases} 0.4\times10^{-8}T^2 + 1.2\times10^{-5}T - 2.416\times10^{-4} & 20\,^{o}\text{C} \le T < 750\,^{o}\text{C} \\ 1.1\times10^{-2} & 750\,^{o}\text{C} \le T \le 860\,^{o}\text{C} \\ 2\times10^{-5}T - 6.2\times10^{-3} & 860\,^{o}\text{C} < T \le 1200\,^{o}\text{C} \end{cases}$
Stress-strain, $\sigma_{s,T} - \varepsilon_{s,T}$	$\sigma_{s,T} = \begin{cases} \varepsilon E_{s,T} & \text{for } \varepsilon \le \varepsilon_{p,T} \\ f_{p,T} - Z + \dfrac{Y\left[X^2 - \left(\varepsilon_{sy} - \varepsilon\right)^2\right]^{0.5}}{X} & \text{for } \varepsilon_{p,T} < \varepsilon < \varepsilon_{sy} \\ f_{y,T} & \text{for } \varepsilon_{sy} \le \varepsilon \le \varepsilon_{st} \\ f_{y,T}\left[1 - \dfrac{\left(\varepsilon - \varepsilon_{st}\right)}{\left(\varepsilon_{su} - \varepsilon_{st}\right)}\right] & \text{for } \varepsilon_{st} < \varepsilon < \varepsilon_{su} \\ 0.00 & \text{for } \varepsilon = \varepsilon_{su} \end{cases}$ where $\varepsilon_{p,T} = \dfrac{f_{p,T}}{E_{s,T}}$; $\varepsilon_{sy} = 0.02$; $\varepsilon_{st} = 0.15$; $\varepsilon_{su} = 0.20$ $X^2 = \left(\varepsilon_{sy} - \varepsilon_{p,T}\right)\left(\varepsilon_{sy} - \varepsilon_{p,T} + \dfrac{Z}{E_{s,T}}\right)$ $Y^2 = Z\left(\varepsilon_{sy} - \varepsilon_{p,T}\right)E_{s,T} + Z^2$ $Z = \dfrac{\left(f_{y,T} - f_{p,T}\right)^2}{\left(\varepsilon_{sy} - \varepsilon_{p,T}\right)E_{s,T} - 2\left(f_{y,T} - f_{p,T}\right)}$

CHAPTER 3
MODELING OF PRECAST CONCRETE LOAD-BEARING WALLS AT ELEVATED TEMPERATURES

3.1 Introduction

Most reinforced concrete structures used in engineering construction are designed following simplified rules and empirical assumptions. Computer programs based on the finite element method have provided means for analysis of much more complex systems in a more realistic way. The main obstacle to the finite element analysis of reinforced concrete structures is the difficulty in characterizing the material properties. Much effort has been spent in search of a realistic model to predict the behavior of reinforced concrete structures. Due mainly to the complexity of the composite nature of concrete, proper modeling of such structures is a challenging task.

Combined bending and axial loads in reinforced concrete members can cause complicated geometrical non-linearities (i.e., the so-called P-delta effect). In this case, no closed-form analytical solution is possible even under normal-temperature conditions; therefore, in a fire study a numerical model is needed. In the event of fire, the geometry and material properties are altered due to thermal exposure at each time step and, hence, a complete structural solution must be found at each time step.

The focus of this thesis is to examine the behavior of precast concrete walls under eccentric load which are exposed to fire on one side. The thermal gradient between the exposed and the unexposed side of the walls would result in non-uniform thermal expansion, causing the walls to bend toward their exposed side. This phenomenon, known as thermal bowing, coupled with the effect of eccentric loading, may cause the walls to have geometrical nonlinearities. The eccentric load can be converted to combined bending and axial loads to be applied on the top surface of the walls. According to Eurocode2 (2004), the mechanical properties of concrete and steel rebar at elevated temperatures are also non-linear. Therefore, a numerical model

is needed in order to investigate the behavior of precast concrete load-bearing walls at elevated temperatures.

As mentioned in Chapter 1, the commercial finite element program ANSYS is used in this thesis to examine the behavior of precast concrete load-bearing walls exposed to fire. Three-dimensional models are selected in order to better simulate the actual behavior of the walls and to establish a model for walls with varying configurations.

In this thesis two cases are examined. The first case deals with the precast concrete wall under thermal load only. The second case involves precast concrete walls under both thermal and axial loads with a specified eccentricity.

3.2 Finite Element Model

ANSYS is one of the most widely used commercial finite element programs which can be applied to a vast array of problems in engineering field. In this study, ANSYS 14.5 has been adopted for the investigation of thermo-mechanical behavior of precast concrete load-bearing walls exposed to fire. The analyses are carried out in two stages: transient thermal analysis and structural stress analysis. In the first stage, a thermal analysis in which the standard ISO 834 fire curve was applied as nodal temperatures on one side of the wall specimen in terms of load steps is performed. Each load step consists of several substeps that are solved using Newton-Raphson technique (ANSYS 2012a). The standard ISO834-1 (1999) fire curve can be illustrated in Figure 3.1. For the second stage a structural stress analysis is conducted in order to predict the performance of the wall specimens under axial load as well as the temperature distribution obtained from the thermal model in the first stage. The framework of the analytical procedure is shown in Figure 3.2.

The element types used in the transient thermal analysis are SOLID70 (3D 8-node thermal solid element) for concrete and LINK33 (3D uniaxial 2-node conduction bar element) for steel rebar. These thermal elements are replaced by structural elements for the structural stress analysis as follows:

- For concrete, the thermal SOLID70 element is replaced by the structural SOLID65 element (3D 8-node reinforced concrete solid element).
- For steel rebar, the thermal LINK33 element is replaced by the structural LINK8 element (3D 2-node structural bar element).

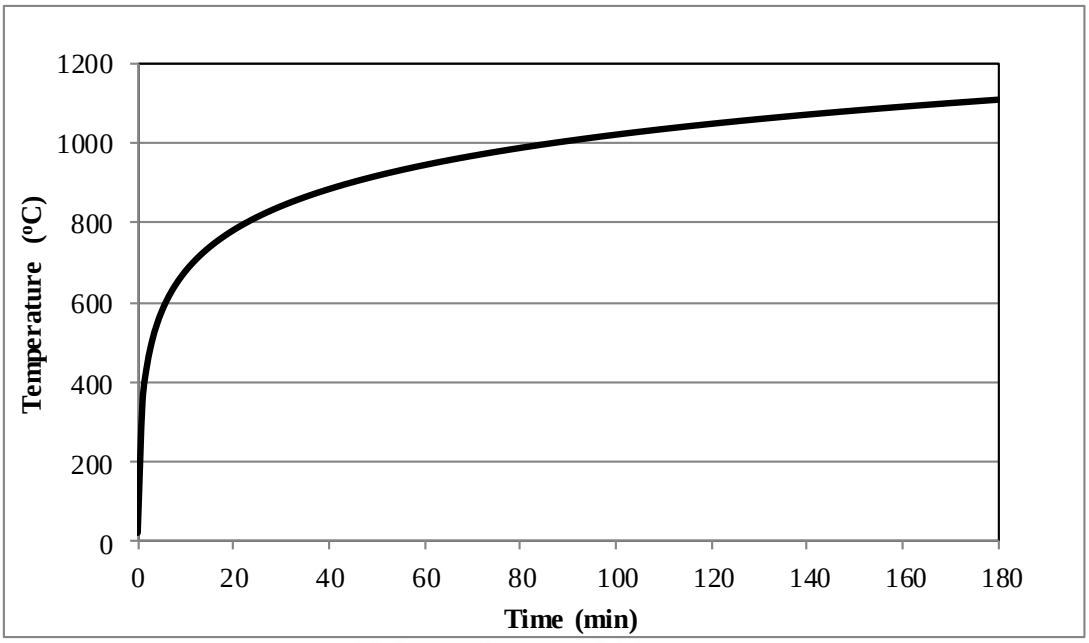

Figure 3.1: ISO 834 standard fire (ISO 834-1 1999).

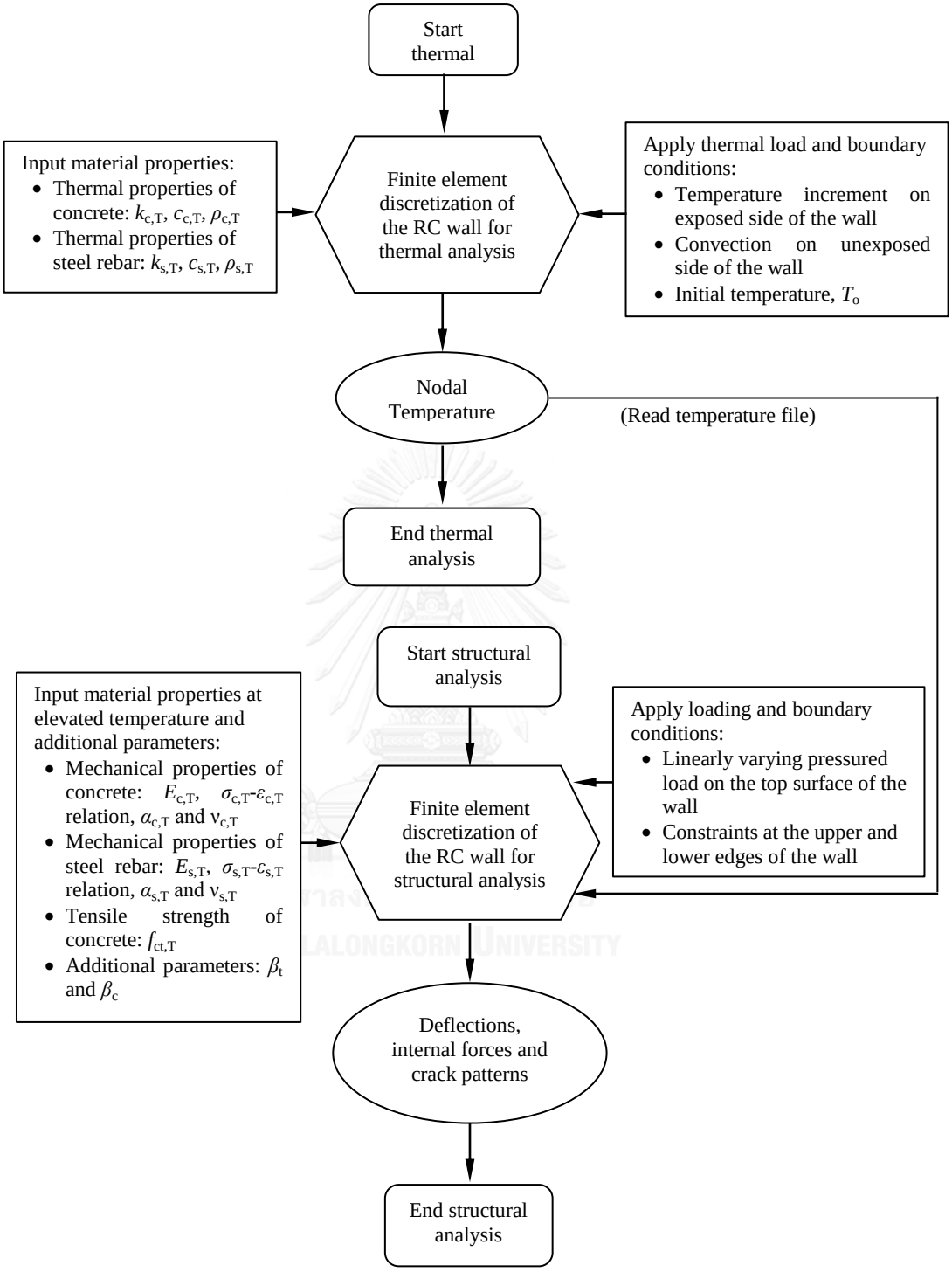

Figure 3.2: Overall framework of finite element analysis.

3.2.1 Thermal Model

The thermal model requires calculations of transient heat transfer to evaluate the temperature distribution within the wall. The load steps are specified in time increment of 60 s. The thermal model of the reinforced concrete wall investigated in the current study comprises three dimensional solid elements for concrete and link elements for steel rebar. The standard time-temperature curve according to ISO 834 (1999) is applied on one side of the wall. Convection and radiation are also taken into account on the unexposed side of the wall while the four edges of the wall are insulated by ceramic fiber. Note that insulation is imposed automatically in ANSYS when no thermal condition is specified along a boundary (Madenci and Guven 2007). Therefore, no boundary conditions have been imposed at the four edges of the wall in the thermal model. The thermal loads and boundary conditions of the walls are shown in Figure 3.3.

According to Buchanan (2001) and Franssen, Kodur et al. (2009), the dominant heat transfer within the test furnace from the fire nozzles to the structures inside the fire chamber is radiation. However, in the actual fire test, the fire nozzles in the furnace are in close proximity to the tested walls and the exposed surface temperatures, which are measured by using thermocouples, are used as input temperatures in the thermal model. The results obtained by using this technique are in good agreement with the experimental results reported in the current and previous studies (Lie and Williams-Leir 1979, Lim, Buchanan et al. 2004) as discussed in Chapter 4.

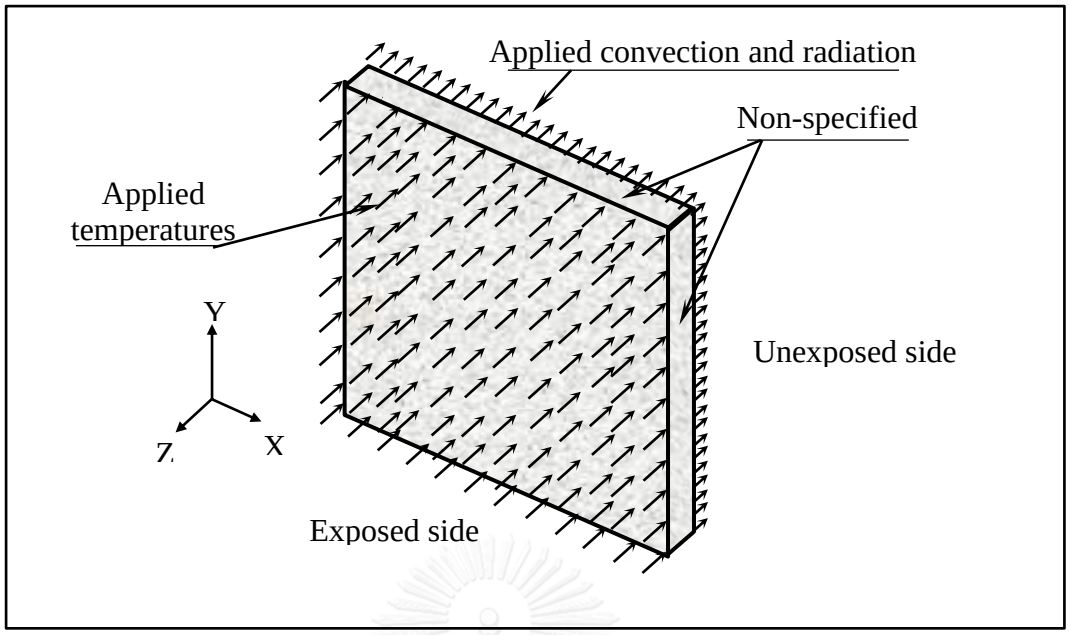

Figure 3.3: Applied thermal loads and boundary conditions on the wall.

3.2.1.1 Concrete

In the thermal analysis, concrete is modeled using 3-D thermal conduction elements comprising eight nodes with a single degree of freedom (i.e., temperature) at each node. This element is applicable to a 3-D, steady-state or transient thermal analysis. The geometry and node locations of this element type are shown in Figure 3.4.

Concrete is a non-homogeneous, anisotropic medium composed of particles of aggregates mixed with hydrated cement paste. It can be considered as a homogeneous isotropic material in heat transfer analysis for simplicity. However, the temperature dependence of the thermal properties of concrete has a significant effect on thermal analysis.

The temperature-dependent thermal properties of concrete i.e., conductivity $k_{c,T}$, specific heat $c_{c,T}$ and density $\rho_{c,T}$ make the heat transfer analysis nonlinear. Since the thermal properties of concrete at high temperature are quite difficult to obtain with only scarce data available in the literature (e.g. Zhu and Chao (2002)), their variation with temperature employed in the proposed implementation scheme is based on Eurocode2 (2004).

Thermal conductivity represents the rate of heat transferred through a unit thickness of the material per unit temperature difference, with units of W/m-K. The thermal conductivity of concrete, $k_{c,T}$, are given by the upper and lower bounds according to the Eurocode2 (2004) as shown in Figure 3.5.

Specific heat is the amount of heat required to heat up a unit mass of the material by one degree, with units of J/kg-K. The specific heat depends upon the moisture content of the materials. The specific heat of concrete $c_{c,T}$ with calcareous aggregates may be modeled taking into account the moisture content in the calculation method as can be seen in Figure 3.6. In the current study, the moisture content of 3% of concrete weight is assumed in the model.

Density of concrete is the concrete mass per volume with units of kg/m^3. This property varies with temperature as influenced by water loss. The concrete density temperature curve is shown in Figure 3.7.

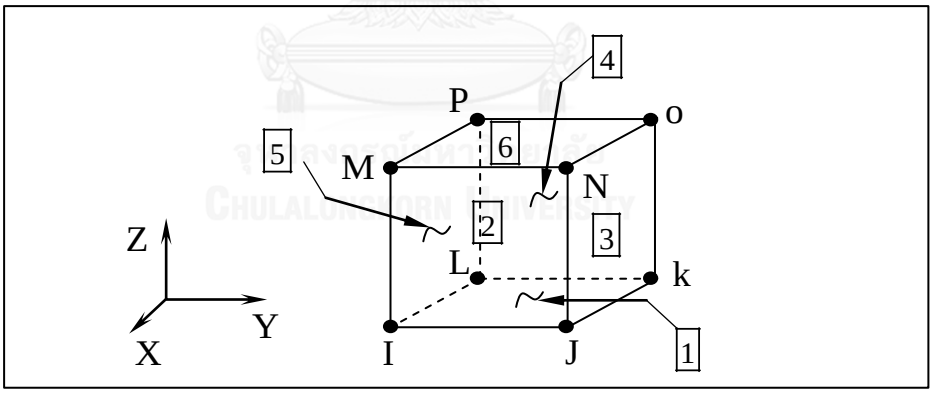

Figure 3.4: SOLID70 element (ANSYS 2012b).

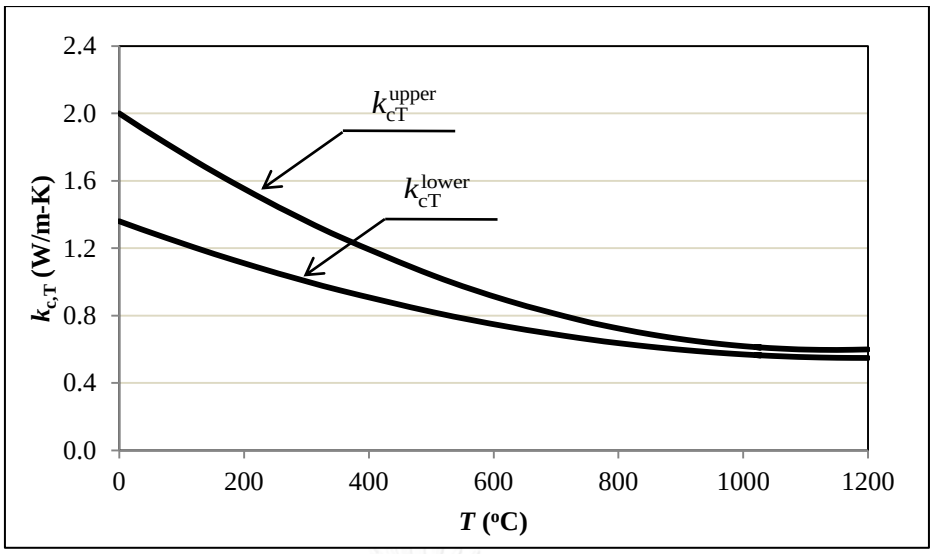

Figure 3.5: Thermal conductivity of concrete at elevated temperature (Eurocode2 2004)

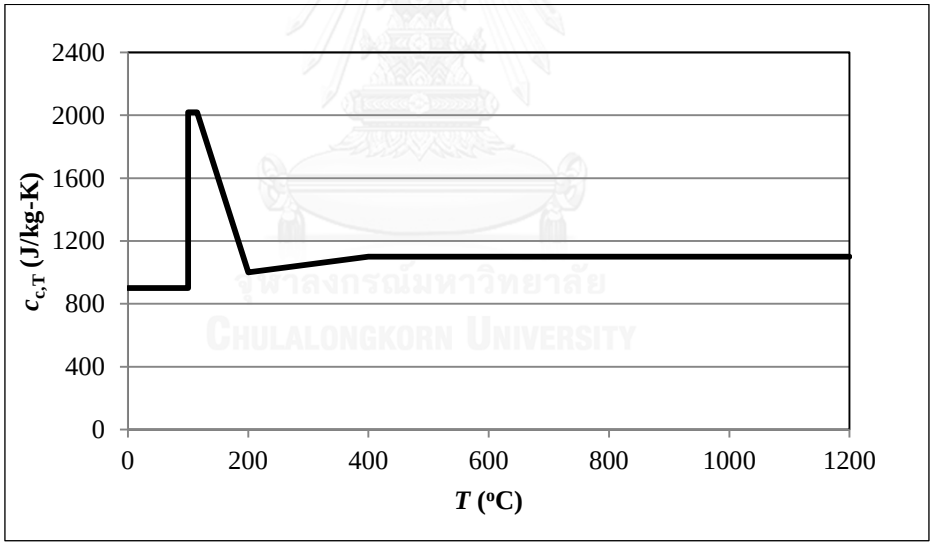

Figure 3.6: Specific heat as a function of temperature for calcareous concrete (3% moisture content by weight) (Eurocode2 2004).

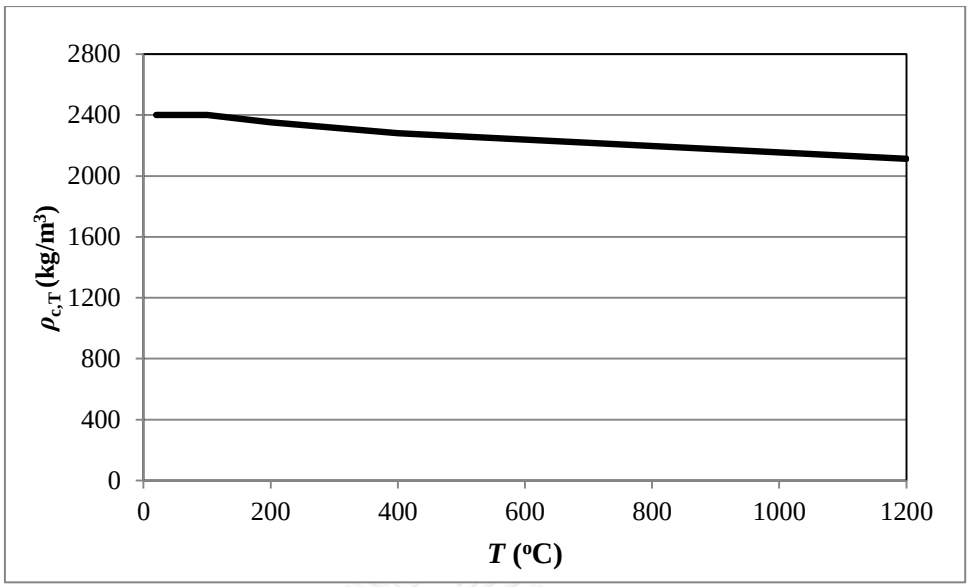

Figure 3.7: Density of concrete at elevated temperature (Eurocode2 2004).

3.2.1.2 Steel Rebar

Steel rebar is modeled using a 3-D link uniaxial element with the ability to conduct heat between its nodes. The element has a single degree of freedom, temperature, at each node. The conducting bar is applicable to a steady-state or transient thermal analysis. The geometry, node locations, and the coordinate system for the 3-D link uniaxial element are shown in Figure 3.8. The element is characterized by two nodes, a cross-sectional area and the material properties. The thermal conductivity is in the element longitudinal direction (ANSYS 2012b).

The thermal conductivity of steel rebar, $k_{s,T}$, depends mainly on the amount of alloying elements and on the heat treatment. Figure 3.9 shows the thermal conductivity of steel rebar at elevated temperature in accordance with Eurocode3 (2005).

The specific heat of steel rebar at elevated temperature is based on Eurocode3 (2005) as shown in Figure 3.10.

As opposed to concrete, the density of steel rebar can be taken as constant regardless of the variation of temperature. The constant value is $\rho_s = 7850$ kg/m^3 according to Eurocode2 (2004).

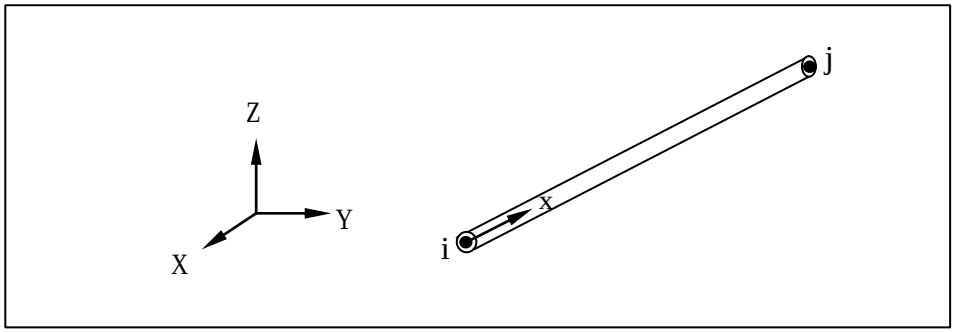

Figure 3.8: LINK33 element (ANSYS 2012b).

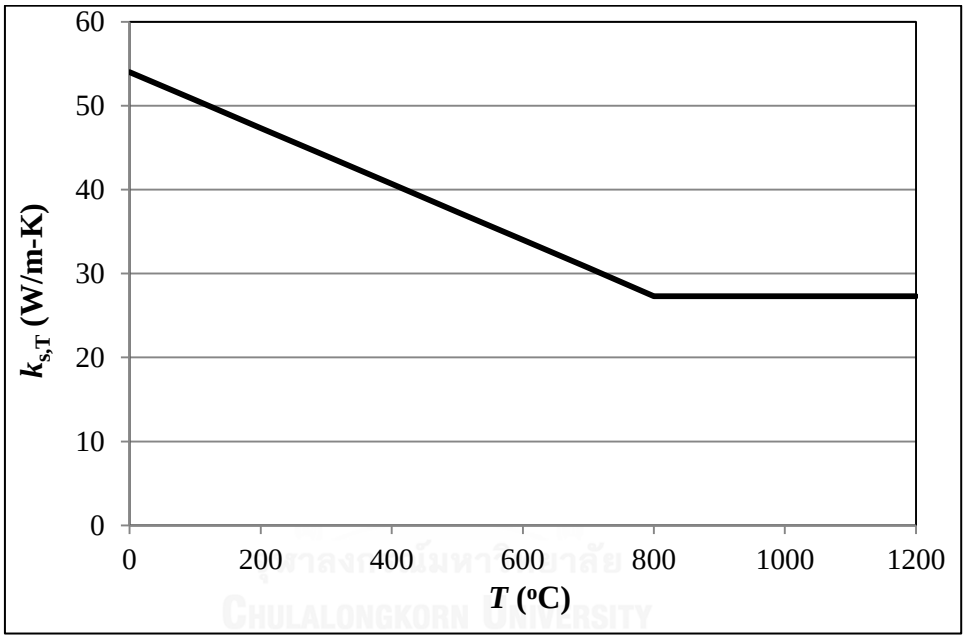

Figure 3.9: Thermal conductivity of steel rebar at elevated temperature (Eurocode3 2005).

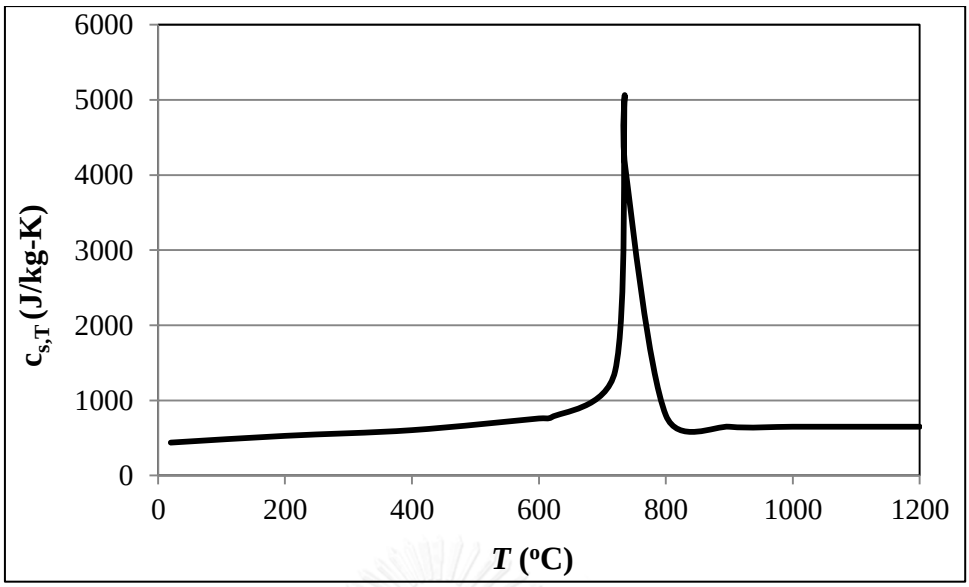

Figure 3.10: Specific heat temperature curve of steel rebar (Eurocode3 2005).

3.2.2 Structural Model

The structural model is used to compute deflections, internal forces and cracking patterns of the walls due to the applied load and temperatures from the thermal analysis. The temperatures are input as thermal-body load while the axial loads used in the experimental program (10% of the buckling load capacity of the wall at normal temperature) are applied as linearly varying pressure on the top surface of the wall.

In this thesis the boundary conditions of the walls are also varied to investigate the effects of end restraints on the behavior of the walls exposed to fire. Note that the structural model does not take into account any geometric imperfection due to fabrication or test setup of the wall specimens.

Because the properties of constituent materials play an important role in determining the response of the precast concrete load-bearing wall exposed to fire, these properties are considered temperature dependent as discussed in the following sections.

3.2.2.1 Concrete

Concrete is modeled using 3-D structural elements. The element has eight nodes in which each node has of three degrees of freedom: translations in X, Y and Z directions. The element can be used for three dimensional modeling of concrete with or without reinforcement and can account for cracking of concrete in tension, crushing of concrete in compression, creep and large strains (ANSYS 2012b). The geometry and node locations of this element type are shown in Figure 3.11.

The material model for concrete in ANSYS adopts the nonlinear constitutive model of Willam and Warnke (1975). This model takes into account the material nonlinearity of concrete in tension and in compression by considering concrete elements to be cracking upon reaching the ultimate tensile strength, and to be crushing once the maximum compressive strength is reached. Furthermore, concrete is treated as an isotropic material up to the first crack then it becomes an anisotropic material after the initiation of cracks. Once a concrete element cracks, the modulus of elasticity is set to be zero in the direction parallel to the principle tensile stress direction.

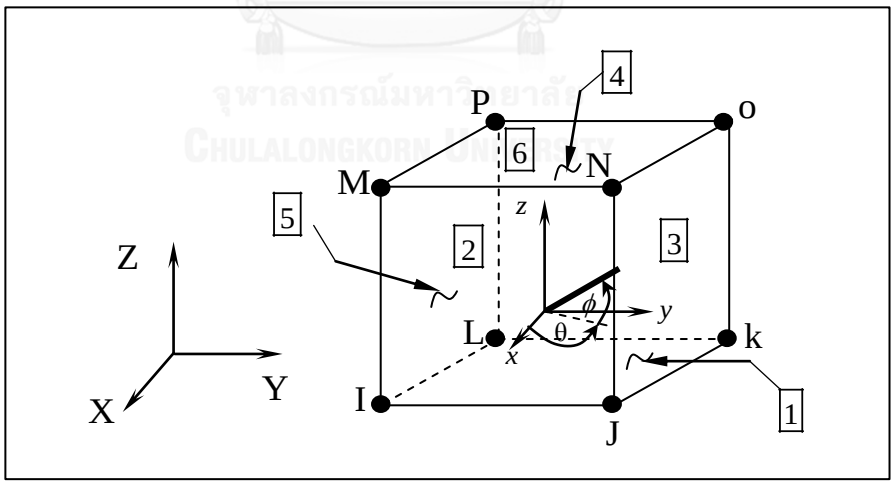

Figure 3.11: SOLID65 element (ANSYS 2012b).

Willam and Warnke (1975) have adopted a typical three-dimensional failure surface for concrete where the state of stress is biaxial or nearly biaxial in *x* and *y* directions as shown in Figure 3.12 in which the compressive and tensile strengths of concrete are represented by $f_{c,T}$ and f_{ct} , respectively. Based on this criterion, when the principal stresses in the *x* and *y* directions (σ_{xp} and σ_{yp}) are negative (compressive), the failure surface is based upon the sign of the principal stress in *z* direction (σ_{zp}) and three failure modes are possible. A cracking surface of concrete occurs when the principal stress in *z* direction is slightly greater than zero and a crushing surface of concrete occurs when the principal stress in *z* direction is equal to or slightly less than zero. In case the principal stresses in the *x* and *y* directions are positive (tensile) the failure surface of concrete represents cracking. In the finite element analysis, cracking of a concrete element occurs when the tensile stress in any direction lies outside the failure surface. Crushing of a concrete element occurs when the principal stresses in all directions are compressive and lie outside the failure surface. After crushing, the elastic modulus of concrete is set to zero in all directions and the element local stiffness becomes zero. This results in large displacements and therefore divergence of the finite element solution. Concrete crushing is ignored in this proposed model by turning off the crushing capacity of the SOLID65 concrete element (ANSYS 2012b).

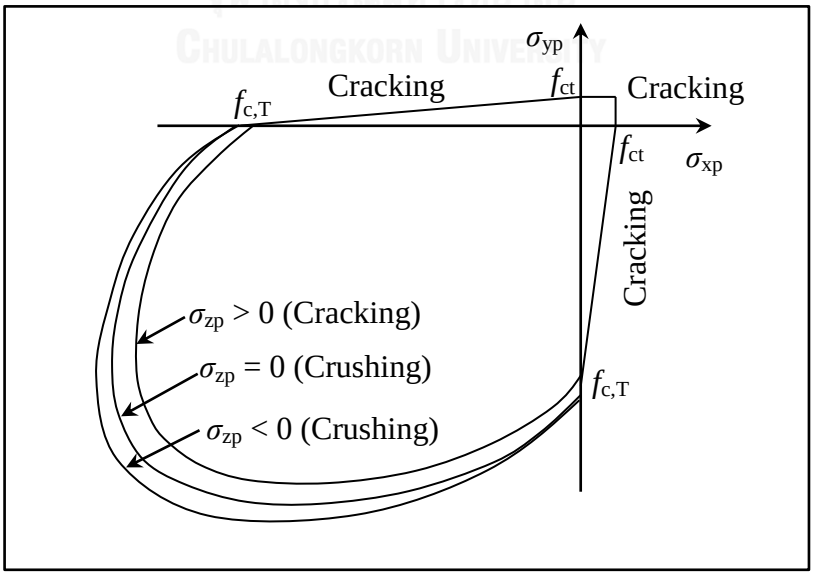

Figure 3.12: 3-D failure surface of concrete (Willam and Warnke 1975).

Additional parameters required for the constitutive model of Willam and Warnke (1975) are open and close crack shear transfer coefficients, β_t and β_c. The shear transfer coefficient is zero when there is a total loss of shear transfer representing a smooth crack and 1.0 when there is no loss of shear transfer representing a rough crack. The values of β_t and β_c in the proposed model are selected as 0.2 and 0.7, respectively (Kodur, Naser et al. 2013).

It has been shown in the literature (Hawileh, Naser et al. 2009, Hawileh and Naser 2012, Aziz and Kodur 2013, Kodur, Naser et al. 2013) that the mechanical properties of concrete and steel rebar based on the Eurocode2 and Eurocode3 can be successfully used to model the behavior of RC structures at elevated temperatures. As such, the temperature-dependent mechanical properties of the materials of the Eurocode2 and Eurocode3 are also adopted for the current study as input in the structural model.

In general, three major factors–i.e., cracking of concrete, nonlinearity of concrete in compression and plasticity of steel rebar–must be included to account for the nonlinear response of reinforced concrete structures. A multi-linear kinematic hardening model (KINH) is implemented in ANSYS 14.5 to accommodate the plastic behavior of concrete at each temperature level as illustrated in Figure 3.13. The curves shown in the Figure 3.13 are generated based on the strength reduction factors given by Eurocode2 (2004) for calcareous aggregates with a specified compressive strength at normal temperature of 43 MPa (specimen 1). It can be seen from Figure 3.13 that the uniaxial compressive stress-strain curve of concrete at elevated temperature is linear up to the proportional limit, about 35% of the ultimate compressive stress (Hawileh, Naser et al. 2009).

The tensile strength of concrete at normal temperature is taken as $0.62\sqrt{f_{c,T}}$ where $f_{c,T}$ is the compressive strength of concrete (Hawileh, Naser et al. 2009, Hawileh and Naser 2012, Aziz and Kodur 2013, Kodur, Naser et al. 2013). Once the concrete material reaches its tensile strength, a tensile stiffness multiplier of 0.6 is used to simulate a sudden drop of the tensile stress to 60% of the initial tensile rupture

stress, followed by a linearly descending curve to zero stress at a strain value of six times the strain corresponding to the concrete rupture stress (ANSYS 2012a).

For the current study, the tensile strength of concrete at elevated temperature is referred to Bazant and Chern (1987). The tensile stress-strain relationship of concrete is based on Pantazopoulou and Papoulia (2001) for the pre-peak stage and ANSYS (2012a) for the post-peak stage as illustrated in Figure 3.14.

Thermal strain is the free thermal expansion due to the elevated temperature. The lack of compatibility between the aggregates and the matrix, and the chemical and physical changes of the aggregates at elevated temperatures result in nonlinearity of the thermal strain of concrete. The value of the thermal strain of concrete with calcareous aggregates as a function of temperature is provided by Eurocode2 (2004) as illustrated in Figure 3.15.

Poisson's ratio is a negative ratio of transverse to axial strains. When concrete is compressed in one direction, it tends to expand in the other two directions perpendicular to the direction of flow. The Poisson's ratio of concrete used in this study is taken from Eurocode2 (2004), which is independent of temperature with a constant value of 0.2.

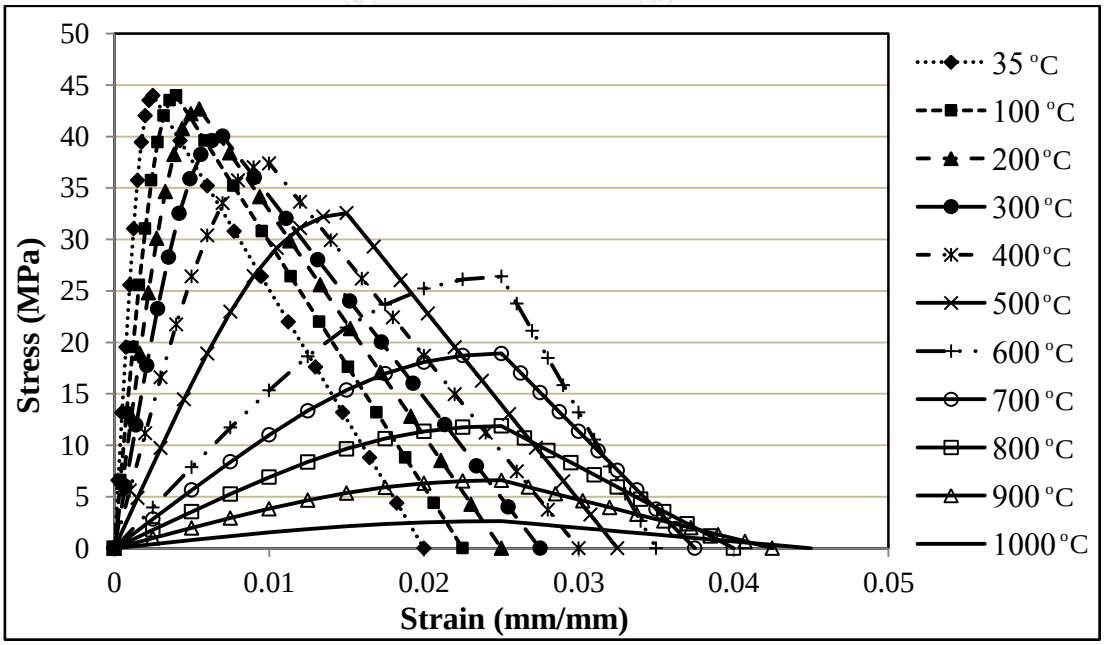

Figure 3.13: Compressive stress-strain curves for concrete at elevated temperatures (Eurocode2 2004).

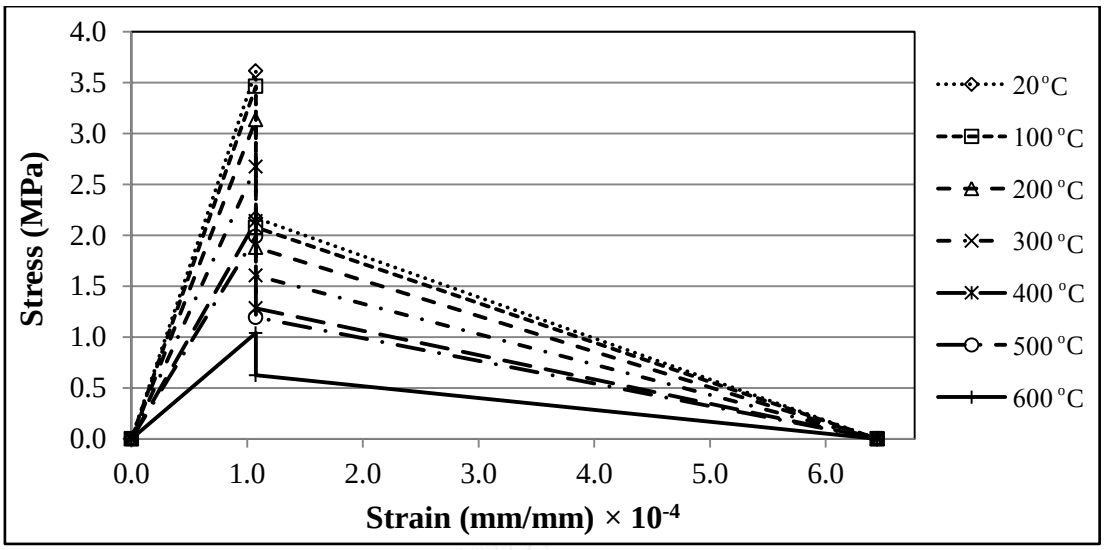

Figure 3.14: Tensile stress-strain curves of concrete at elevated temperatures (Eurocode2 2004).

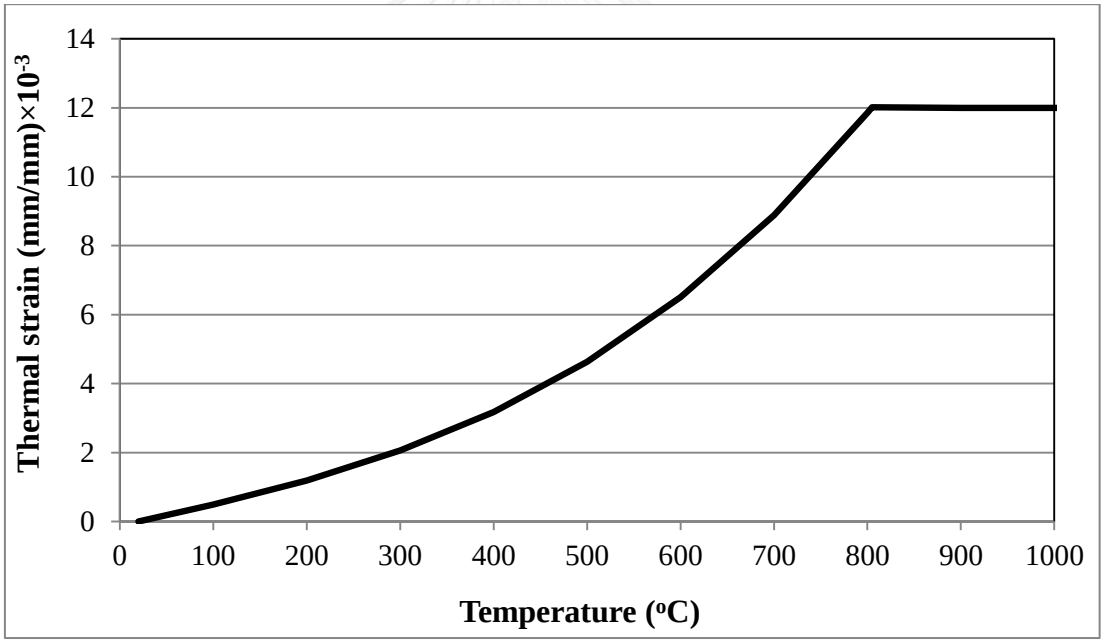

Figure 3.15: Thermal strain of concrete at elevated temperature (Eurocode2 2004).

3.2.2.2 Steel Rebar

Three techniques can be used to incorporate steel rebar in the finite element models for reinforced concrete structures (Tavárez 2001). These techniques are discrete, embedded and smeared models as illustrated in Figure 3.16.

The steel rebar in the discrete model (Figure 3.16a) is represented by bar or beam elements connected to concrete mesh nodes. Therefore, the concrete and the steel rebar elements share the same nodes and the steel rebar occupies the same regions occupied by the concrete. A drawback to this model is that the concrete mesh is restricted by the location of the steel rebar and the volume of the steel rebar is not deducted from the volume of the surrounding concrete.

In the embedded model (Figure 3.16b), the stiffness of the steel rebar is evaluated separately from that of concrete elements. The model is built in a way that keeps steel rebar displacements compatible with the surrounding concrete elements. The embedded model is advantageous for structures with complicated steel rebar. However, this model increases the number of nodes and degrees of freedom in the model, therefore, increasing the running time and computational cost.

In the smeared model (Figure 3.16c), the steel rebar elements are assumed to uniformly spread throughout the concrete elements in a defined region of the finite element mesh. For a large-scale model where reinforcement does not significantly contribute to overall response of the structure, the smeared model is recommended to use.

Fanning (2001) modeled the response of the reinforcement of reinforced concrete beam using the discrete and the smeared model. It was found that the best way for modeling reinforcement was to use the discrete model.

Following the recommendation by Fanning (2001), the current study adopts the discrete model for steel rebar. The steel rebar is modeled using link uniaxial tension-compression elements with three degrees of freedom at each node: translations in the x, y, and z directions. The element is capable of modeling plasticity, creep, swelling, stress stiffening, and large deflection (ANSYS 2012b).The geometry and node locations of this element type are shown in Figure 3.17.

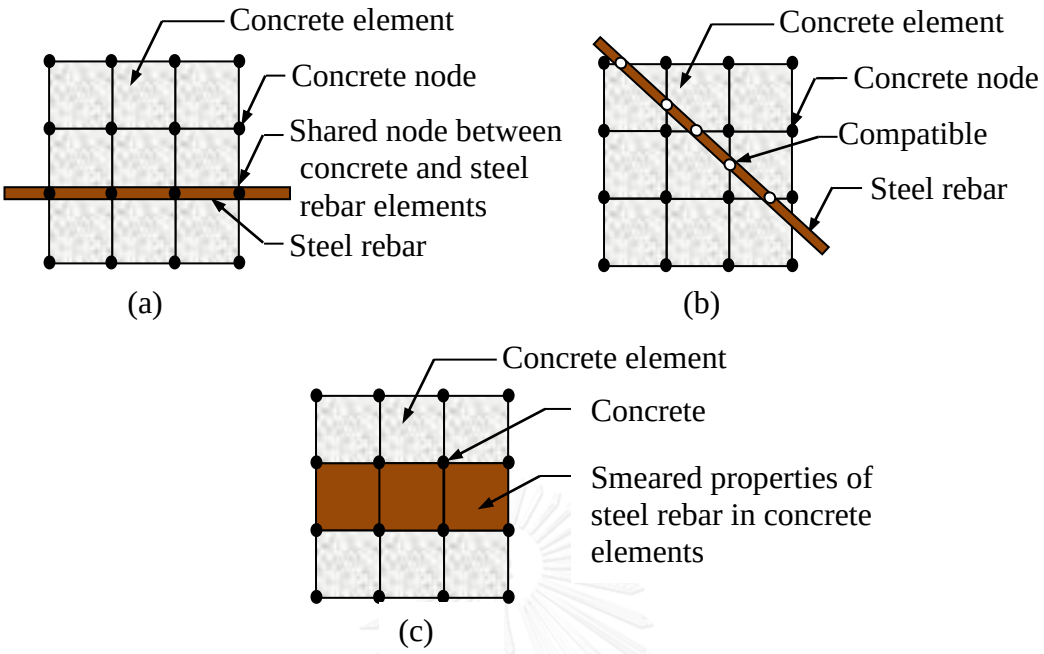

Figure 3.16: Models for steel rebar in reinforced concrete (Tavárez 2001): (a) discrete model; (b) embedded model; (c) smeared model.

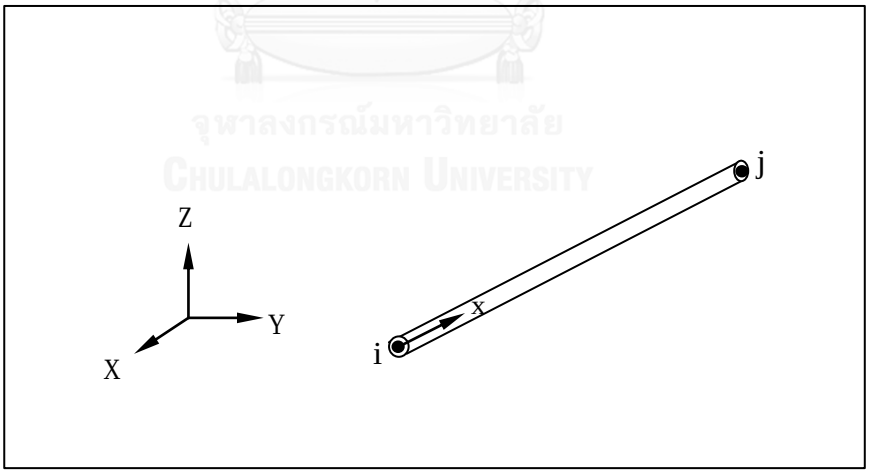

Figure 3.17: LINK8 element (ANSYS 2012b).

The steel rebar is assumed to behave as an elasto-plastic material both in tension and compression. The multi-linear isotropic hardening model (MISO) is implemented in ANSYS 14.5 by considering the modulus of elasticity of steel rebar as the initial tangent modulus of the stress-strain curve (ANSYS 2012a). Figure 3.18 shows the multi-linear stress–strain curves for steel rebar at elevated temperatures based on the reduction factors of yield strength and the corresponding strains taken from Eurocode2 (2004).

Other temperature-dependent mechanical properties of steel rebar required to be specified as input in the structural model are modulus of elasticity, thermal expansion coefficient or thermal strain and Poisson's ratio. The modulus of elasticity and thermal strain of steel rebar are based on Eurocode2 (2004) as illustrated in Figure 3.19 and Figure 3.20, respectively. The Poisson's ratio of steel rebar is taken as 0.3 regardless of the temperature level according to Eurocode3 (2005).

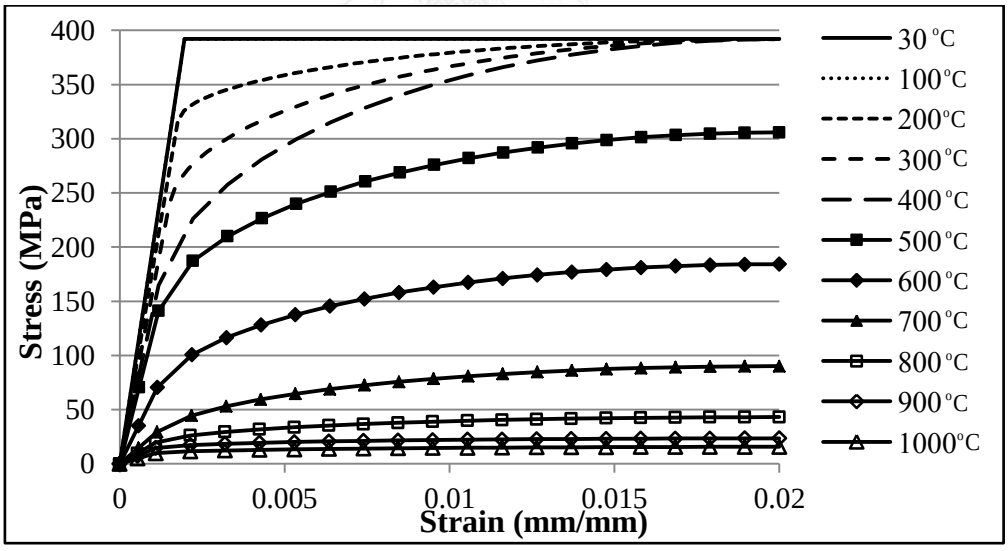

Figure 3.18: Stress-strain curves for steel rebar at elevated temperature (Eurocode2 2004).

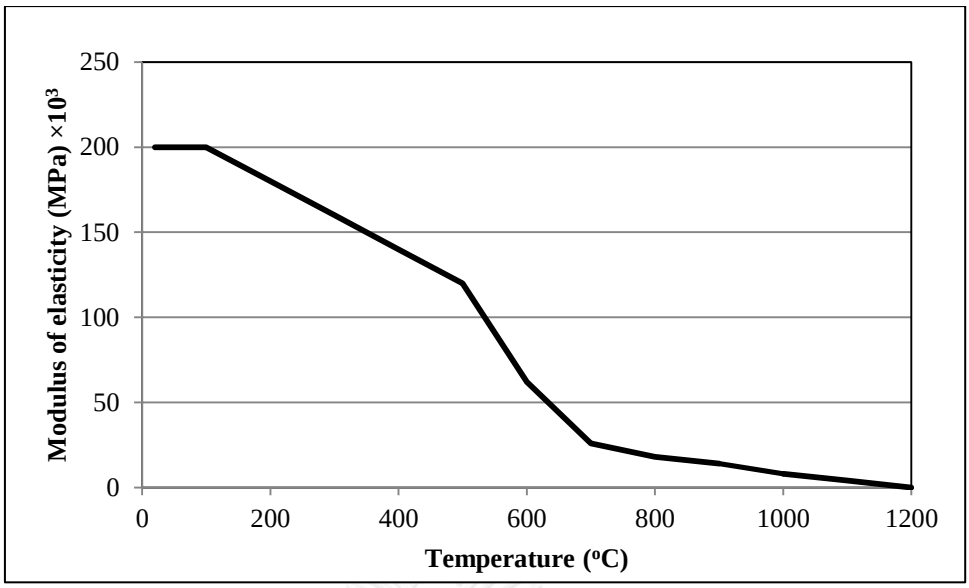

Figure 3.19: Modulus of elasticity of steel rebar at elevated temperature (Eurocode3 2005).

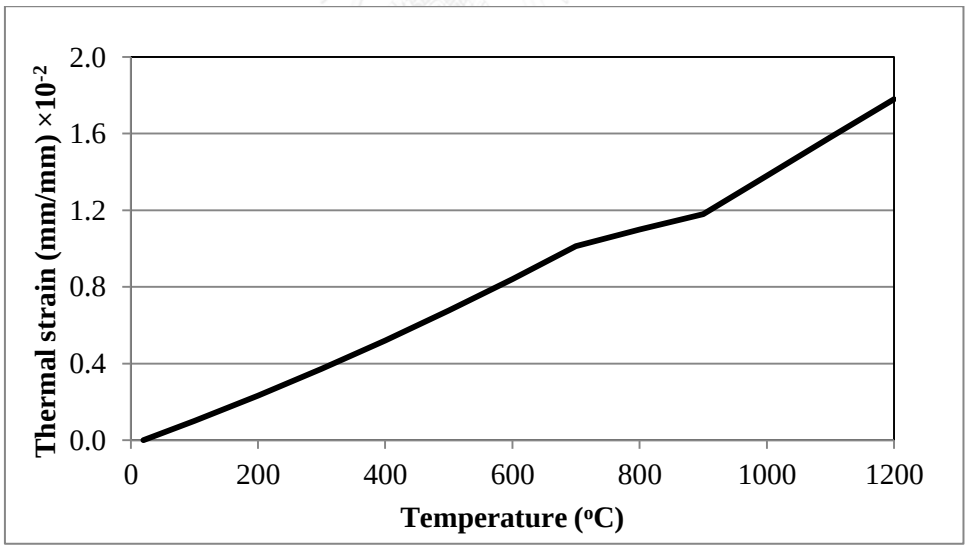

Figure 3.20: Thermal strain of steel rebar at elevated temperature (Eurocode3 2005).

CHAPTER 4
VERIFICATION OF THE FINITE ELEMENT METHODS

As mentioned in the previous chapter, load-bearing fire tests are conducted for the current study to examine the efficacy of the proposed model. Details of the test setup, the finite element model used and the comparison between the test and modeling results are presented below.

4.1 Description of the Fire Tests

Load-bearing fire tests were carried out on two precast concrete walls W1 and W2 having identical dimensions of 3420 mm in width, 2650 mm in height and 120 mm in thickness. Figure 4.1 shows the details of the wall specimens. Each concrete wall is reinforced with a single layer of four 12 mm steel deformed bars in the vertical direction and a 250 mm × 250 mm grid of 8 mm deformed bars at the middle of the wall thickness. The tested tensile strength at normal temperature of the 12 mm and 8 mm rebars were 392 MPa and 540 MPa, respectively. The concrete mixtures containing polypropylene (PP) fibers in the proportion of 0.05% (0.2%) by volume is used to cast the walls W1 (W2), in order to prevent concrete spalling that may occur on the exposed face of these walls during the fire test. The compressive strength of concrete at 28 days was 43 MPa for walls W1 and W2. The walls are installed with dowel connections to the upper and lower cross ties to simulate the actual installation details used in practice for load-bearing walls in high-rise buildings. The applied load on each concrete wall was specified at 410 kN, which is 10% of the buckling capacity of the wall at normal temperature as calculated according to (ACI 318-11, 2011). This load level represents a general service level load in practice. During the fire test, the temperature distribution throughout the wall was examined using 45 type-K thermocouples installed at 5 different layers (with 9 points in each layer) as shown in Figure 4.2. The vertical deflections of the concrete wall were also recorded using two linear variable differential transducers (LVDTs) with a measurement range of ±50 mm, while the horizontal displacements of the wall were monitored using five LVDTs

with a measurement range of ±200 mm as shown in Figure 4.3. The vertical and horizontal displacements of the wall were monitored against the limiting deflection criteria of ISO834-1 (1999) throughout the course of the fire test. In addition, photographs of the unexposed face of the wall were periodically taken to observe the crack patterns.

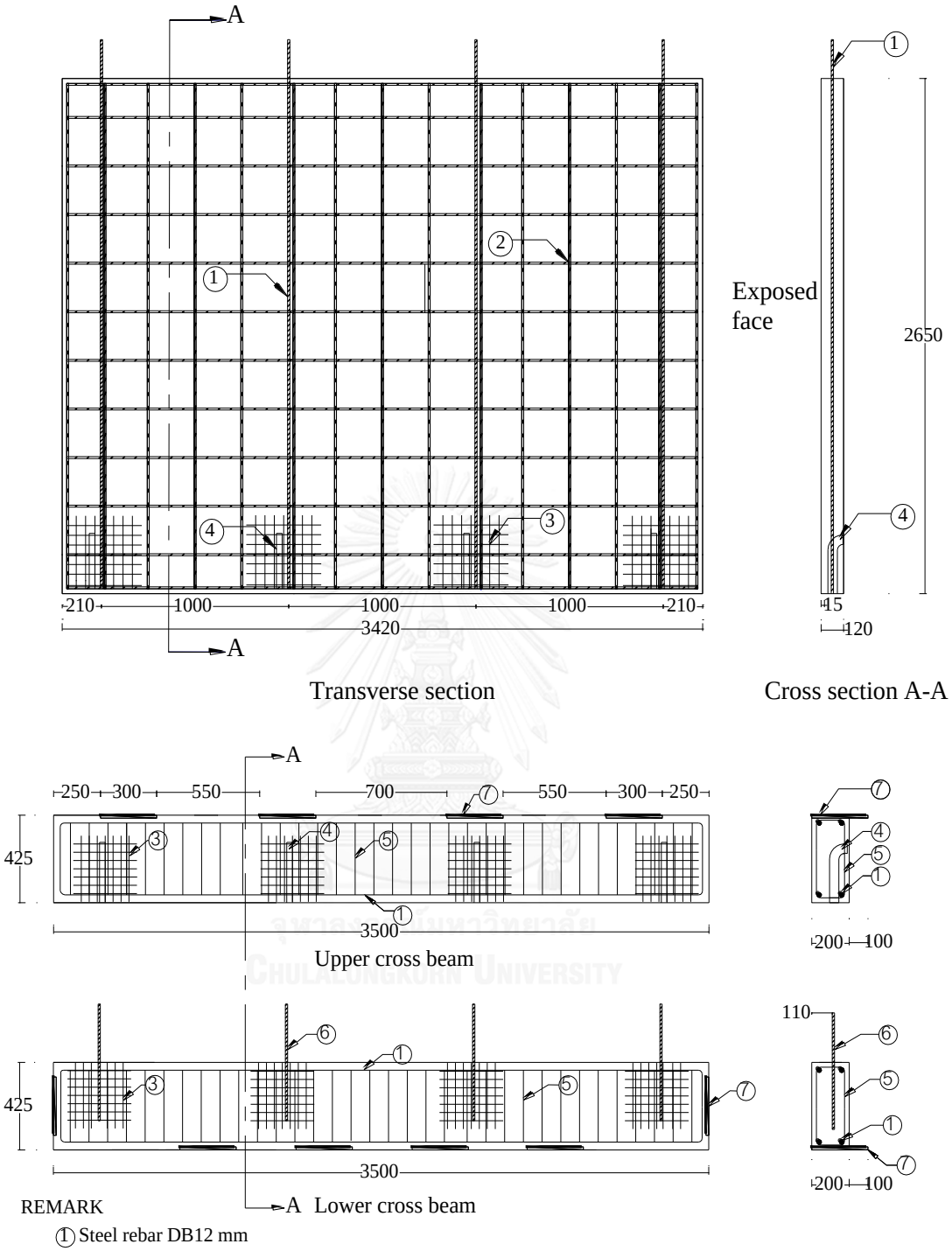

Figure 4.1: Details of wall specimens W1 and W2.

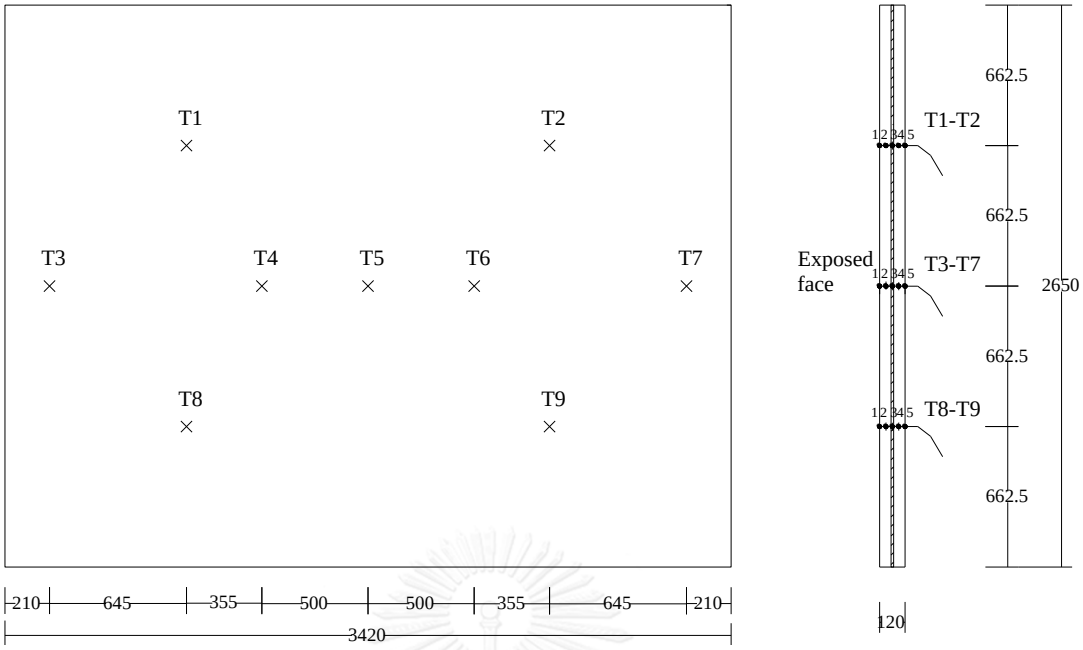

Unit: mm

Figure 4.2: Location of thermocouples.

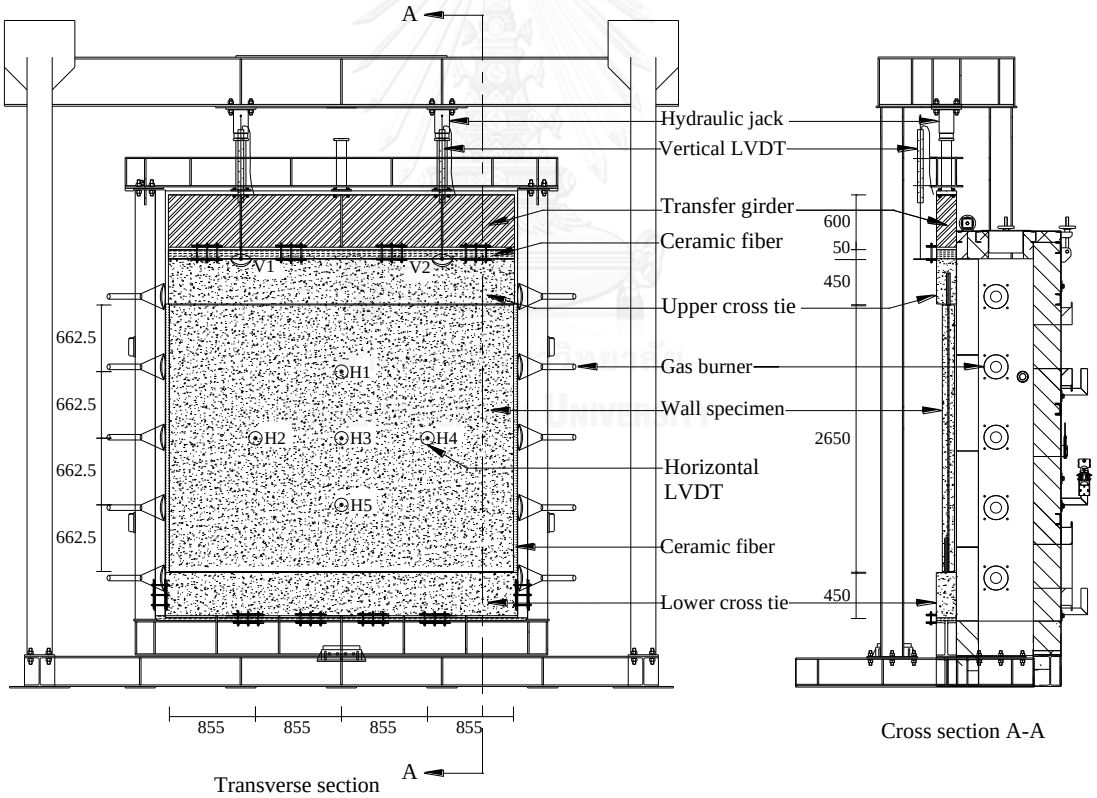

Unit: mm

Figure 4.3: Overview of the fire test setup.

4.2 Finite Element Model

A series of finite element models are examined using different meshes of SOLID70 elements for the thermal model (SOLID65 for the structural model) in order to determine the finite element mesh to be used for further analyses. The different meshes are designated as M1, M2, M3 and M4 as illustrated in Figure 4.4. Note that the element size is restricted by the location of the steel rebar and the steel grid since in the proposed modeling scheme the concrete and the steel elements share the same nodes.

The average temperatures at the middle of the wall thickness with respect to the number of elements for each mesh are illustrated in Figure 4.5 for wall W1 and Figure 4.6 for wall W2, respectively. Meanwhile, the horizontal displacement at the wall mid-height for different meshes for walls W1 and W2 are plotted in Figure 4.7 and Figure 4.8. It can be seen from these figures that the temperature and displacement obtained from mesh M3 (31,376 elements) begin to converge with 0.01% and 0.7% deviations, respectively, compared to mesh M4 (56,816 elements). Mesh M3 is therefore used for further investigations.

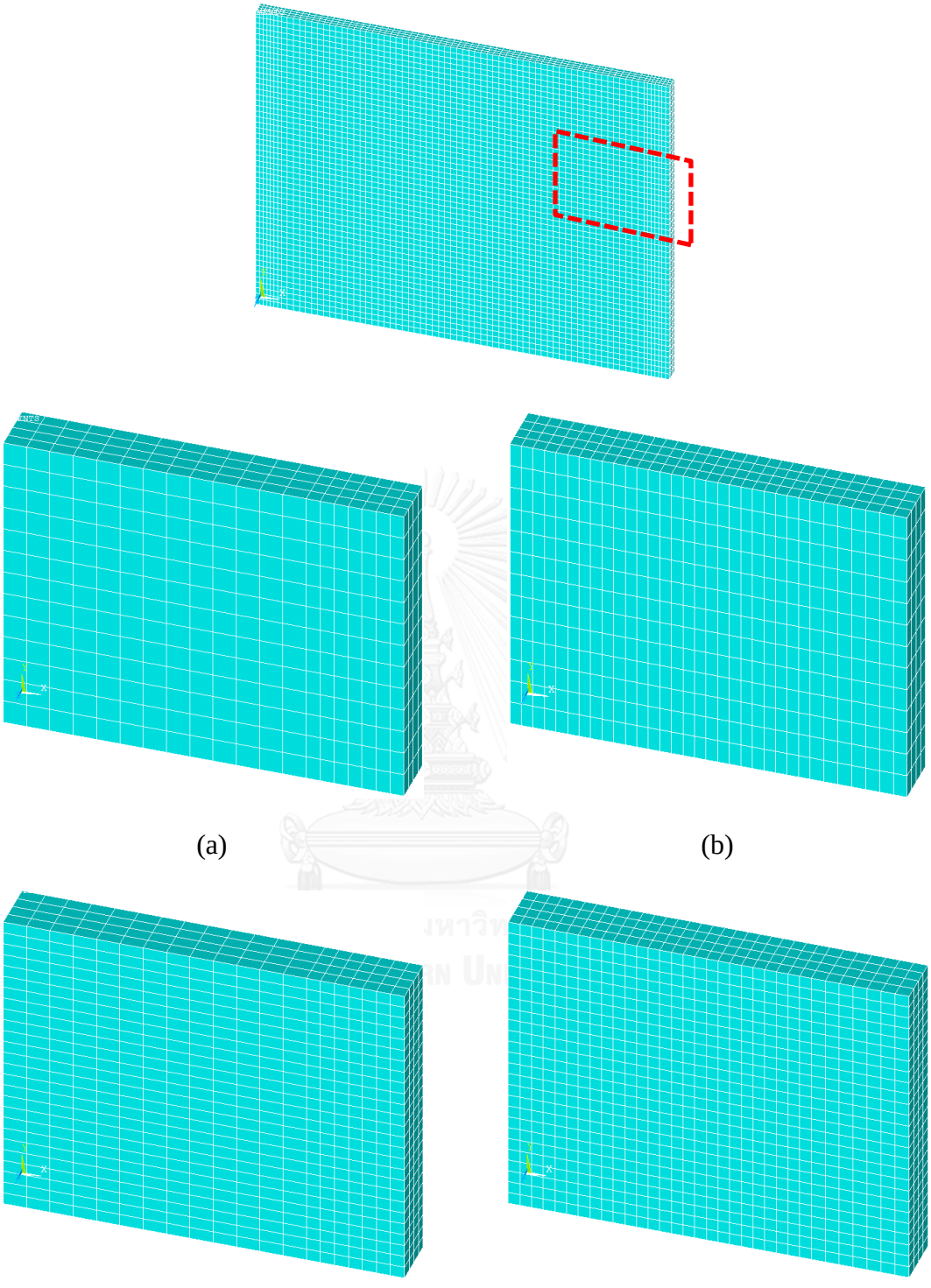

(a) (b)

(c) (d)

Figure 4.4: Finite element models with different meshes: (a) M1 (15,688 elements); (b) M2 (28,408 elements); (c) M3 (31,376 elements); (d) M4 (56,816 elements).

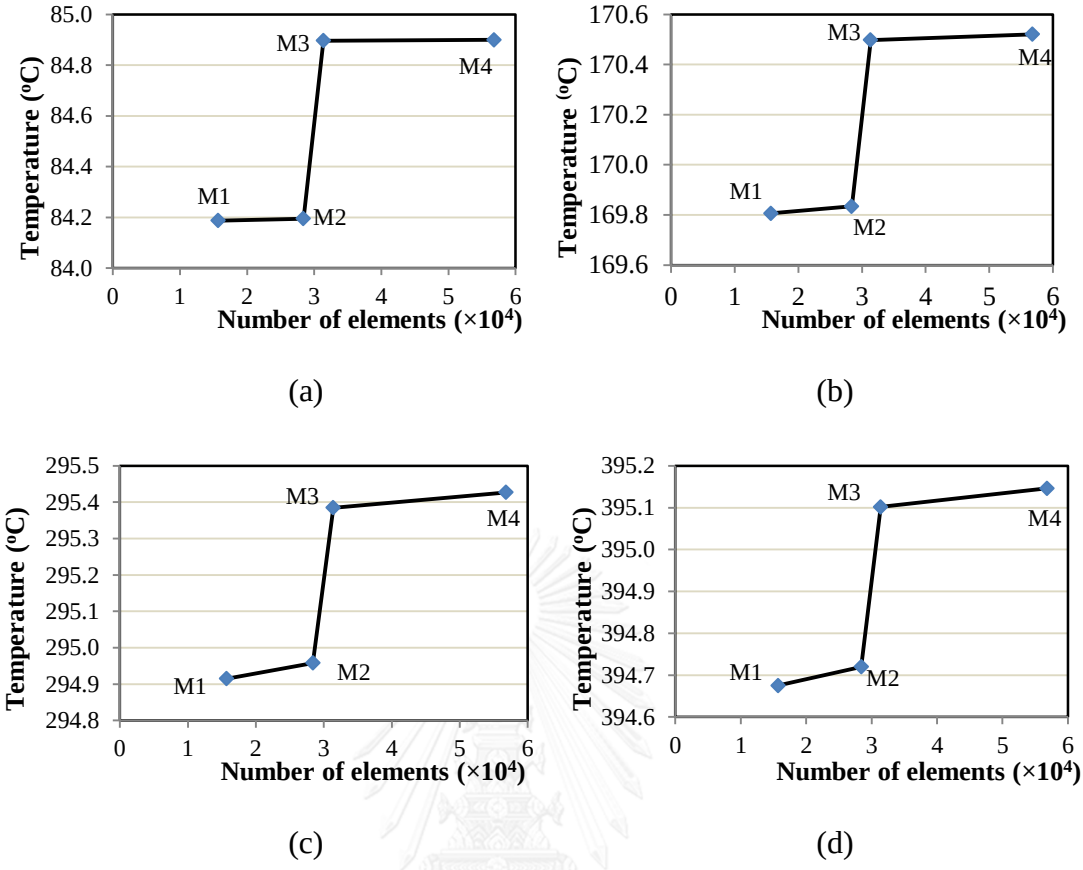

Figure 4.5: Mean temperature at the middle layer of wall W1 for different meshes with respect to varying heating periods: (a) 30 min; (b) 60 min; (c) 120 min; (d) 180 min.

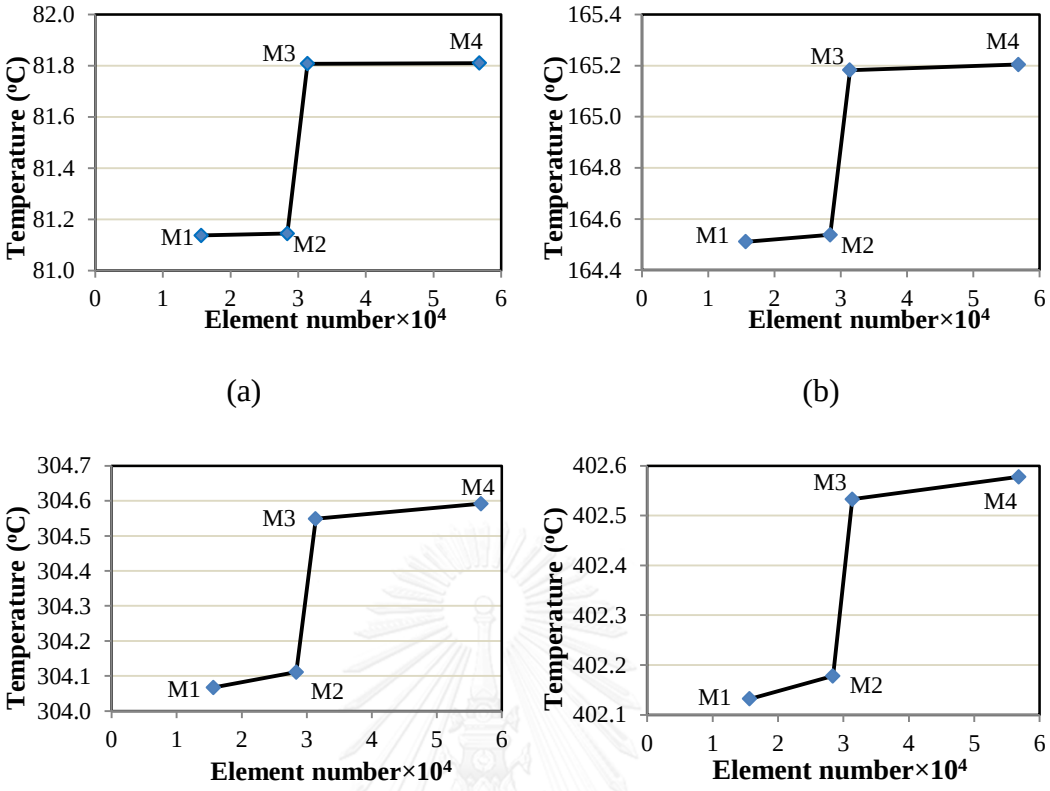

Figure 4.6: Mean temperature at the middle layer of wall W2 for different meshes with respect to varying heating periods: (a) 30 min; (b) 60 min; (c) 120 min; (d) 180 min.

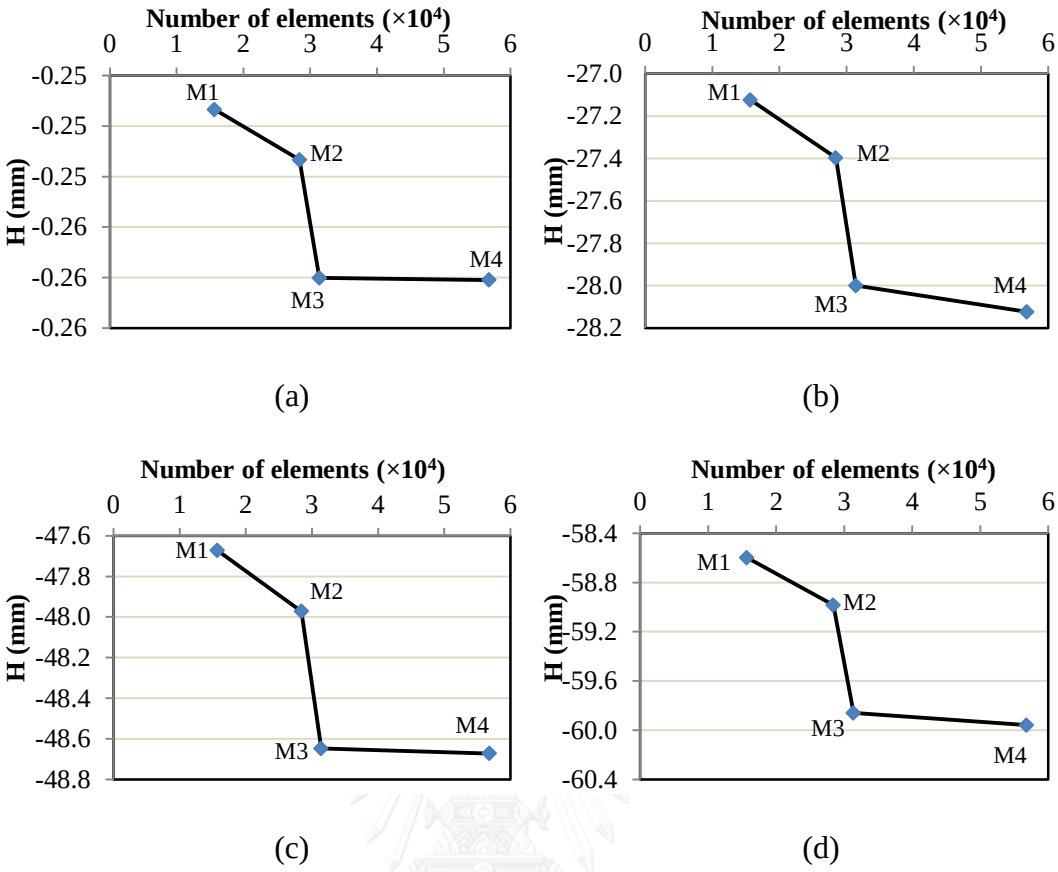

Figure 4.7: Mid-height displacement of wall W1 for different meshes with respect to varying heating periods: (a) 30 min; (b) 60 min; (c) 120 min; (d) 180 min.

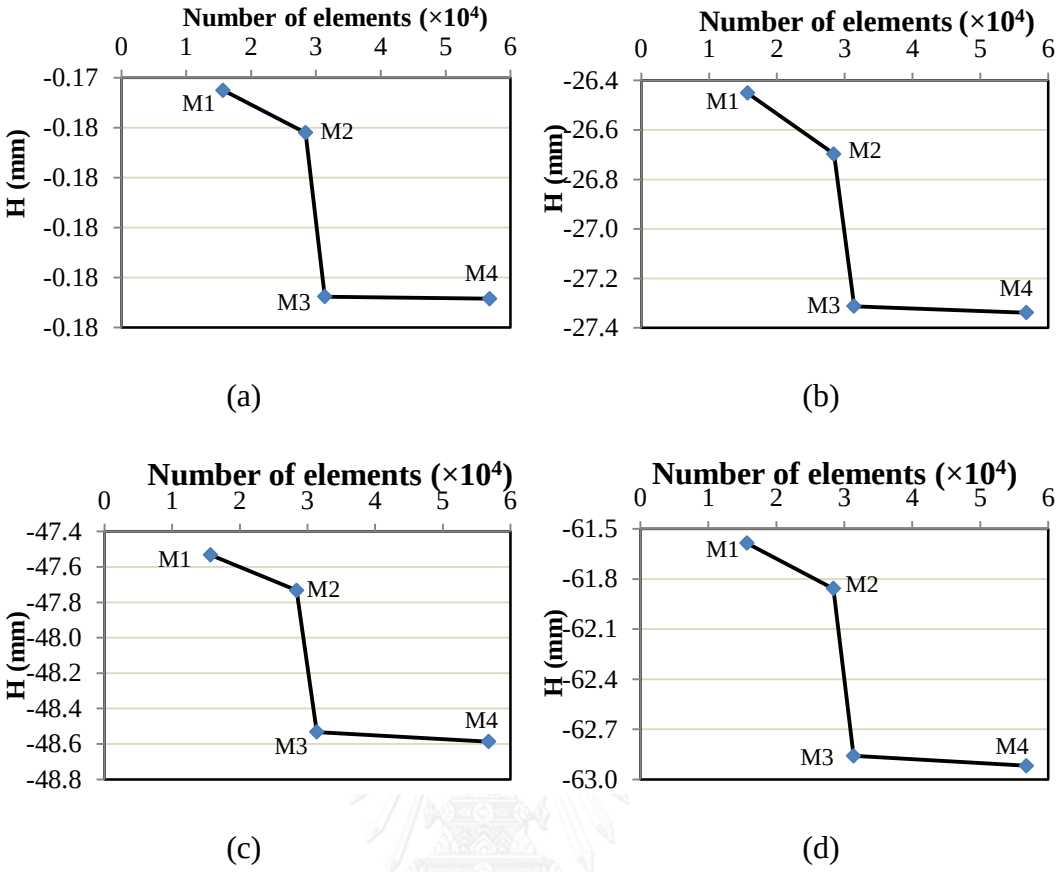

Figure 4.8: Mid-height displacement of wall W2 for different meshes with respect to varying heating periods: (a) 30 min; (b) 60 min; (c) 120 min; (d) 180 min.

4.3 Thermal Response

The thermal model is verified by comparing the predicted temperatures with the measured temperatures obtained from the fire tests conducted in the current study, as well as the temperature data taken from previous studies in the literature (Lie and Williams-Leir 1979, Lim, Buchanan et al. 2004). The thermal properties used in the proposed model are taken from Eurocode2 for concrete and Eurocode3 for steel rebar (see section 3.2.1.1 and 3.2.1.2). The average of the exposed surface temperatures measured during the fire test is used as the applied thermal load, while the convection and radiation are imposed at the unexposed side of the wall as mentioned in section 3.2.1.

4.3.1 Temperature History from the Fire Tests

The predicted and the measured temperatures at different layers of the walls W1 and W2 are plotted in Figure 4.9 (a) and Figure 4.9 (b), respectively. The measured temperature is shown as the average of the nine thermocouple readings in each layer (Figure 4.2). It is seen that the average temperatures in each layer of the two walls are slightly different and increase in similar trends. However, wall W2 shows lower temperatures in its inner layers as compared with the wall W1. This is possibly due to the different thermal conductivity and specific heat of various concretes resulted from the increase of PP fiber contents in the concrete mixture for wall W2. The variation in thermal properties of concrete is not taken into account in the current study.

The temperatures predicted by the thermal model are in good agreement with those measured during the fire tests for both walls. The discrepancies between the measured and the predicted temperatures are observed to be in the range of 20-50 °C (2-5% of the maximum temperature of 950 ^{o}C). The temperature deviation may be caused by variation of the actual thermal conductivity and specific heat of concrete mixed with PP fibers from those specified by the Eurocode2 and Eurocode3. Based on the temperature data, the thermal model provides reasonably accurate predictions through the wall thickness. As such, the proposed thermal model can be used to predict the temperatures within the precast concrete load-bearing walls exposed to fire.

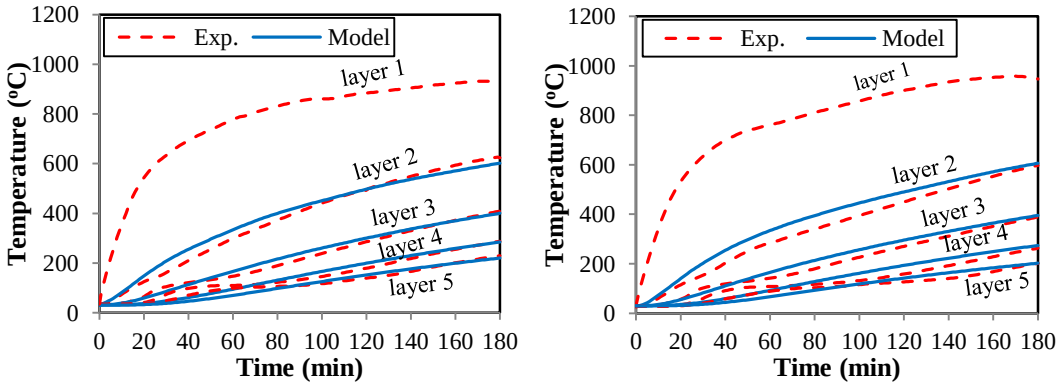

(a) W1 (b) W2

Figure 4.9: Predicted and measured temperatures of the walls.

4.3.2 Temperature History from Previous Studies

In order to further examine the validity of the proposed thermal model, a comparison is made between the predicted and the measured temperatures taken from the experimental studies in the literature on reinforced concrete slabs exposed to fire (Lie and Williams-Leir 1979, Lim, Buchanan et al. 2004). Lim, Buchanan et al. (2004) has conducted a fire test on a flat slab with the dimensions of 3300 mm in length, 4300 mm in width and 100 mm in depth. The slab was subjected to fire on the soffit for 180 min. The temperatures were recorded at 5 different layers, i.e. 0, 25, 50, 75 and 95 mm from the exposed face of the slab. Another fire test has been conducted by Lie and Williams-Leir (1979) on a slab with the dimensions of 800 mm in width, 900 mm in length and 150 mm in thickness. The slab was subjected to fire on the bottom side for 360 min. The temperatures were recorded during the fire test at the exposed face, the mid-depth and the unexposed face of the slab.

Note that the thermal properties of concrete and steel rebar based on Eurocode2 and Eurocode3 are adopted for the finite element model.

Figures 4.10 (a), (b) show the comparison between the predicted temperatures and the measured temperatures for these two fire tests. The maximum deviations are found to be around 35 ^{o}C, which is 3% of the maximum temperature of 1050 ^{o}C, at the mid-depth for Lim, Buchanan et al. (2004) and 40 ^{o}C, which is 3% of the maximum temperature of 1120 ^{o}C, at the unexposed face for Lie and Williams-Leir (1979), respectively. Therefore, the proposed finite element model is deemed reliable as a tool for predicting temperatures within reinforced concrete members that are exposed to fire.

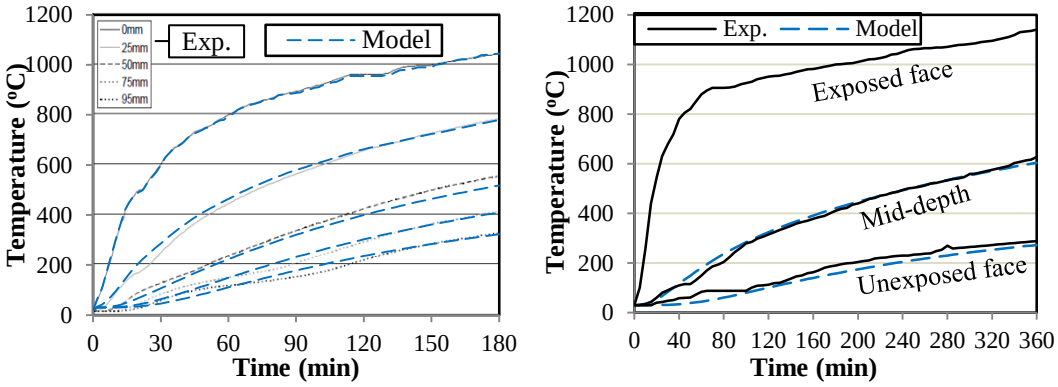

(a) (b)

Figure 4.10: Comparison between predicted and measured temperatures for RC slabs from previous studies: (a) Lim, Buchanan et al. (2004); (b) Lie and Williams-Leir (1979).

4.4 Structural Response

The predicted horizontal displacements obtained from the structural model are compared with those measured during the fire tests as illustrated in Figure 4.11-4.12. The wall is modeled as a simply supported taking into account the temperature-dependent mechanical properties of concrete and steel rebar according to Eurocode2 and Eurocode3 as previously discussed in sections 3.2.2.1 and 3.2.2.2. The load of 410 kN (10% of the bucking capacity of the wall at normal temperature) is applied as a uniformly distributed load on the upper end of the wall. It is seen that the maximum horizontal displacements of wall W1 as predicted by the structural model match well with the measurements taken throughout the fire test. However, the structural model overestimates the horizontal displacements of wall W2 as compared with the test results after the first 20 min, with a maximum deviation of around 7 mm (7% of the maximum displacement of 60 mm). Note that the LVDT at H1 malfunctioned after 88 min from the initiation of the fire test. Based on the above comparison, it can be concluded that the structural response obtained by the proposed model is reasonably accurate, particularly for wall W1 with the PP fiber content of 0.05% by volume in the concrete mixture.

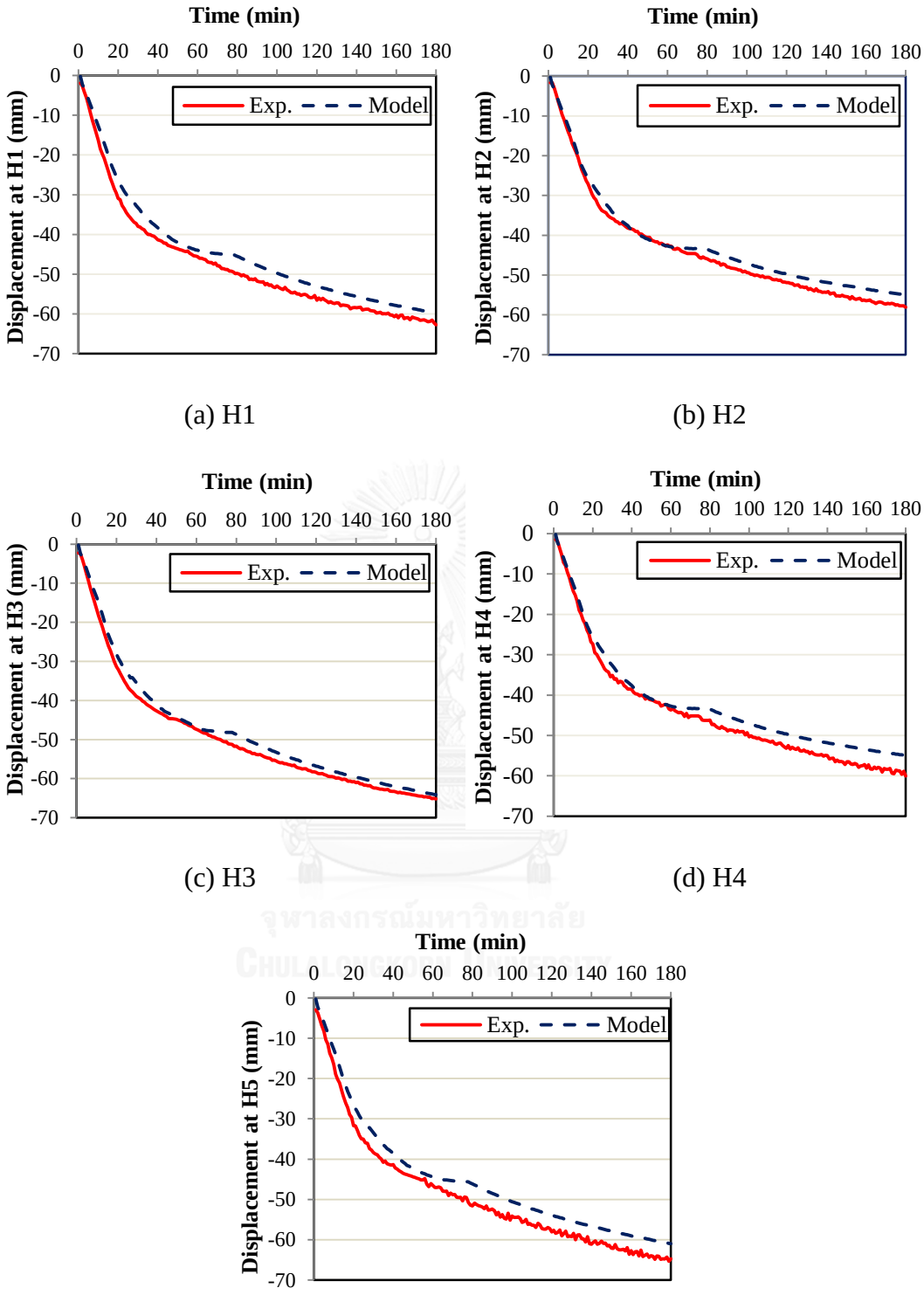

Figure 4.11: Time-displacement curves for wall W1 at locations H1-H5, (see Fig. 43. for location of H1-H5).

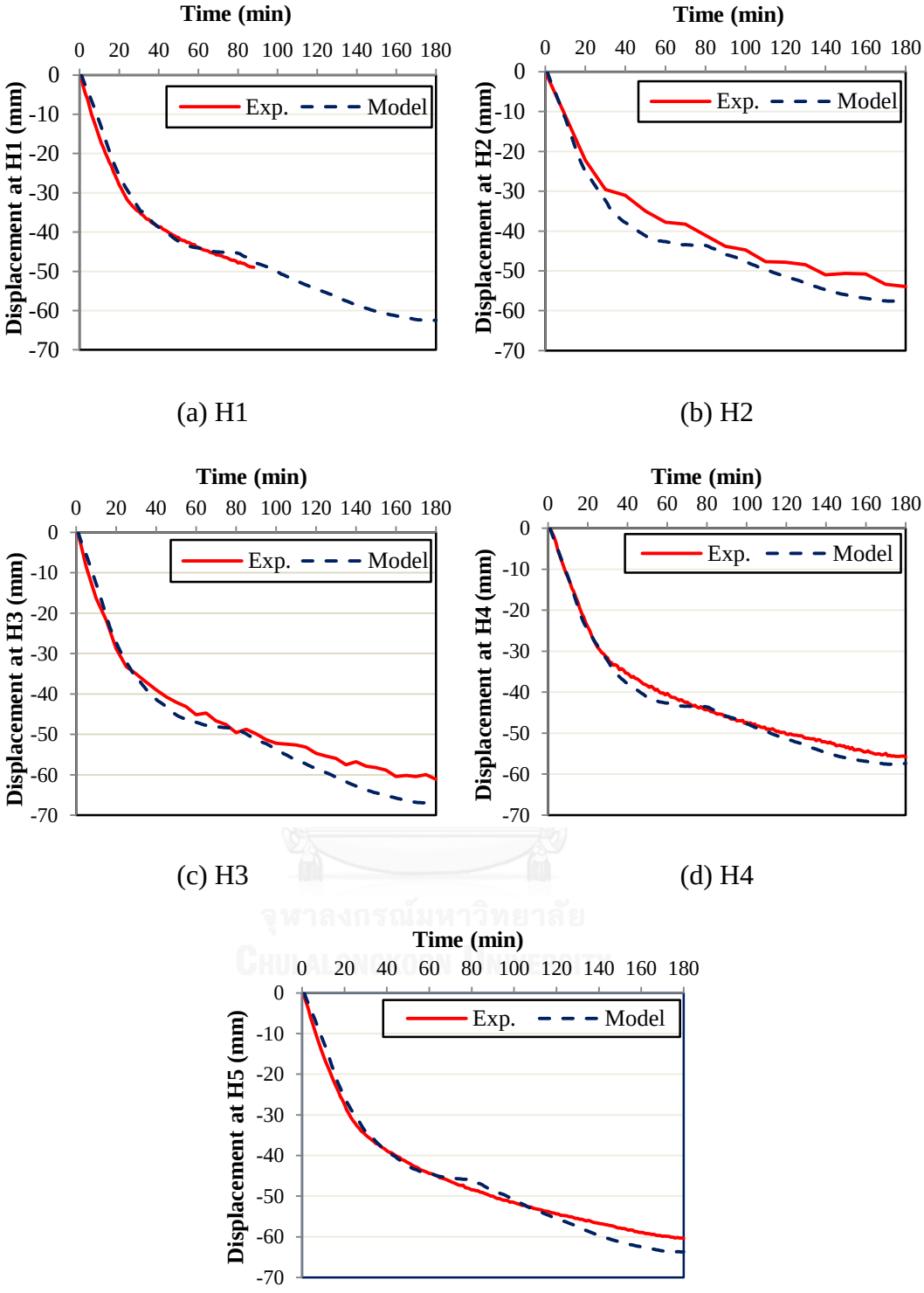

Figure 4.12: Time-displacement curves for wall W2 at locations H1-H5, (see Fig. 4.3 for location of H1-H5)

4.5 Crack Pattern

The photographs taken during the fire test and the graphical representations of crack planes obtained from the finite element model for the walls W1 and W2 are shown in Figures 4.13 and 4.14, respectively, in which the plane of cracks is represented by a straight line in the direction perpendicular to that where the principal stress exceeds the tensile strength of concrete. It can be observed that the crack patterns of both walls as obtained from the proposed model are in line with the test results. The cracks on the unexposed face are initiated in the vertical direction at 17 min and 21 min for walls W1 and W2, respectively. The occurrence of these vertical cracks is mainly due to the thermal expansion of the wall in the horizontal direction with no restraint on the vertical edges. In addition, tensile stresses are induced in the horizontal direction from the effect of Poisson's ratio as the load level is increased. Meanwhile, the horizontal cracks of walls W1 and W2 are observed after 40-min and 43-min heating duration, respectively. The horizontal cracks are initiated near the edges and propagate to the middle of the wall. In addition to the vertical and horizontal cracks, inclined cracks are also observed around the corners of the walls. The inclined cracks are initiated at about the same time as the horizontal cracks.

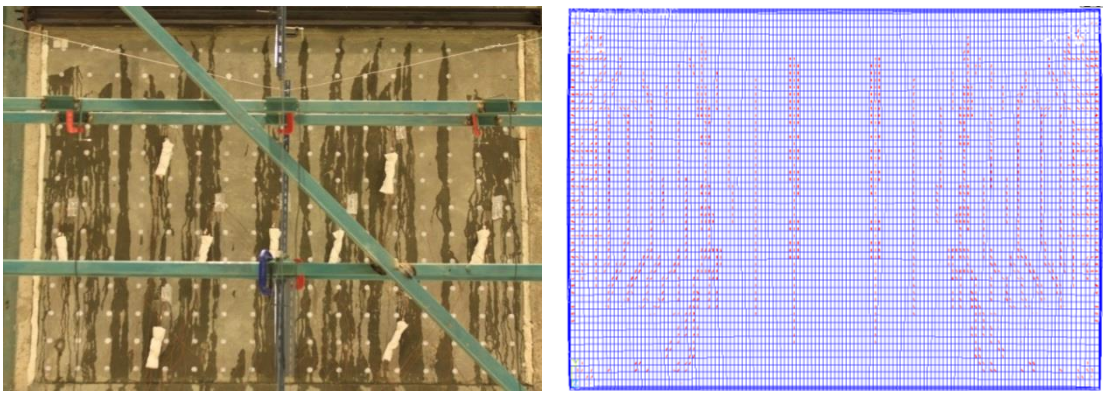

(a) 20 min

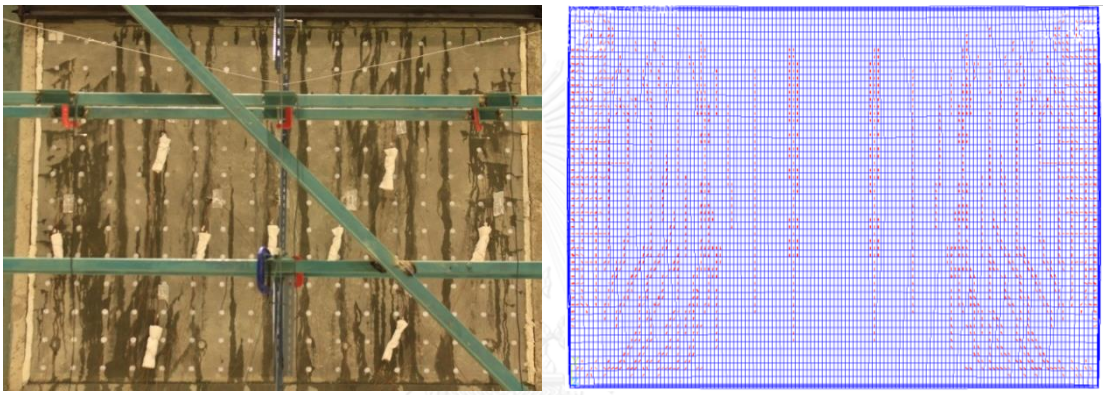

(b) 40 min

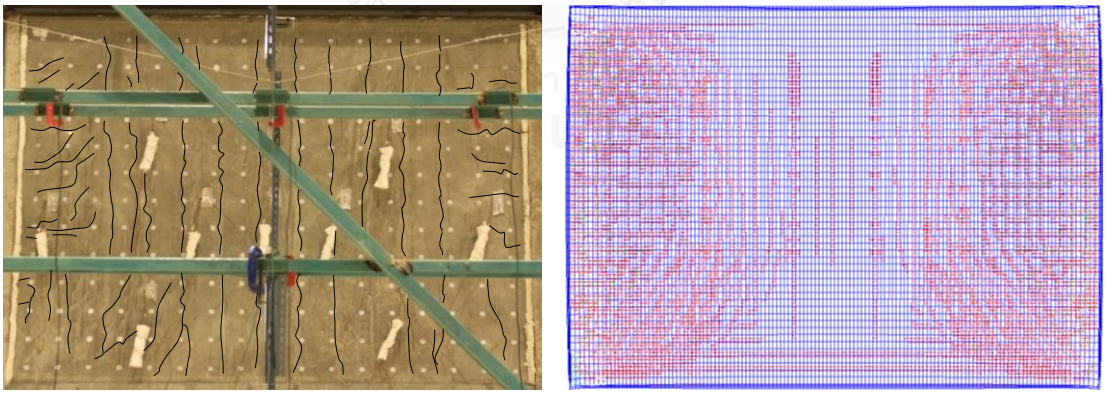

(c) 180 min

Figure 4.13: Comparison between the predicted and observed crack patterns for wall W1 with respect to time.

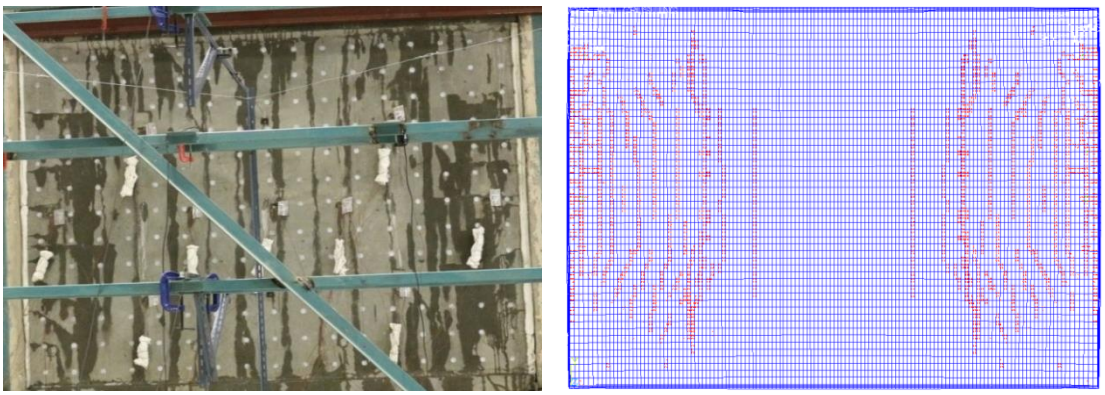

(a) 20 min

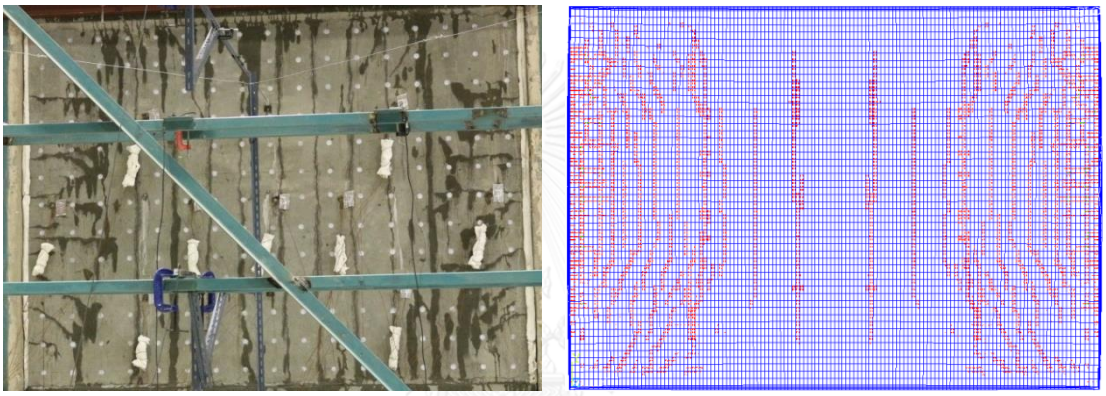

(b) 40 min

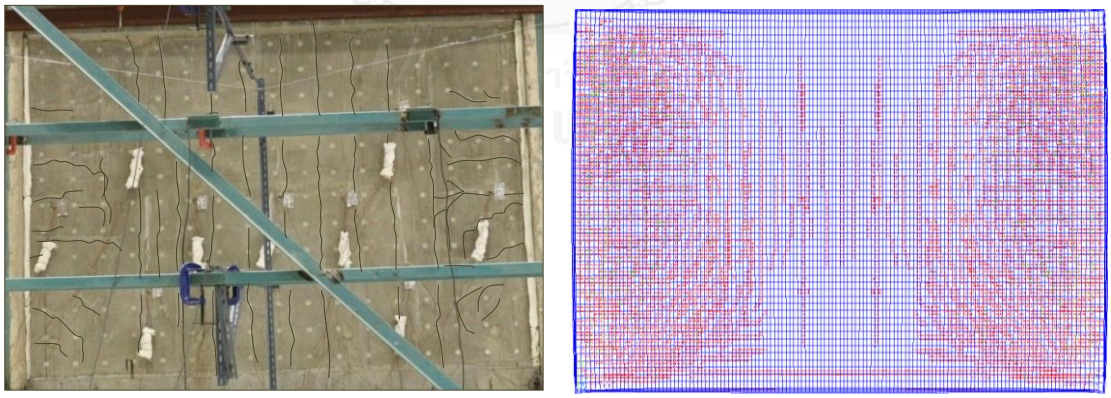

(c) 180 min

Figure 4.14: Comparison between the predicted and observed crack patterns for wall W2 with respect to time.

CHAPTER 5
PARAMETRIC STUDIES AND ESTIMATION OF THE FIRE RESISTANCE OF PRECAST CONCRETE LOAD-BEARING WALLS

This chapter presents the results of a parametric study that has been conducted using the proposed FE model to investigate the effect of load level, slenderness ratio and rotational restraint on the load-bearing capacity of the precast concrete walls with one-sided exposure to ISO 834-1 standard fire. Furthermore, a set of simplified equations are proposed using polynomial functions for estimating the fire resistance rating (FRR) of the walls based on the load level and slenderness ratio. Finally, the capability of the model to handle openings and unsymmetrical configurations is illustrated.

5.1 Effect of Load Level

The effect of varying load levels is investigated for a simply supported wall. The dimensions of the wall are 3420 mm in width, 2650 mm in height and 120 mm in thickness. The wall is subject to different values of axial load at the specified load ratios of 0.1, 0.2, 0.3, 0.4 and 0.5 as illustrated in Figure 5.1. Note that the thickness of the wall is kept constant herein to avoid the impact of thermal gradient on the overall structural behavior. In the finite element analysis, cracking of a concrete element occurs when the tensile strength of concrete is exceeded. Crushing of a concrete element occurs when the principal stresses reach the failure criteria of Willam and Warnke (1975) (see section 3.2.2.1). After crushing, the elastic modulus of concrete is set to zero in all directions and the element local stiffness becomes zero. This results in large displacements and divergence of the finite element solution. At this point, the wall is regarded as reaching its load-bearing capacity and its fire resistance rating can be determined.

The mid-height horizontal displacements of the wall for different load levels are plotted in Figure 5.2. The termination point of each curve indicates the time to failure of the load-bearing wall as obtained from the FE model. It can be seen that

failure of the wall under the load ratios of 0.2, 0.3, 0.4 and 0.5 occurs at 170 min, 72 min, 33 min and 19 min, respectively, while the wall does not fail under the load ratio of 0.1 within the heating duration of 180 min. It is evident that the fire resistance rating of the load-bearing wall decreases by up to 90% with the increasing load level. This is due to the fact that under the higher load level, larger principal stresses are induced in the concrete elements which lead to earlier crushing failure. Based on the modeling results, the 120-mm thick precast concrete walls with a load ratio exceeding 0.2 are unable to sustain a 3-hour (180 min) fire resistance period.

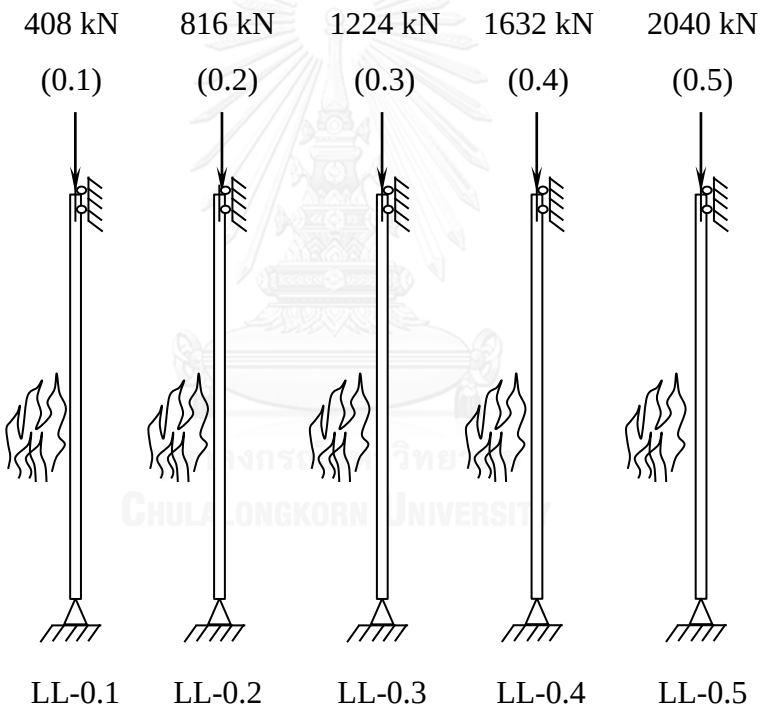

Figure 5.1: Simply supported walls with one-sided fire exposure and varying load levels, (0.1, 0.2, 0.3, 0.4 and 0.5).

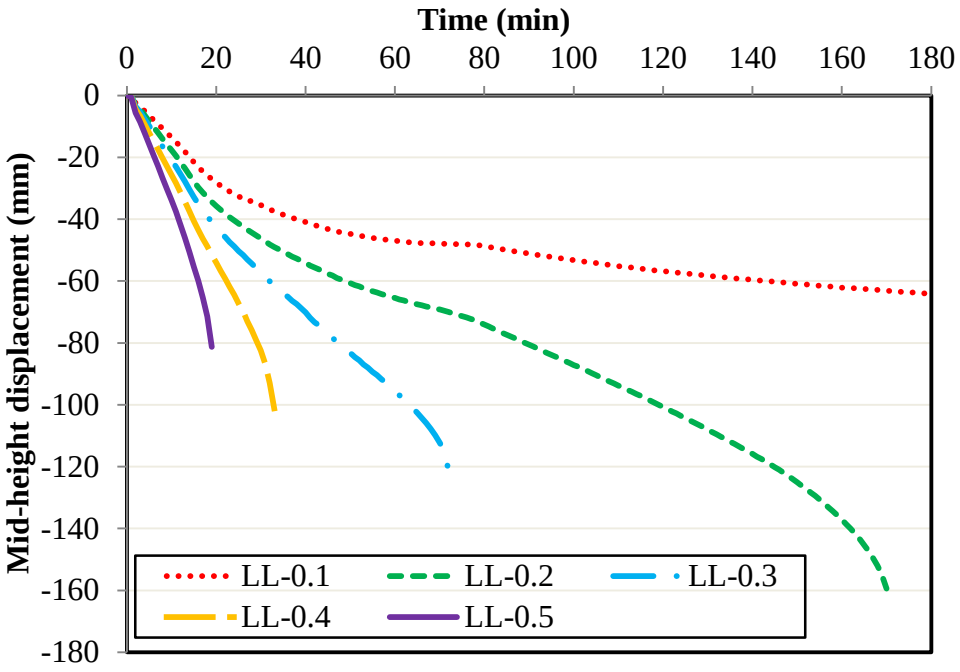

Figure 5.2: The mid-height horizontal displacements for precast concrete walls with varying load levels.

5.2 Effect of Slenderness Ratio

In order to examine the effect of slenderness ratio on the fire performance of the precast concrete wall, the same configuration of the wall as for the previous section is considered. The wall thickness and width are specified as 120 mm and 3420 mm, respectively, while the wall height is varied to obtain different slenderness ratios of 20 (SR-20), 25 (SR-25), 30 (SR-30) and 35 (SR-35) as determined by dividing the wall height by its thickness. These walls are subject to a constant axial load of 1000 kN and are exposed to fire on one side as illustrated in Figure 5.3. The maximum horizontal displacement vs. time curves for the walls obtained from the FE model are shown in Figure 5.4. It is seen that the walls with the slenderness ratio of 25, 30 and 35 have the fire resistance rating of 67, 26 and 12 min, respectively, while the wall with the slenderness ratio of 20 does not fail within the heating duration of 180 min. This clearly indicates that the walls with higher slenderness ratios are more prone to structural failure with lower fire resistance ratings by up to 93%. Further, it is observed that the failure of the wall is primarily due to buckling as evident from the

maximum stress and deflection along the wall height as illustrated in Figures 5.5-5.7. The maximum principal stresses are 24, 23 and 22 MPa for the walls with the slenderness ratios of 25, 30 and 35, respectively. According to the failure criteria of Willam and Warnke (1975), crushing of concrete occurs only for the wall with the slenderness ratio of 25. Meanwhile, for the other two walls with the slenderness ratios of 30 and 35, extremely large displacements are found at the mid-height where the maximum principal stresses are induced. The large displacements result in divergence of the finite element solution. As such, the walls can be regarded as reaching their load-bearing capacity, and the fire resistance rating can be determined. Note that detailed examinations of the principal stresses against the failure criteria of (Willam and Warnke 1975) are shown in Appendix A.

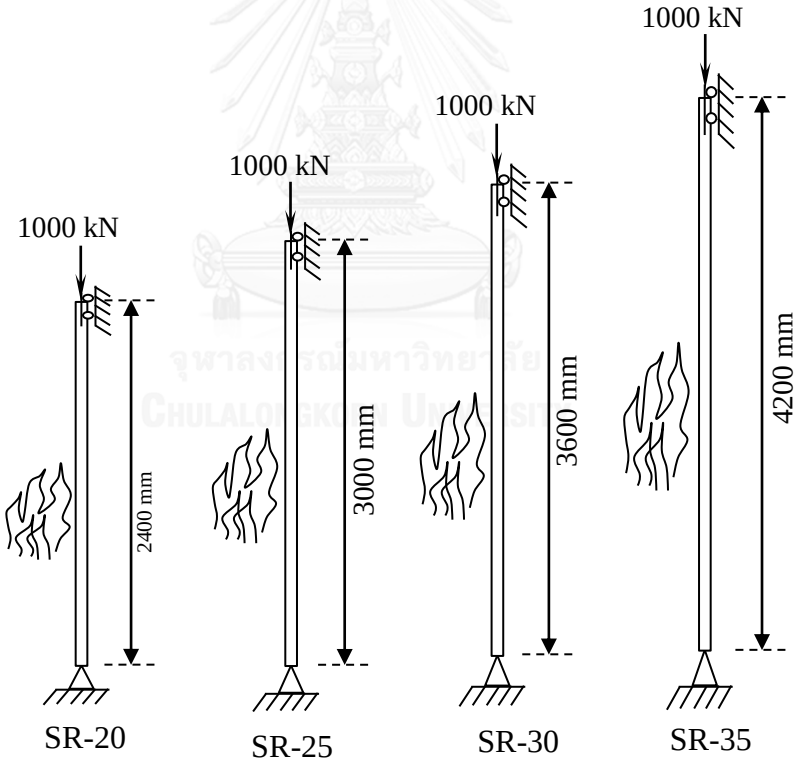

Figure 5.3: Simply supported walls with one-sided fire exposure and varying slenderness ratios.

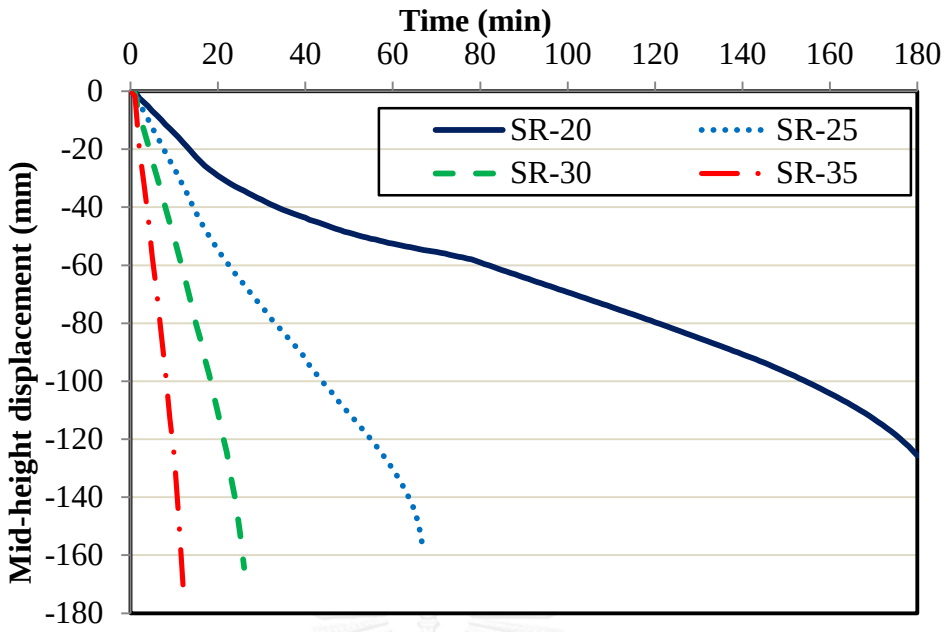

Figure 5.4: Mid-height horizontal displacements for precast concrete load-bearing walls with varying slenderness ratio.

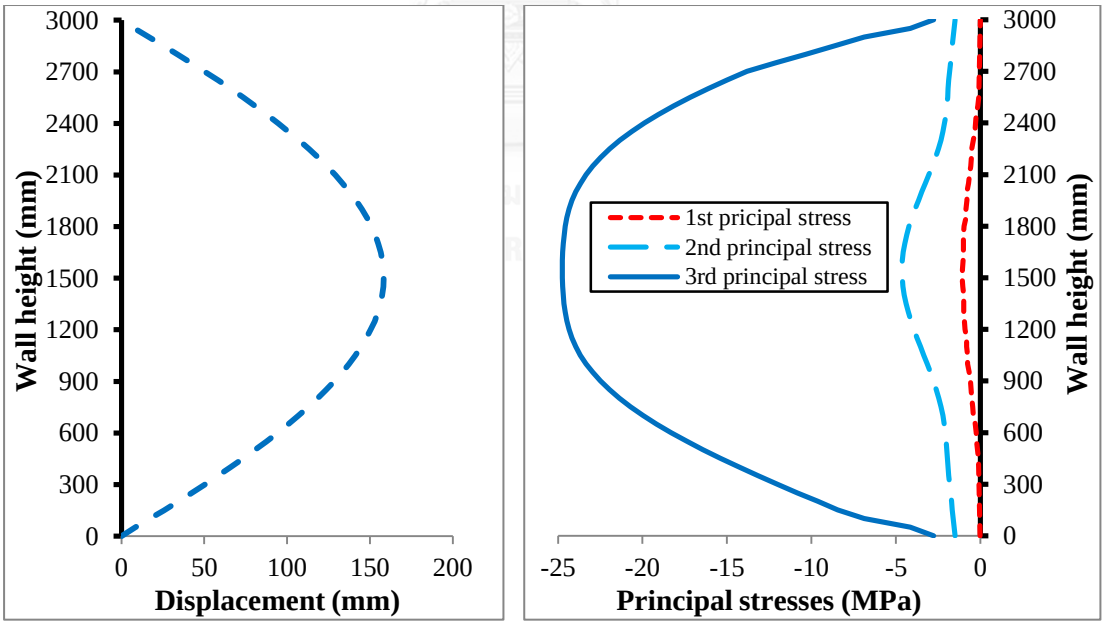

(a) (b)

Figure 5.5: Buckling characteristics of wall SR-25 at maximum displacement section: (a) horizontal displacements; (b) principal stresses.

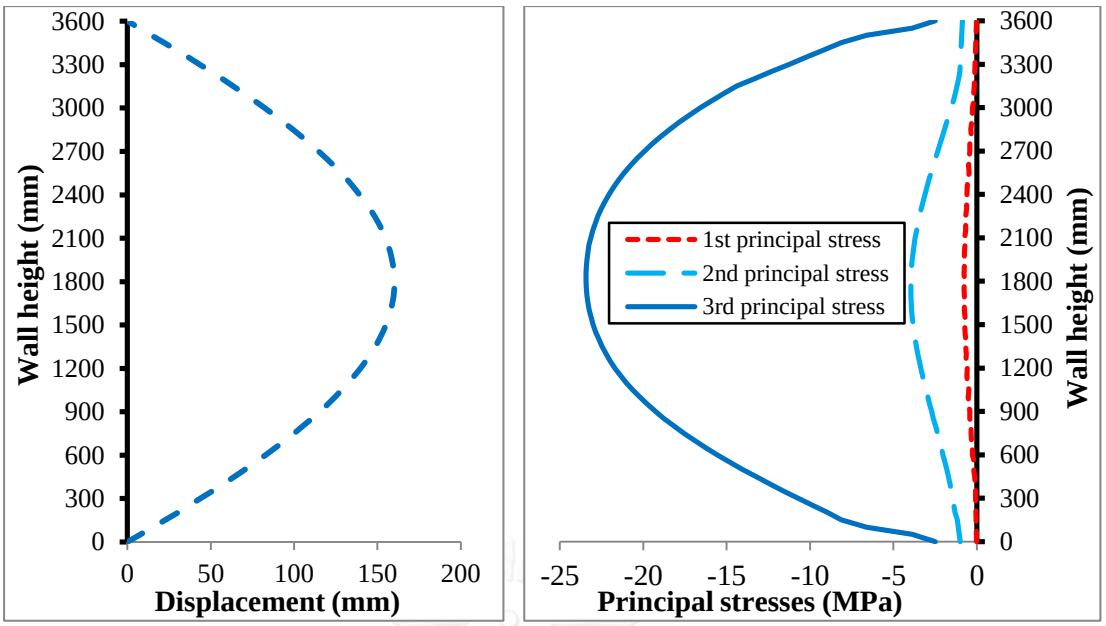

(a) (b)

Figure 5.6: Buckling characteristics of wall SR-30 at maximum displacement section: (a) horizontal displacements; (b) principal stresses.

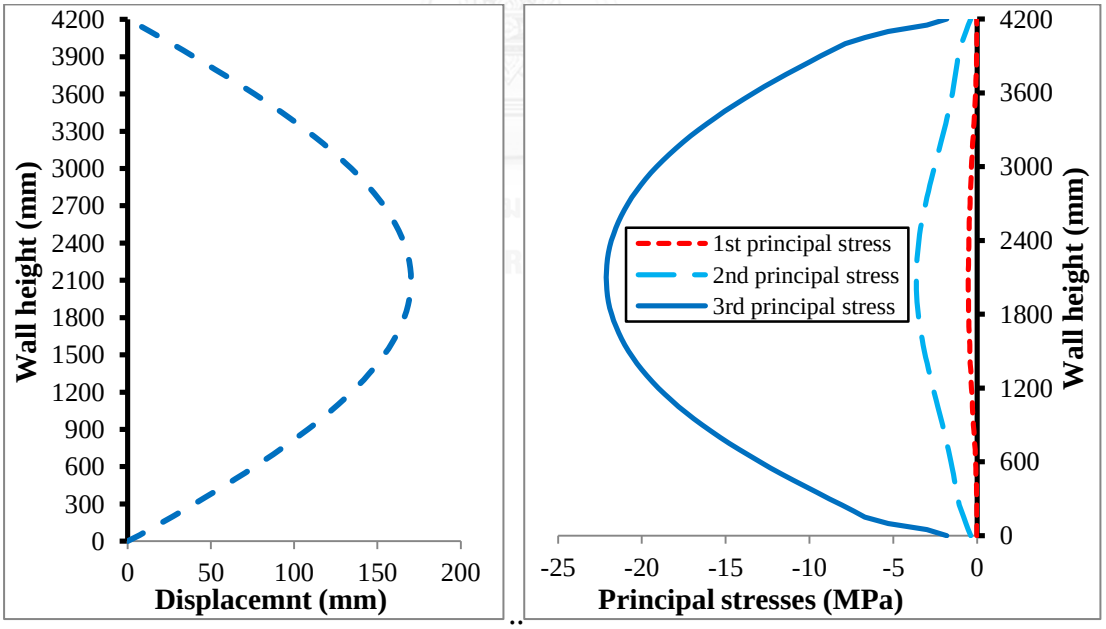

(a) (b)

Figure 5.7: Buckling characteristics of wall SR-35 at maximum displacement section: (a) horizontal displacements; (b) principal stresses.

5.3 Effect of Rotational Restraint

The rotational restraint is imposed at the wall with fixed dimensions of 3420 mm in width, 2650 mm in height and 120 mm in thickness and applied load of 2500 kN. The three different boundary conditions investigated are shown in Figure 5.8. In the first case, no rotational restraint is imposed at both ends of the wall (SS). For the second case the rotational restraint is applied at the lower end of the wall (FS). Finally, the rotational restraint is imposed at both ends of the wall as the third case (FF). Note that in all cases the walls are allowed to translate vertically at the upper support with no axial restraint. The predicted maximum deflection of the wall is shown in Figure 5.9. It can be seen from Figure 5.9 that the rotational restraint has a significant influence on the fire resistance of the load-bearing walls. The wall with no rotational restraint (SS) fails after 11 min of fire exposure, while the wall with rotational restraint at the lower end (FS) fails at 129 min. The wall with rotational restraint on both ends is observed to maintain its structural stability throughout the fire exposure period of 180 min. This indicates that the fire resistance rating of the walls increases by up to 94% when the rotational restraints are imposed at the ends of the walls. The positive effect of the rotational restraints on the fire resistance of the load-bearing wall are due to the redistribution of positive and negative moments along the wall height as illustrated in Figures 5.10-5.12. For the walls FS and FF the shift of the inflection point can be observed, which results in a relatively lower increase of the positive bending moment and the overall deflection during the fire exposure as compared to the wall SS. Note that while the maximum displacements are plotted along the vertical cross section of the wall, the maximum bending moments are obtained for the middle strip of 500 mm in width in order to better characterize the flexure behavior of the walls. The bending moments are computed from the normal stresses, in which the normal stress distribution of the walls SS, FS and FF are shown in Figures 5.13-5.15. Detailed calculations of the bending moment can be found in Appendix B.

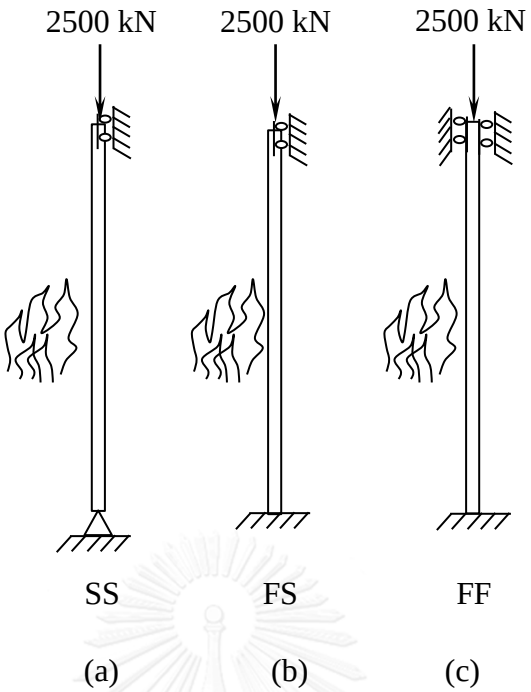

Figure 5.8: Load-bearing walls with different boundary conditions, (a) SS: No rotational restraints at both ends of the wall, (b) FS: Rotational restraints at bottom end of the wall, (c) FF: Rotational restraints at both ends of the wall.

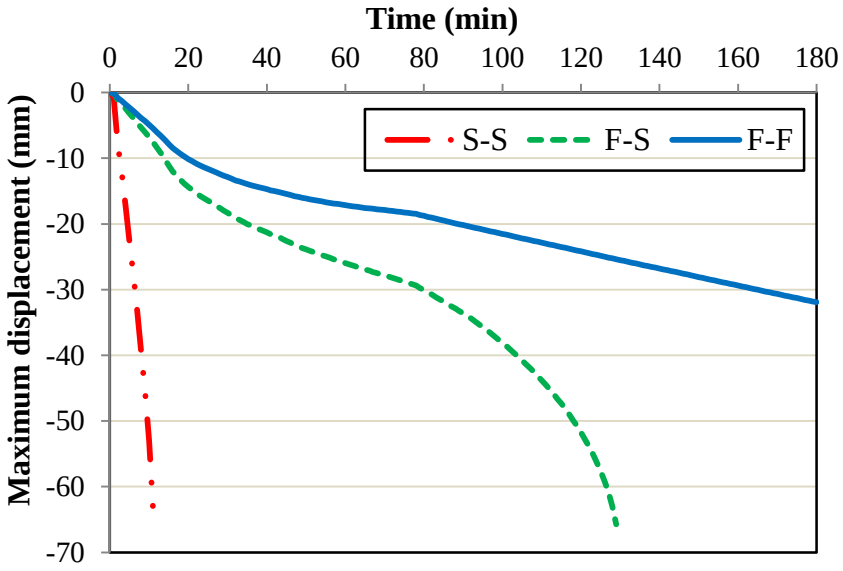

Figure 5.9: Maximum horizontal displacement of load-bearing walls with different boundary conditions.

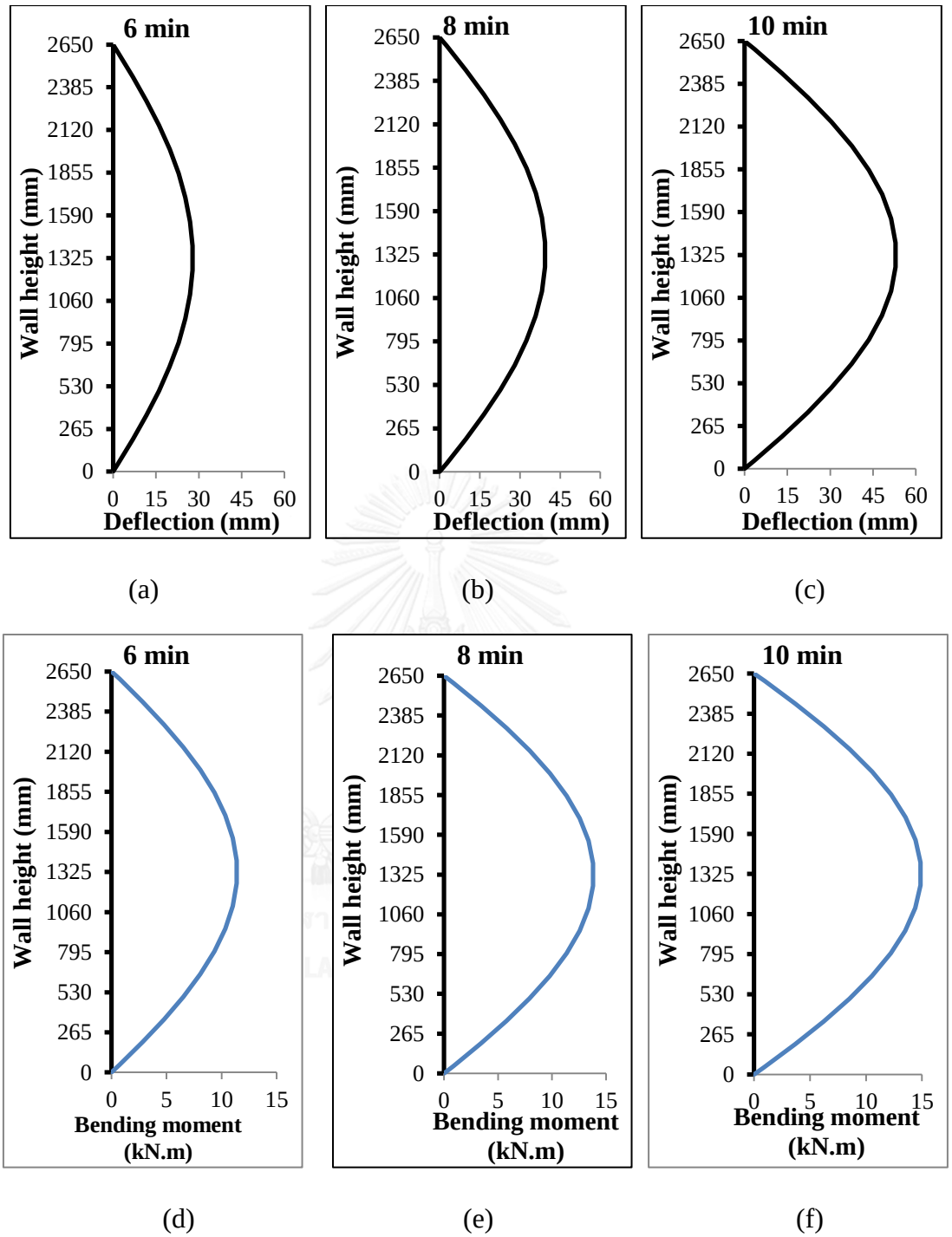

Figure 5.10: Effect of rotational restraint on wall SS: (a)-(c) deflection shape and (d)-(f) bending moment.

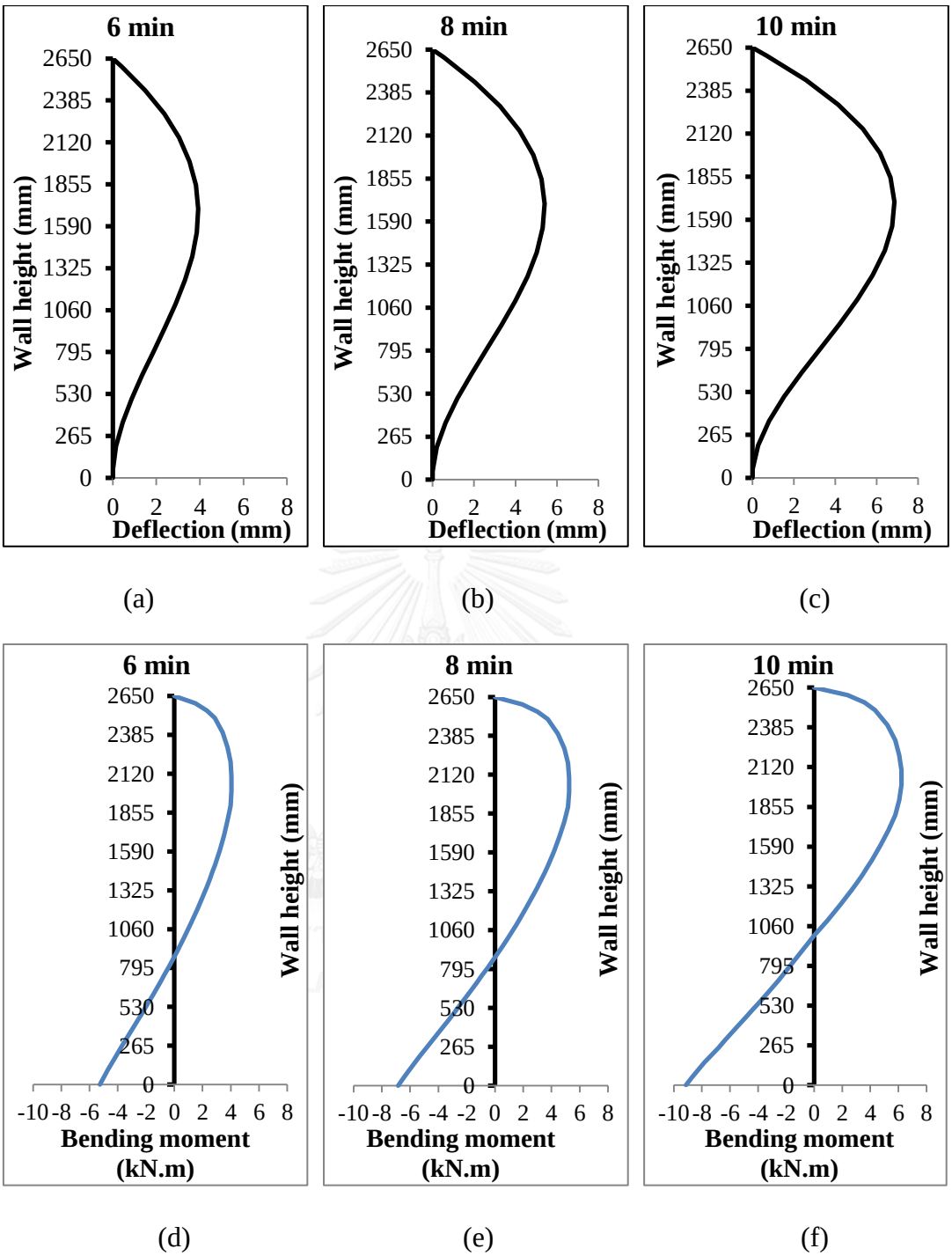

Figure 5.11: Effect of rotational restraint on wall FS: (a)-(c) deflection shape and (d)-(f) bending moment.

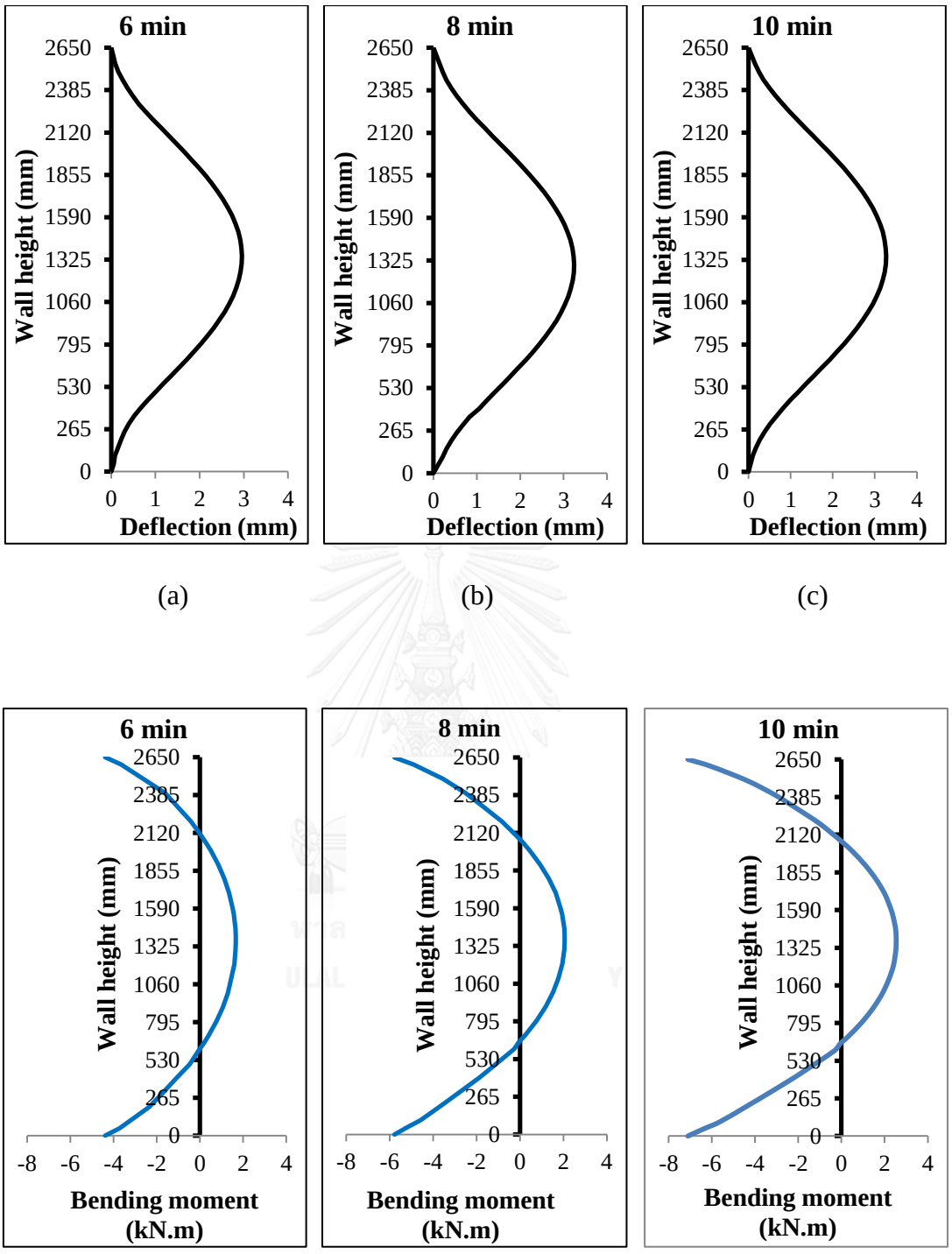

Figure 5.12: Effect of rotational restraint on wall FF: (a)-(c) deflection shape and (d)-(f) bending moment.

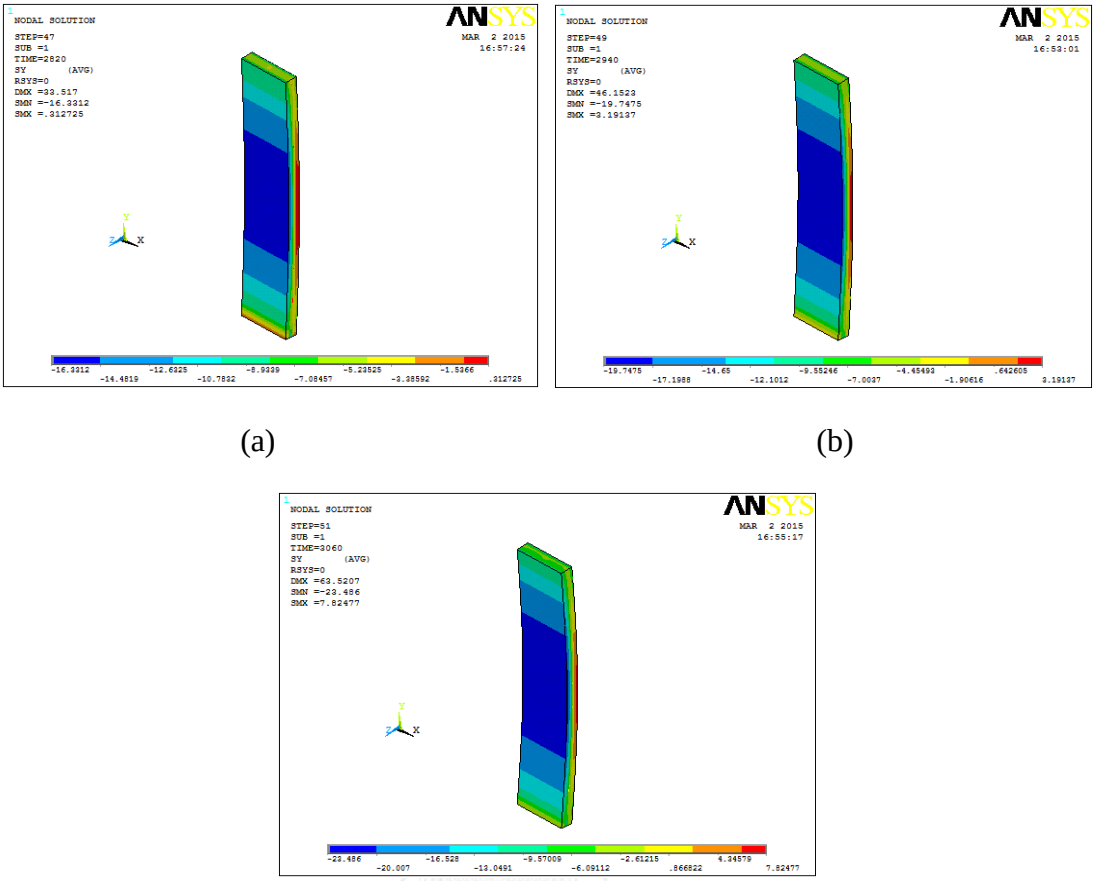

Figure 5.13: Normal stresses along the middle strip of the wall SS for different heating durations: (a) 6 min; (b) 8 min; (c) 10 min.

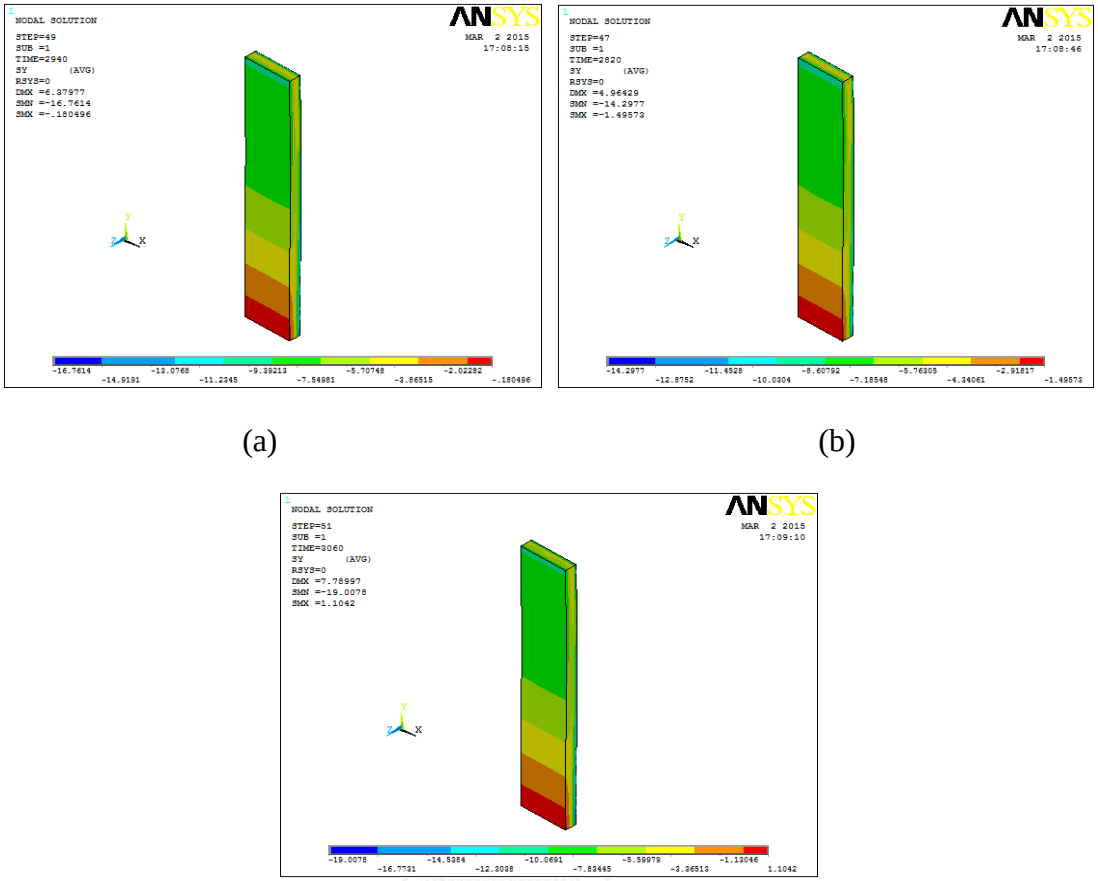

Figure 5.14: Normal stresses along the middle strip of the wall FS for different heating durations: (a) 6 min; (b) 8 min; (c) 10 min.

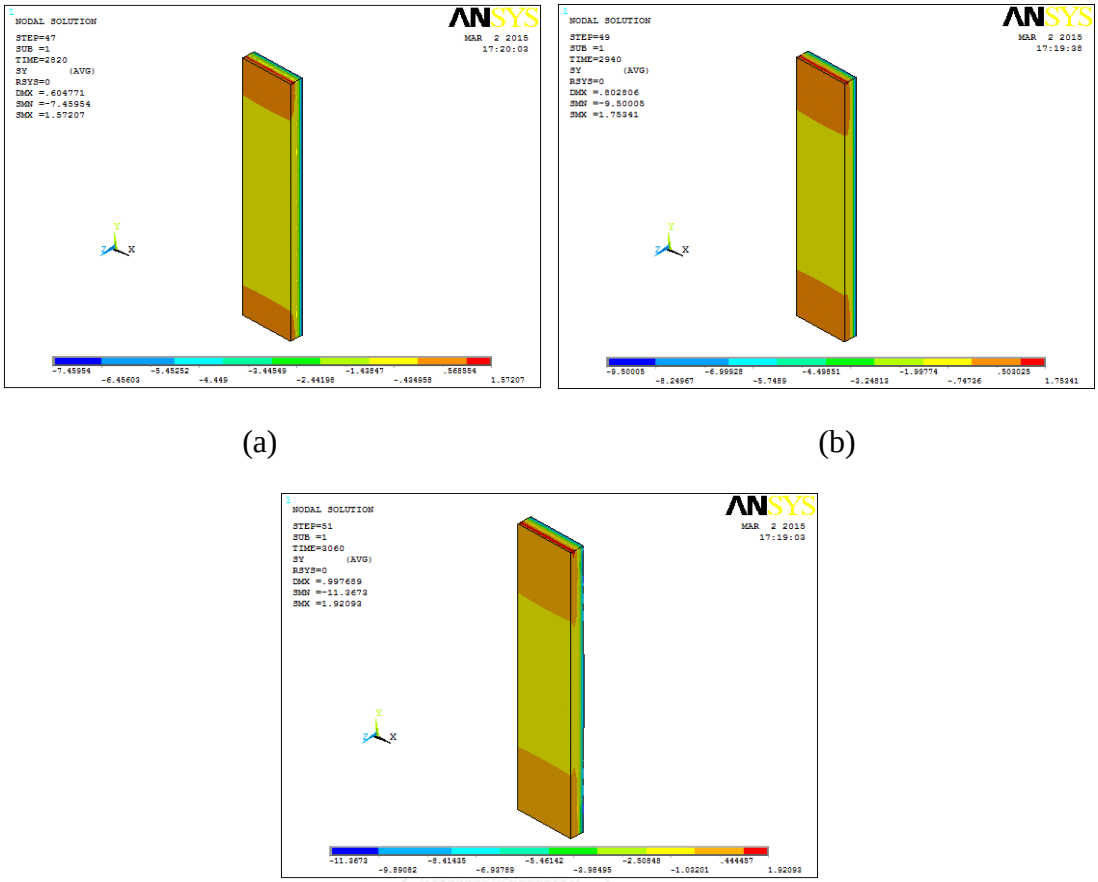

Figure 5.15: Normal stresses along the middle strip of the wall FF for different heating durations: (a) 6 min; (b) 8 min; (c) 10 min.

5.4 Simplified Equations for FRR

In this section, simplified equations are derived for estimating the FRR of the precast concrete load-bearing walls in terms of load levels and slenderness ratios. The least-squares technique is used to determine the best fit of a third-order polynomial function to the dataset of fire resistance ratings obtained from the proposed model with respect to varying load level and slenderness ratio in a specified range. Detailed derivation of the simplified equations can be found in Appendix C.

The effect of varying boundary conditions is also included by examining the simply supported wall (SS), the wall with one end fixed (FS) and the wall with both ends fixed (FF) as presented below. However, to avoid the impact of varying thermal

gradients, the simplified equations are derived only for the wall with a constant thickness of 120 mm. It should also be noted that the simplified equations are developed herein for the wall with the vertical reinforcement ratio of 0.30% and the compressive strength of concrete at normal temperature of 44 MPa. Furthermore, the effect of PP fibers on the thermal and mechanical properties of concrete is not taken into account due to the very small amount of PP fibers (0.05-0.2% by volume) used in the concrete mixture.

5.4.1 Simply Supported Walls (SS)

A series of finite-element analyses have been carried out to obtain the FRR of the simply supported wall with varying height and applied load. The results can be summarized in Table 5.1 and plotted in Figure 5.16. Based on the obtained FRR data, a simplified equation is derived by regarding the load level and the slenderness ratio as independent variables. Note that the load level is computed as the ratio between the applied load and the load-bearing capacity of the wall at normal temperature while the slenderness ratio is determined by simply dividing the wall height by its thickness. Equation (5.1) shows the best-fit third-order polynomial (standard error: 8 min; correlation: 0.98) for wall SS and Figure 5.17 shows the surface plot of the equation compared with the FRR data obtained by using the proposed finite-element model.

$$FRR_{SS} = 1460 - 109S_r - 2560L_r + 4.25S_r^2 + 4080L_r^2 - 0.054S_r^3 - 2170L_r^3 \quad (5.1)$$

in which FRR_{SS} denotes the estimated fire resistance rating (min) for the simply supported wall; S_r denotes the slenderness ratio; and L_r denotes the load ratio, respectively. Note that in the derivation of the simplified equation, the tolerance of the standard error for the FRR estimation is set at 9 min or approximately 5% of the maximum heating duration of 180 min.

Table 5.1 Fire resistance ratings of wall SS as obtained from the finite-element analyses

FRR (min)						
Wall height (m)	**Load (kN)**					
	1000	**1100**	**1200**	**1300**	**1400**	**1500**
2.5	159	132	109	91	75	62
3.0	67	50	40	34	28	24
3.5	30	24	20	17	13	10
4.0	16	12	8	4	3	2

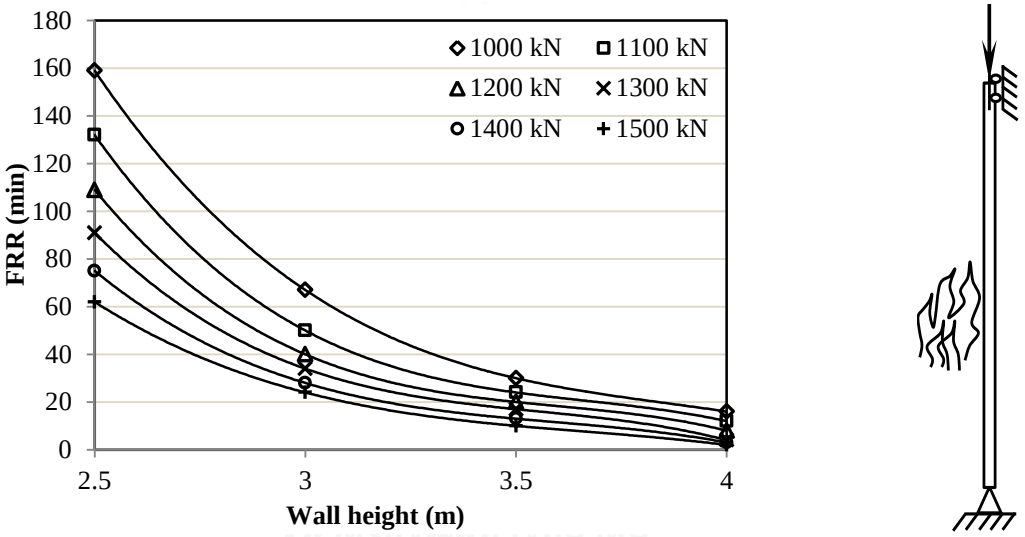

Figure 5.16: FRR of wall SS obtained by using the finite-element model with varying heights and loads.

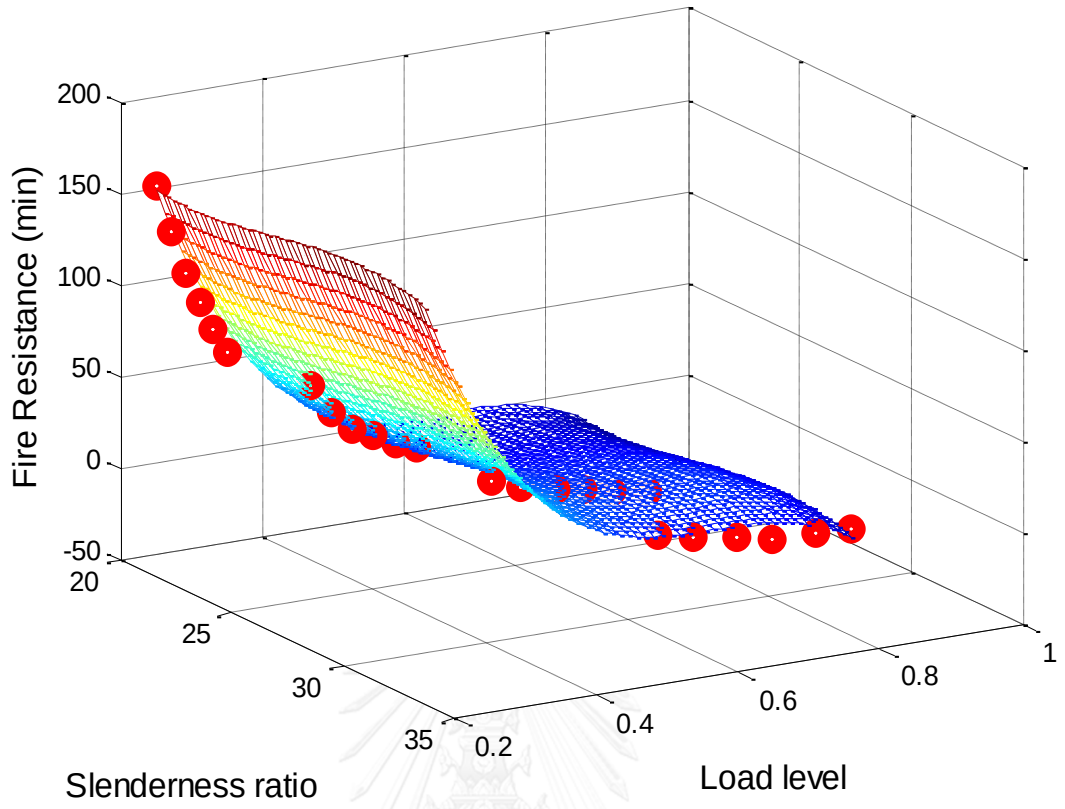

Figure 5.17: Surface plot of the FRR esimating equation for wall SS.

5.4.2 Walls with One End Fixed (FS)

A simplified equation is derived herein for predicting the FRR of precast concrete load-bearing walls with one end fixed. The FRR data obtained from the proposed model that are used in finding the best-fit polynomial are summarized in Table 5.2. The variation of FRR with respect to the applied load and the wall height can be illustrated in Figure 5.18. Based on the least-squares method, the best-fit third-order polynomial can be obtained as

$$FRR_{FS} = 1820 - 137S_r - 2420L_r + 5S_r^2 + 3500L_r^2 - 0.06S_r^3 - 1720L_r^3 \qquad (5.2)$$

Note that the standard error and the correlation provided by the above equation are 9 min and 0.98, respectively. Figure 5.19 shows the surface plot of Eq. (5.2) compared with the FRR data in Table 5.2.

It can be observed that the overall fire resistance rating of the wall with one end fixed is higher compared with the simply supported wall.

Table 5.2 Fire resistance ratings of wall FS as obtained from the finite-element analyses

Fire resistance rating (min)							
Wall height (m)	**Load (kN)**						
	2400	**2500**	**2600**	**2700**	**2800**	**2900**	**3000**
2.5	175	164	153	143	133	124	114
3.0	77	69	61	54	46	42	38
3.5	31	27	24	21	19	17	15
4.0	14	12	9	7	4	3	2

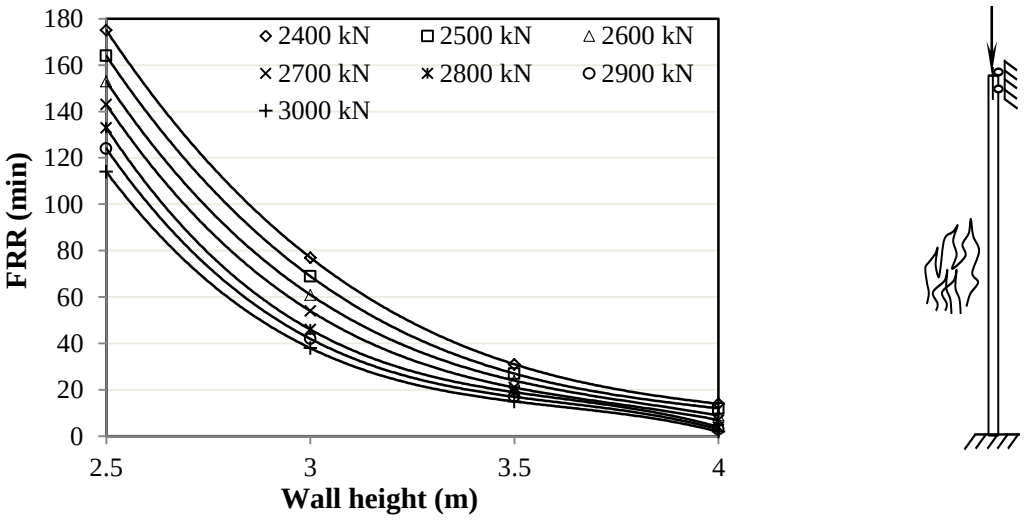

Figure 5.18: FRR of wall FS obtained by using the finite-element model with varying heights and loads.

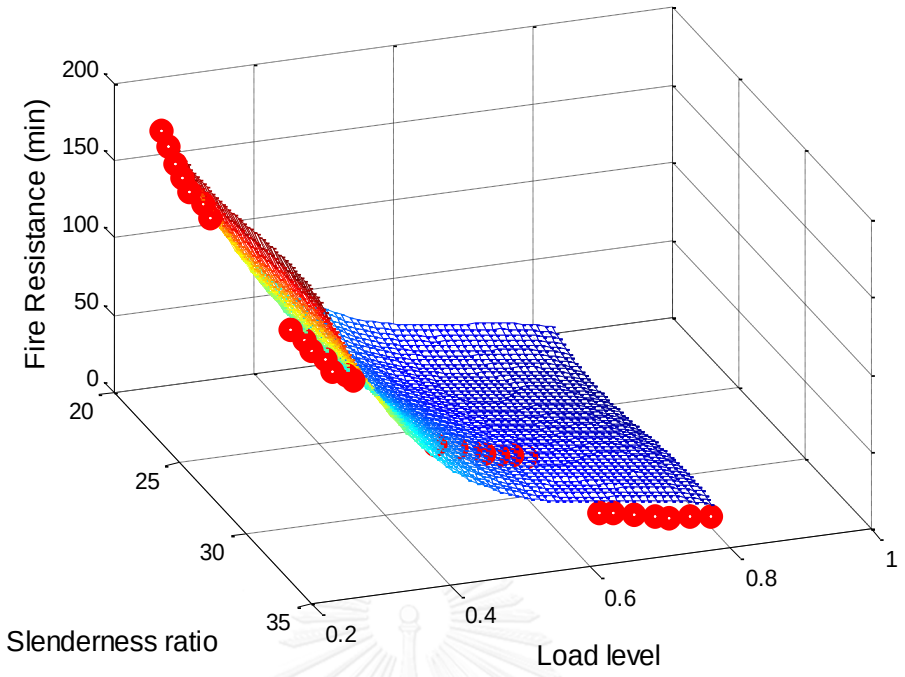

Figure 5.19: Surface plot of the FRR esimating equation for wall FS.

5.4.3 Walls with Both Ends Fixed (FF)

The FRR data for the wall with both ends fixed as obtained from the finite-element analyses are shown in Table 5.3 and plotted in Figure 5.20. The simplified equation for FRR estimation derived based on this dataset can be expressed as

$$FRR_{FF} = 600 - 22S_r - 1370L_r + 0.86S_r^2 + 1700L_r^2 - 0.011S_r^3 - 740L_r^3 \qquad (5.3)$$

The standard error and the correlation estimated by the above equation are 3 min and 0.99, respectively. Figure 5.21 shows the surface plot of Eq. (5.3). It is seen that the wall with both ends fixed provides better fire resistance rating overall compared with the other cases.

Table 5.3 Fire resistance ratings of wall FF as obtained from the finite-element analyses

Fire resistance rating (min)								
Wall height (m)	**Load (kN)**							
	5000	**5200**	**5400**	**5600**	**5800**	**6000**	**6200**	**6400**
2.5	160	152	145	139	133	128	124	120
3.0	98	93	88	84	80	76	72	68
3.5	62	59	55	52	50	47	44	41
4.0	41	38	36	34	32	30	28	26

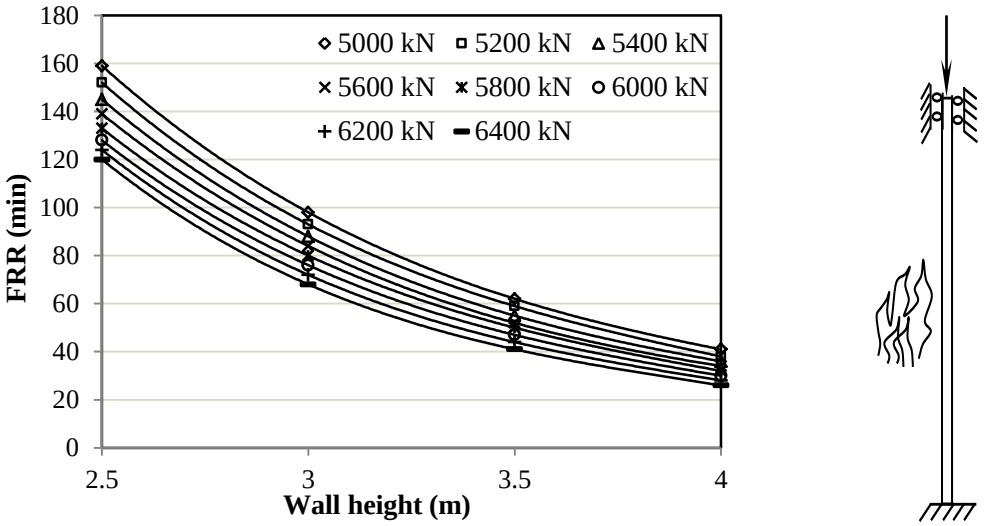

Figure 5.20: FRR of wall FF obtained by using the finite-element model with varying heights and loads.

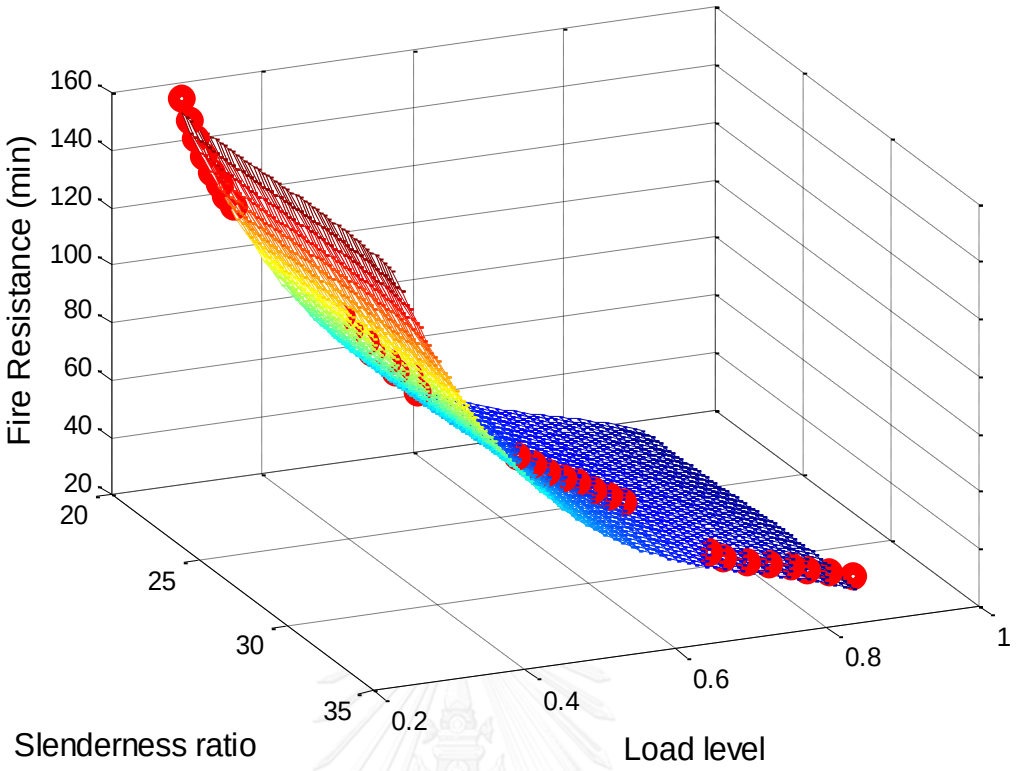

Figure 5.21: Surface plot of the FRR esimating equation for wall FF.

5.5 Effect of Wall Thickness

As mentioned in the previous section, the walls investigated thus far have been specified with a constant thickness of 120 mm to avoid the effect of varying thermal gradients on the overall fire performance. In this section, the wall with a different thickness of 150 mm is examined by maintaining the same slenderness ratios and load levels as for the 120-mm thick wall as shown in Figure 5.22. The fire resistance ratings of the 150-mm thick wall with simple support as obtained from the proposed finite-element model are shown in Table 5.4 and plotted in comparison with the 120-mm thick wall in Figure 5.23 for different slenderness ratios and load levels. It can be seen that for the same load level and slenderness ratio, the 150-mm thick wall shows better fire performance compared with the 120-mm thick wall. This is due to the lower temperature gradient—computed as the maximum deviation between the exposed and unexposed face temperature divided by the wall thickness—of the 150-mm thick wall as illustrated in Figure 5.24. The lower temperature gradient results in

lesser thermal bowing, thereby increasing the fire resistance of the wall. It should also be noted that the simplified equations for the FRR prediction that have been derived in the previous section cannot be used herein due to the effect of varying thermal gradients.

Table 5.4 Fire resistance ratings of the 150-mm thick wall as obtained from the finite-element analyses

S_r	L_r	**FRR (min)**
72	0.32	86
86	0.46	29
100	0.66	12
115	0.82	4

Figure 5.22: Simply supported wall with a thickness of 150 mm.

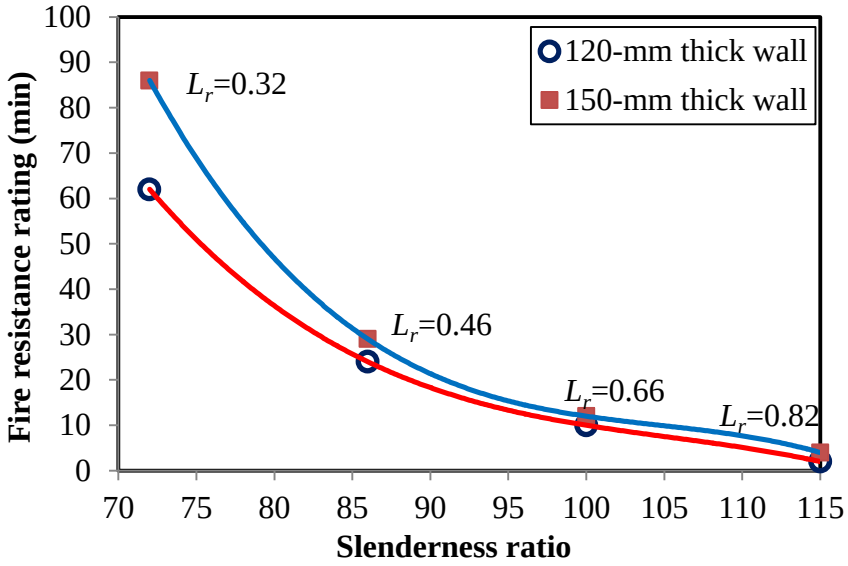

Figure 5.23: Comparison of FRR for the 120-mm and 150-mm thick walls with different slenderness ratios and load levels (L_r).

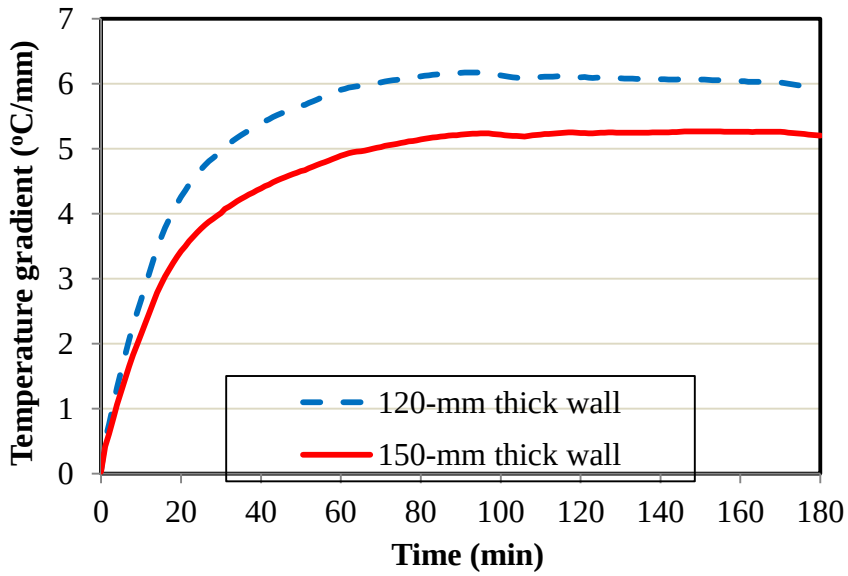

Figure 5.24: Temperature gradients for the 120-mm and 150-mm thick walls.

5.6 Further Capabilities of the Proposed Model

Precast concrete load-bearing walls can be designed with openings (e.g. windows, doors, etc.) or unsymmetrically restrained on the vertical boundaries (e.g. cornered walls). In such applications, the three-dimensional model developed in the current study is deemed advantageous over the two-dimensional models proposed in the literature. In this section, finite-element analyses are carried out to illustrate the capability of the proposed model in handling walls with openings and unsymmetrical restraints as well as to examine the structural behavior of these walls compared with ones without these features.

5.6.1 Walls with Unsymmetrical Boundaries

The wall investigated in this section is specified with the same dimensions as wall W1, but is additionally restrained on one side as shown in Figure 5.25. The lower end of the wall is axially restrained on the nodes along the centroid line against translations in the *x*, *y* and *z* directions to simulate the pinned support. The upper end of the wall is restrained on the nodes along the centroid line from movements in the *x* and *z* directions. Moreover, on the left edge of the wall the nodes along the centroid line are also restrained in the *x* direction as shown in Figure 5.25. The maximum displacement of the wall with the specified boundaries is plotted in comparison with that of the simply supported wall as illustrated in Figure 5.26. It is seen that the maximum horizontal displacement of the wall with unsymmetrical boundaries is reduced by up to 6% compared with the simply supported wall throughout the heating period of 180 min. This indicates that imposing the translational restraint along one vertical edge of the simply supported wall can help reduce the horizontal displacements, and thereby improve the fire performance of the wall.

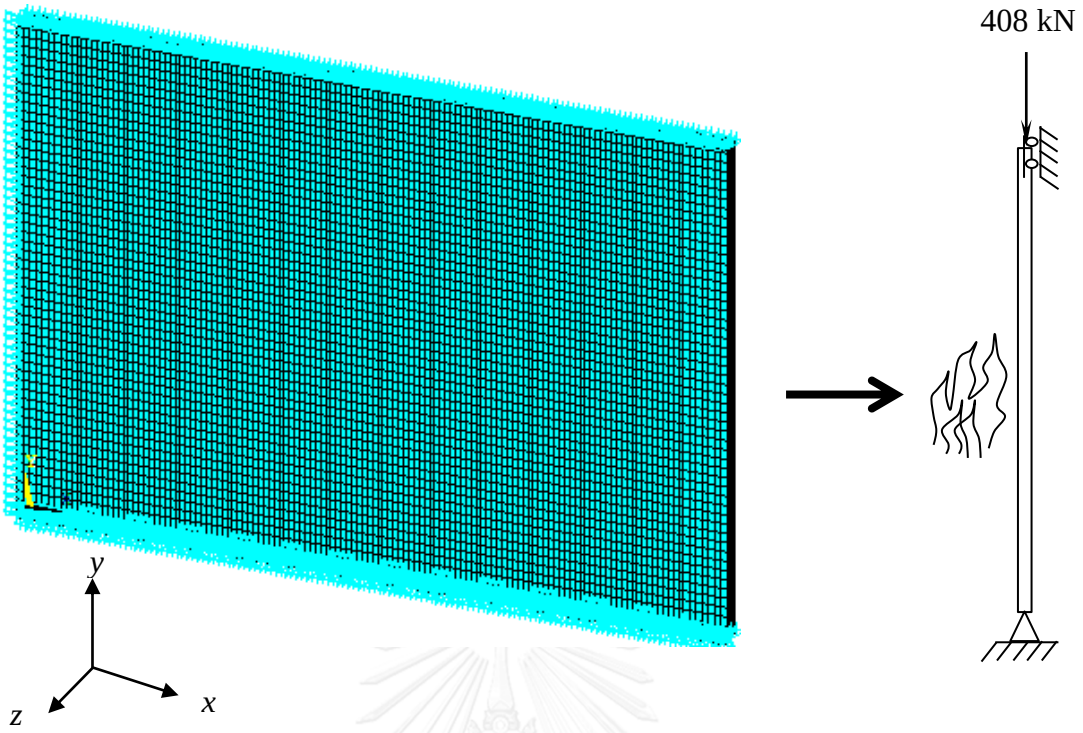

Figure 5.25: Wall with unsymmetrical boundaries.

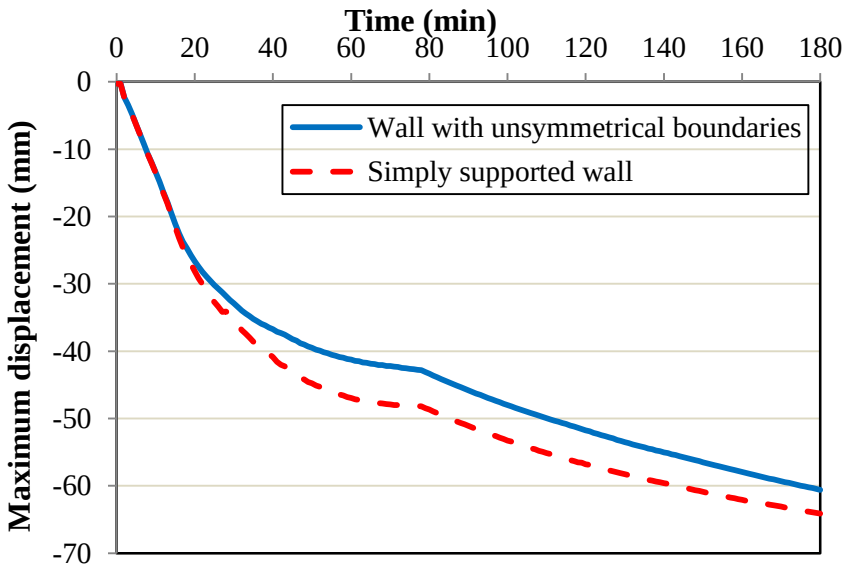

Figure 5.26: Maximum horizontal displacement for the wall with unsymmetrical boundaries and the simply supported wall.

5.6.2 Walls with Openings

The effect of opening on the fire performace of the load-bearing wall exposed to fire on one side is investigated herein. Again, wall W1 is adopted as for the previous section, but is designated with a 1000 × 2000 mm^2 rectangular opening as shown in Figure 5.27. The maximum horizontal displacements of the wall with the specified opening and wall W1 are plotted in Figure 5.28. It can be seen from the figure that the wall opening induces larger horizontal displacements of the wall. The maximum horizontal displacements of the wall with and without opening during the 180-min heating period are 87 and 64 mm, respectively. The larger displacements (by up to 36%) due to the wall opening may lead to a premature failure under higher levels of applied load. It is therefore recommended that the effect of openings with varying configurations on the fire performance of the walls be further investigated in future studies.

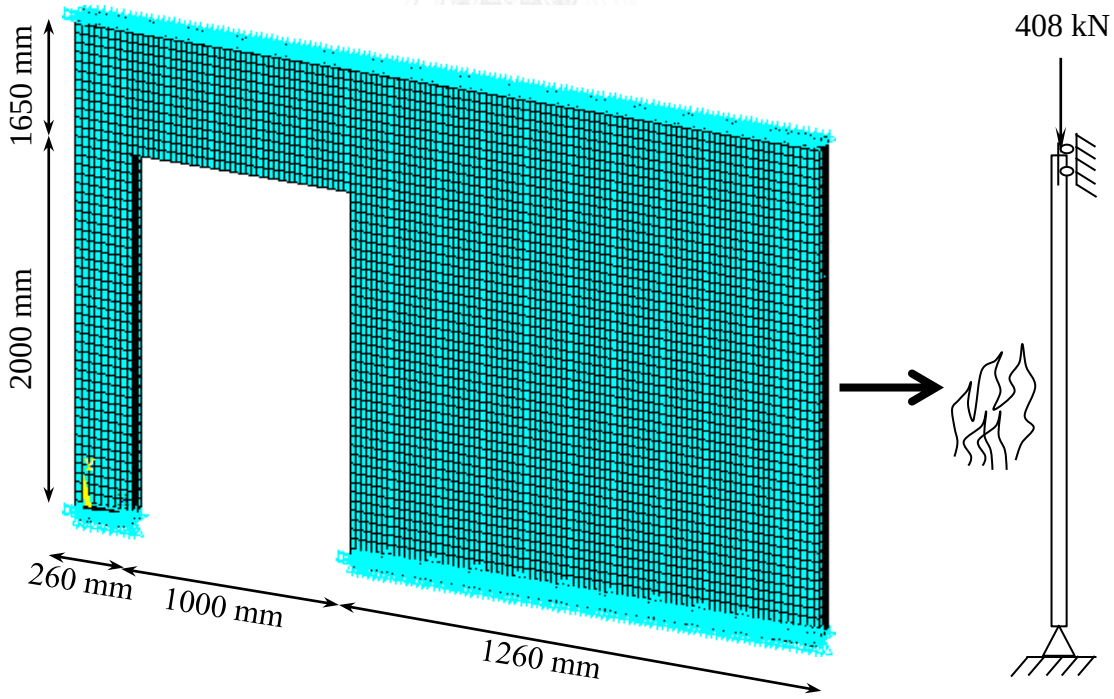

Figure 5.27: Wall with a 1000x2000 mm opening.

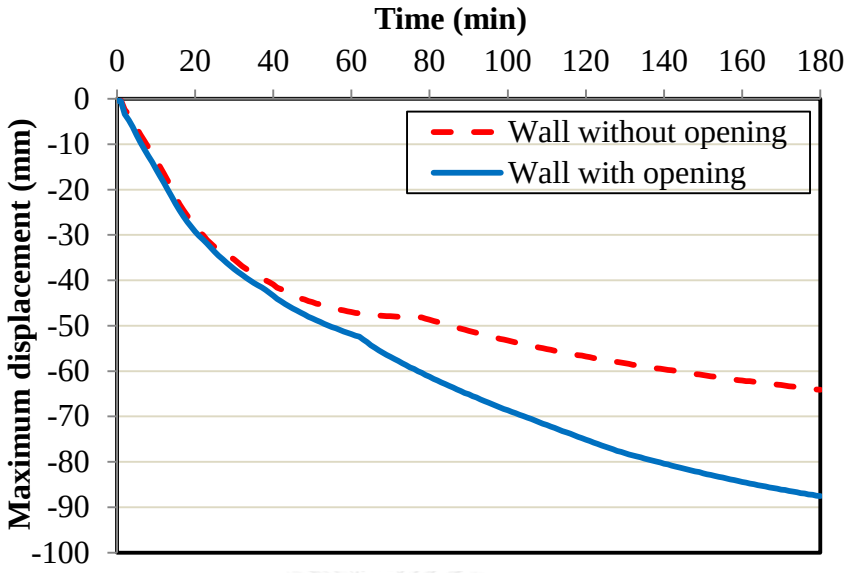

Figure 5.28: Maximum horizontal displacement vs. time curves for the walls with and without opening.

CHAPTER 6
CONCLUSIONS

6.1 Summary

The fire performance of precast concrete load-bearing walls with varying load levels, slenderness ratios and boundary conditions has been investigated by using three-dimensional thermal and structural models. The thermal model is employed to capture the temperature distribution within the wall with respect to time. The temperature history obtained from the thermal model is used as input for the structural model to evaluate displacements, cracking behavior and the structural stability of the walls. The models are capable of taking into account the variation of thermal and mechanical properties of concrete and steel rebar. The models are verified against the experimental data by comparing the predicted temperatures, displacements and crack patterns with the measured ones from the fire test.

Based on the modeling results, it is found that the temperatures predicted by the thermal model are in good agreement with those measured during the fire tests for two wall specimens W1 and W2. The discrepancies between the measured and the predicted temperatures are observed to be in the range from 20 to 50 °C. The temperature deviation may be caused by variation of the actual thermal conductivity and specific heat of concrete from those specified by the Eurocode2 (2004). In order to further examine the validity of the proposed thermal model, the predicted temperatures are compared with the measured temperatures taken from the experimental studies in the literature on reinforced concrete slabs exposed to fire. The maximum deviations are found to be around 35 ^{o}C at the mid-depth and 40 ^{o}C at the unexposed face.

The predicted horizontal displacements are compared with those measured during the fire tests of the walls W1 and W2. It is found that the maximum horizontal displacements of wall W1 as predicted by the structural model match well with the measurements taken throughout the fire test. However, the structural model overestimates the horizontal displacements of wall W2 as compared with the test

results after the first 20 min, with a maximum deviation of around 7 mm. Moreover, the crack patterns of the wall W1 and W2 as obtained from the proposed model are in good agreement with the crack patterns observed during the fire test.

The verified model is used to examine the effects of varying load level, slenderness ratio and boundary condition. The effect of varying load levels is investigated for a simply supported wall with fixed dimensions of 3420 mm in width, 2650 mm in height and 120 mm in thickness. The wall is subject to different values of axial load at the specified load ratios of 0.1, 0.2, 0.3, 0.4 and 0.5. It is found that the fire resistance rating of the load-bearing wall decreases by up to 90% with the increasing load level. This is due to the fact that under the higher load level, larger principal stresses are induced in the concrete elements which lead to earlier crushing failure. The 120-mm thick precast concrete walls with a load ratio exceeding 0.2 are unable to sustain a 3-hour (180 min) fire resistance period.

In order to examine the effect of slenderness ratio on the fire performance of the precast concrete load-bearing wall, the wall thickness and width are specified as 120 mm and 3420 mm, respectively, while the wall height is varied to obtain different slenderness ratios of 20, 25, 30 and 35 as determined by dividing the wall height by its thickness. These walls are subject to a constant axial load of 1000 kN and are exposed to fire on one side. It is found that the walls with higher slenderness ratios are more prone to premature structural failure in which the fire resistance rating decreases by to 93%. The failure of the wall is primarily due to buckling.

In terms of the boundary condition, the rotational restraint is imposed on the wall with fixed dimensions of 3420 mm in width, 2650 mm in height and 120 mm in thickness and applied load of 2500 kN. Three cases are considered herein. In the first case, no rotational restraint is imposed on both ends of the wall (SS). For the second case the rotational restraint is applied at the lower end of the wall (FS). Finally, the rotational restraint is imposed on both ends of the wall as the third case (FF). It can be seen that the rotational restraint has a significant influence on the fire resistance of the load-bearing walls. The modeling results show that wall SS and wall FS fail at 11 min and 129 min, respectively, while wall FF is able to maintain its structural stability throughout the heating period of 180 min. This indicates a 94% increase in the fire

resistance of the load-bearing walls due to the positive effect of rotational restraints through the redistribution of positive and negative moments along the wall height.

To investigate the effect of wall thickness, the wall with a thickness of 150 mm is examined by maintaining the same slenderness ratios and load levels as for the 120-mm thick wall. As compared with the 120-mm thick wall, the 150-mm thick wall shows better fire performance for the same load level and slenderness ratio. This is due to the lower temperature gradient of the 150-mm thick wall, compared with that of the 120-mm thick wall. The lower temperature gradient results in lesser thermal bowing which increases the fire resistance of the wall.

Further capabilities of the proposed models are also presented in the current study. The finite-element analyses are carried out to illustrate the capability of the proposed model in handling walls with openings and unsymmetrical restraints as well as to examine the structural behavior of these walls compared with ones without these features. It is observed that imposing the translational restraint along one vertical edge of the simply supported wall can help reduce the horizontal displacements by up to 6%, and thereby improve the fire performance of the wall. Moreover, the wall with the specified opening shows larger displacements by up to 36%, which may lead to a premature failure under higher levels of the applied load.

6.2 Limitations of the Current Study and Recommendations for Future Research

The model proposed in the current study is capable of taking into account the variation of thermal and mechanical properties of concrete and steel rebar with temperatures, as well as wall's opening and unsymmetrical geometry. Nevertheless, concrete spalling and geometrical imperfection of the wall are not considered in the model. To further enhance the modeling capability, the following potential extensions are suggested:

(1) the modulus of elasticity of the concrete elements where the vapor pressure is higher than the tensile strength may be treated as zero in order to incorporate the effect of concrete spalling (this would require a coupled analysis of the vapor-thermal interactions);

(2) the geometrical imperfection of the wall may be considered by taking into account the eccentricity of the wall once the load is applied.

For the current study a simplified equation has been derived for estimating the fire resistance rating of the wall with only a specific thickness of 120 mm due to the effect of temperature gradient. It is therefore suggested that the method proposed in the current study be used to derive equations for predicting the fire resistance of walls with other thicknesses. Furthermore, because the wall with openings has been identified with more risk of premature failure under higher levels of loads, the effect of opening with varying configurations on the fire performance of the wall should further be investigated.

REFERENCES

American Concrete Institute, ACI 318M-11 Building Code Requirements for Structural Concrete, 2011.

ANSYS (2012a). Mechanical APDL Theory Reference. V. 14.5. Canonsburg (PA).

ANSYS (2012b). Mechanical APDL Element Reference. V. 14.5. Canonsburg (PA).

Aziz, E. and V. Kodur (2013). "An approach for evaluating the residual strength of fire exposed bridge girders." Journal of Constructional Steel Research 88(0): 34-42.

Bazant, Z. P. and J.-C. Chern (1987). "Stress-induced thermal and shrinkage strains in concrete." Journal of engineering mechanics 113(10): 1493-1511.

Bazant, Z. P. and M. F. Kaplan (1996). "Concrete at high temperature: material properties and mathematical models." England: Longman Group Limited.

Buchanan, A. (2001). Structural design for fire safety, West Sussex, England: Wiley.

Cooke, G. and P. Morgan (1988). "Thermal bowing in fire and how it affects building design."

Crozier, D. A. and J. G. Sanjayan (2000). "Tests of load-bearing slender reinforced concrete walls in fire." ACI Structural Journal 97(2).

Cruz, C. R. (1966). "Elastic properties of concrete at high temperatures." Journal of the PCA Research and Development Laboratories 8: 37-45.

Dias, W., G. Khoury and P. Sullivan (1990). "Mechanical properties of hardened cement paste exposed to temperatures up to 700 C (1292 F)." ACI Materials Journal 87(2).

Eurocode2 (2004). Design of concrete structures-Part 1-2: General rules-Structural fire design. European Standards, London. EN BS 1992:1-2.

Eurocode3 (2005). Design of steel structures—Part 1–2: general rules- structural fire design. London (UK): British Standards Institution. BS EN, 1993-1-2.

Fanning, P. (2001). "Nonlinear models of reinforced and post-tensioned concrete beams." Electronic Journal of Structural Engineering 1: 111-119.

Fares, H., S. Remond, A. Noumowe and A. Cousture (2010). "High temperature behaviour of self-consolidating concrete: microstructure and physicochemical properties." Cement and Concrete Research 40(3): 488-496.

Felicetti, R. and P. G. Gambarova (1998). "The effects of high temperature on the residual compressive strength of high-strength siliceous concretes." ACI Materials Journal 95(4).

Franssen, J. M., V. Kodur and R. Zaharia (2009). Designing steel structures for fire safety, CRc Press.

Furumura, F., T. Abe and Y. Shinohara (1995). "Mechanical properties of high strength concrete at high temperatures." in Proceedings of the 4th Weimar Workshop on High Performance Concrete, Material Properties and Design: 237–254.

Go, C.-G., J.-R. Tang, J.-H. Chi, C.-T. Chen and Y.-L. Huang (2012). "Fire-resistance property of reinforced lightweight aggregate concrete wall." Construction and Building Materials 30(0): 725-733.

Guerrieri, M. and S. Fragomeni (2010). Spalling of normal strength concrete walls in fire. Proceedings of the 6th International Conference on Structures in Fire.

Harmathy, T. (1970). "Thermal properties of concrete at elevated temperatures." Journal of Materials.

Harmathy, T. and L. Allen (1973). Thermal properties of selected masonry unit concretes. ACI Journal Proceedings, ACI.

Hawileh, R. A., M. Naser, W. Zaidan and H. A. Rasheed (2009). "Modeling of insulated CFRP-strengthened reinforced concrete T-beam exposed to fire." Engineering Structures 31(12): 3072-3079.

Hawileh, R. A. and M. Z. Naser (2012). "Thermal-stress analysis of RC beams reinforced with GFRP bars." Composites Part B: Engineering 43(5): 2135-2142.

ISO834-1 (1999). Fire Resistance Tests – Elements of Buildings Construction. General Requirements Part-1. International Organization for Standardization, Switzerland.

Khaliq, W. and V. Kodur (2012). "High Temperature Mechanical Properties of High-Strength Fly Ash Concrete with and without Fibers." ACI Materials Journal 109(6).

Khoury, G. (2008). "Concrete spalling assessment methodologies and polypropylene fibre toxicity analysis in tunnel fires." Structural concrete 9(1): 11-18.

Kodur, V. and M. Sultan (2003). "Effect of temperature on thermal properties of high-strength concrete." Journal of materials in civil engineering 15(2): 101-107.

Kodur, V. K. R., M. Naser, P. Pakala and A. Varma (2013). "Modeling the response of composite beam–slab assemblies exposed to fire." Journal of Constructional Steel Research 80(0): 163-173.

Kodur, V. K. R. and M. Sultan (1998). "Thermal properties of high strength concrete at elevated temperatures." ACI SPECIAL PUBLICATIONS 179: 467-480.

Kodur, V. K. R., T. C. Wang and F. P. Cheng (2004). "Predicting the fire resistance behaviour of high strength concrete columns." Cement and Concrete Composites 26(2): 141-153.

Kodur, V. R. and T. Z. Harmathy (2008). Properties of building materials. in SFPE Handbook of Fire Protection Engineering P. J. DiNenno, Ed., , National Fire Protection Association, Quincy, Mass, USA.

Kodur, V. R. and N. Raut (2010). "Performance of concrete structures under fire hazard: emerging trends." The Indian Concrete Journal 84(2): 23–31.

Lee, S. and C. Lee (2013). "Fire resistance of reinforced concrete bearing walls subjected to all-sided fire exposure." Materials and structures 46(6): 943-957.

Li, M., C. Qian and W. Sun (2004). "Mechanical properties of high-strength concrete after fire." Cement and concrete research 34(6): 1001-1005.

Lie, T. and V. Kodur (1996). "Thermal and mechanical properties of steel-fibre-reinforced concrete at elevated temperatures." Canadian Journal of Civil Engineering 23(2): 511-517.

Lie, T. and G. Williams-Leir (1979). "Factors affecting temperature of fire-exposed concrete slabs." Fire and Materials 3(2): 74-79.

Lie, T. T. and V. K. R. Kodur (1995). "Thermal properties of fibre-reinforced concrete at elevated temperatures."

Lim, L. (2000). Stability of precast concrete tilt panels in fire.

Lim, L., A. Buchanan, P. Moss and J.-M. Franssen (2004). "Numerical modelling of two-way reinforced concrete slabs in fire." Engineering structures 26(8): 1081-1091.

Madenci, E. and I. Guven (2007). The finite element method and applications in engineering using ANSYS®, Springer.

Mindess, S., J. F. Young and D. Darwin (2003). Concrete Upper Saddle River, Pearson Education, pp. 94–104.

Noumowe, A. (2005). "Mechanical properties and microstructure of high strength concrete containing polypropylene fibres exposed to temperatures up to 200 C." Cement and Concrete Research 35(11): 2192-2198.

O'Meagher, A. J. and I. D. Bennetts (1991). "Modelling of concrete walls in fire." Fire Safety Journal 17(4): 315-335.

Pantazopoulou, S. and K. Papoulia (2001). "Modeling cover-cracking due to reinforcement corrosion in RC structures." Journal of Engineering Mechanics 127(4): 342-351.

Phan, L. T. (1996). Fire performance of high-strength concrete: A report of the state-of-the art, US Department of Commerce, Technology Administration, National Institute of Standards and Technology, Office of Applied Economics, Building and Fire Research Laboratory.

Rilemtc129-Mht, De La Rilem and P. d. recommandation (1995). "129-MHT: Test Methods for Mechanical Properties of Concrete at High Temperatures." Materials and Structures 28: 410-414.

Schaffer, E. (1992). Structural fire protection, ASCE.

Shin, K.-Y., S.-B. Kim, J.-H. Kim, M. Chung and P.-S. Jung (2002). "Thermo-physical properties and transient heat transfer of concrete at elevated temperatures." Nuclear engineering and design 212(1): 233-241.

Sideris, K. K. (2007). "Mechanical characteristics of self-consolidating concretes exposed to elevated temperatures." Journal of materials in civil engineering 19(8): 648-654.

Tang, W. and T. Lo (2009). "Mechanical and fracture properties of normal-and high-strength concretes with fly ash after exposure to high temperatures." Magazine of Concrete Research 61(5): 323-330.

Tavárez, F. A. (2001). Simulation of behavior of composite grid reinforced concrete beams using explicit finite element methods, University of Wisconsin-Madison.

Van Geem, M. G., J. Gajda and K. Dombrowski (1997). "Thermal properties of commercially available high-strength concretes." Cement, Concrete and Aggregates 19(1).

Willam, K. and E. Warnke (1975). Constitutive model for the triaxial behavior of concrete. Proceedings, International Association for Bridge and Structural Engineering, ISMES, Bergamo, Italy.

Zhu, X. and Y. Chao (2002). "Effects of temperature-dependent material properties on welding simulation." Computers & Structures 80(11): 967-976.

APPENDIX

Appendix A Crushing of Concrete Elements

The failure criterion of concrete due to a multiaxial stress state in accordance with William and Warnke (1975) can be expressed in the form:

$$\frac{P}{f_{c,T}} - F \geq 0 \qquad \text{(A-1)}$$

where:

P is a function of principal stresses (σ_{xp}, σ_{yp}, σ_{zp})

F is the failure surface expressed in terms of principal stresses and other five parameters $f_{ct}, f_{c,T}, f_{cb}, f_1$ and f_2

$f_{c,T}$ is the ultimate compressive strength of concrete

f_{ct} is the tensile strength of concrete

$f_{cb} = 1.2\, f_{c,T}$
$f_1 = 1.45\, f_{c,T}$
$f_2 = 1.725\, f_{c,T}$

The values of f_{cb}, f_1 and f_2 are valid only for stress states where the following condition is satisfied.

$$|\sigma_h| \leq \sqrt{3}\, f_{c,T}$$

where σ_h = hydrostatic stress state $= \dfrac{\sigma_{xp} + \sigma_{yp} + \sigma_{zp}}{3}$

The concrete is assumed to crush when the failure criterion (Eq. A-1) is satisfied and the principal stresses σ_1, σ_2 and σ_3 are less than zero where $\sigma_1 = \max(\sigma_{xp}, \sigma_{yp}, \sigma_{zp})$ and $\sigma_3 = \min(\sigma_{xp}, \sigma_{yp}, \sigma_{zp})$. In this case the function P and the failure surface F are defined as

$$P = \frac{1}{\sqrt{15}}\left[(\sigma_1-\sigma_2)^2+(\sigma_2-\sigma_3)^2+(\sigma_3-\sigma_1)^2\right]^{\frac{1}{2}} \quad \text{(A-2)}$$

$$F = \frac{2R_2(R_2^2-R_1^2)\cos\phi + R_2(2R_1-R_2)\left[4(R_2^2-R_1^2)\cos^2\phi + 5R_1^2 - 4R_1R_2\right]^{\frac{1}{2}}}{4(R_2^2-R_1^2)\cos^2\phi + (R_2-2R_1)^2} \quad \text{(A-3)}$$

where:

$$\cos\phi = \frac{2\sigma_1-\sigma_2-\sigma_3}{\sqrt{2}\left[(\sigma_1-\sigma_2)^2+(\sigma_2-\sigma_3)^2+(\sigma_3-\sigma_1)^2\right]^{\frac{1}{2}}}$$

$$R_1 = \mathrm{a}_0 + \mathrm{a}_1\lambda + \mathrm{a}_3\lambda^2$$

$$R_2 = \mathrm{b}_0 + \mathrm{b}_1\lambda + \mathrm{b}_3\lambda^2$$

$$\lambda = \frac{\sigma_\mathrm{h}}{f_{\mathrm{c,T}}}$$

The angle of similarity ϕ describes the relative magnitude of the failure surface F. When $\phi = 0^\mathrm{o}$, F equals R_1 while if $\phi = 60^\mathrm{o}$, F equals R_2. Therefore, the function R_1 represents the failure surface of all stress states with $\phi = 0^\mathrm{o}$ while the function R_2 represents the failure surface of all stress states with $\phi = 60^\mathrm{o}$ as can be seen in Figure A.1. The function R_1 is determined by adjusting a_0, a_1 and a_2 such that f_{ct}, f_{cb} and f_1 all lie on the failure surface. The value of these coefficients are determined as

$$\begin{bmatrix} 1 & \lambda_\mathrm{t} & \lambda_\mathrm{t}^2 \\ 1 & \lambda_{\mathrm{cb}} & \lambda_{\mathrm{cb}}^2 \\ 1 & \lambda_1 & \lambda_1^2 \end{bmatrix} \begin{Bmatrix} \mathrm{a}_0 \\ \mathrm{a}_1 \\ \mathrm{a}_2 \end{Bmatrix} = \begin{Bmatrix} \frac{P}{f_{\mathrm{c,T}}}(\sigma_1 = f_{\mathrm{ct}}, \sigma_2 = \sigma_3 = 0) \\ \frac{P}{f_{\mathrm{c,T}}}(\sigma_1 = 0, \sigma_2 = \sigma_3 = -f_{\mathrm{cb}}) \\ \frac{P}{f_{\mathrm{c,T}}}(\sigma_1 = -\sigma_\mathrm{h}, \sigma_2 = \sigma_3 = -\sigma_\mathrm{h} - f_1) \end{Bmatrix} \quad \text{(A-4)}$$

with $\lambda_\mathrm{t} = \frac{f_\mathrm{t}}{3f_{\mathrm{c,T}}}, \lambda_{\mathrm{cb}} = -\frac{2f_{\mathrm{cb}}}{3f_{\mathrm{c,T}}}$ and $\lambda_1 = -\frac{\sigma_\mathrm{h}}{f_{\mathrm{c,T}}} - \frac{2f_1}{3f_{\mathrm{c,T}}}$.

The function R_2 is calculated by adjusting b_0, b_1 and b_2 to satisfy the conditions:

$$\begin{bmatrix} 1 & -\frac{1}{3} & \frac{1}{9} \\ 1 & \lambda_2 & \lambda_2^2 \\ 1 & \lambda_0 & \lambda_0^2 \end{bmatrix} \begin{Bmatrix} b_0 \\ b_1 \\ b_2 \end{Bmatrix} = \begin{Bmatrix} \frac{P}{f_{c,T}}(\sigma_1 = f_{ct}, \sigma_2 = \sigma_3 = 0) \\ \frac{P}{f_{c,T}}(\sigma_1 = 0, \sigma_2 = \sigma_3 = -f_{cb}) \\ \frac{P}{f_{c,T}}(\sigma_1 = -\sigma_h, \sigma_2 = \sigma_3 = -\sigma_h - f_1) \end{Bmatrix} \quad \text{(A-5)}$$

with $\lambda_2 = -\frac{\sigma_h}{f_{c,T}} - \frac{f_2}{3 f_{c,T}}$ and λ_0 is a positive root of the equation:

$$R_2(\lambda_0) = a_0 + a_1\lambda_0 + a_2\lambda_0^2 = 0.$$

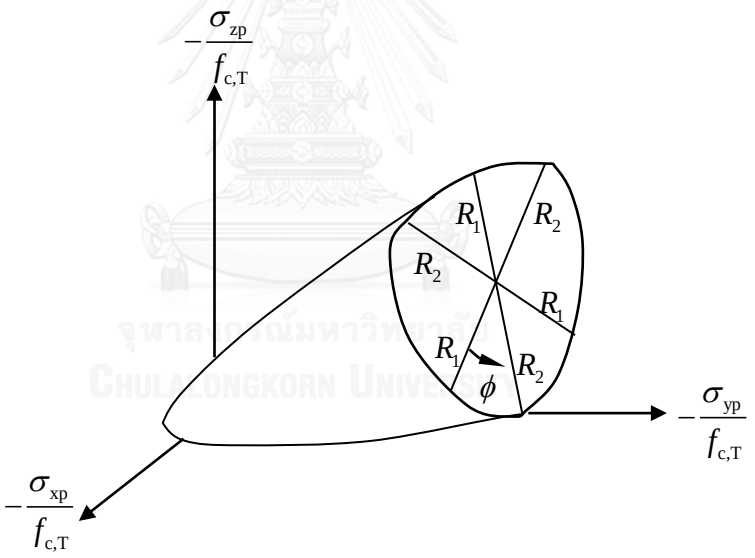

Figure A.1: 3-D failure surface in principal stress space.

As discussed in Chapter 5 (section 5.2), crushing of concrete occurs for the wall with the slenderness ratio of 25, while no crushing is observed for the other two walls with the slenderness ratios of 30 and 35. The failure modes of these walls can be illustrated in Figure A.2.

The wall with the slenderness ratio of 25 shows the principal stresses of $\sigma_3 = 24\,\text{MPa}$, $\sigma_2 = 4\,\text{MPa}$ and $\sigma_1 = 1\,\text{MPa}$. The wall fails at the applied temperature of 800 ^{o}C with the corresponding compressive strength of concrete $f_{c,T} = 11\,\text{MPa}$ and the tensile strength of concete $f_{ct} = 2\,\text{MPa}$. By using the principal stresses in conjunction with the compressive and tensile strength of concrete, the value of *P* can be computed from Eq. (A-2) as 7.9 MPa, while the value of *F* can be computed from Eq. (A-3) as 0.1. This indicates that the failure criterion in Eq. (A-1) is satisfied with the principal stresses σ_1, σ_2 and σ_3 less than zero. It can therefore be concluded that crushing of concrete occurs for the wall with the slenderness ratio of 25 in accordance with the failure criterion of William and Warnke (1975).

Meanwhile, the wall with the slenderness ratio of 30 shows the principal stresses of $\sigma_3 = 23\,\text{MPa}$, $\sigma_2 = 3\,\text{MPa}$ and $\sigma_1 = 0.7\,\text{MPa}$. The wall fails at the applied temperature of 600 ^{o}C with the corresponding compressive strength of concrete $f_{c,T} = 26\,\text{MPa}$ and the tensile strength of concrete $f_{ct} = 3\,\text{MPa}$. The values of *P* and *F* can be obtained as 7.76 MPa and 0.30, respectively; hence, the failure criterion in Eq. (A-1) is not satisfied and crushing of concrete does not occur.

The wall with the slenderness ratio of 35 shows the principal stresses of $\sigma_3 = 22\,\text{MPa}$, $\sigma_2 = 3\,\text{MPa}$ and $\sigma_1 = 0.7\,\text{MPa}$. The wall fails at the applied temperature of 380 ^{o}C with the corresponding compressive strength of concrete $f_{c,T} = 35\,\text{MPa}$ and the tensile strength of concrete $f_{ct} = 3.7\,\text{MPa}$. The value of *P* is obtained as 7.75 MPa, while the value of *F* is 7.38. As such, the failure criterion Eq. (A-1) is not satisfied and the concrete element is deemed not to crush in this case.

Appendix B Calculation of Bending Moment along Wall Height

The bending moments are computed about the center of the cross section of the wall in the middle strip as shown in Figure B.1. The normal stresses at the nodes located along the cross section of the wall on the middle strip are used to compute the bending moments according to the following equation.

$$M = \sum_i M_i = \sum_i \int_{A_i} Z_i \sigma_i dA_i \qquad \text{(B-1)}$$

where

M_i is the bending moment of each layer about the center of the cross section (N.mm)

Z_i is the distance from the center of the cross section to each layer i (mm)

σ_i is the nodal stress at the center of each layer i (MPa)

A_i is the area of each layer i (mm^2)

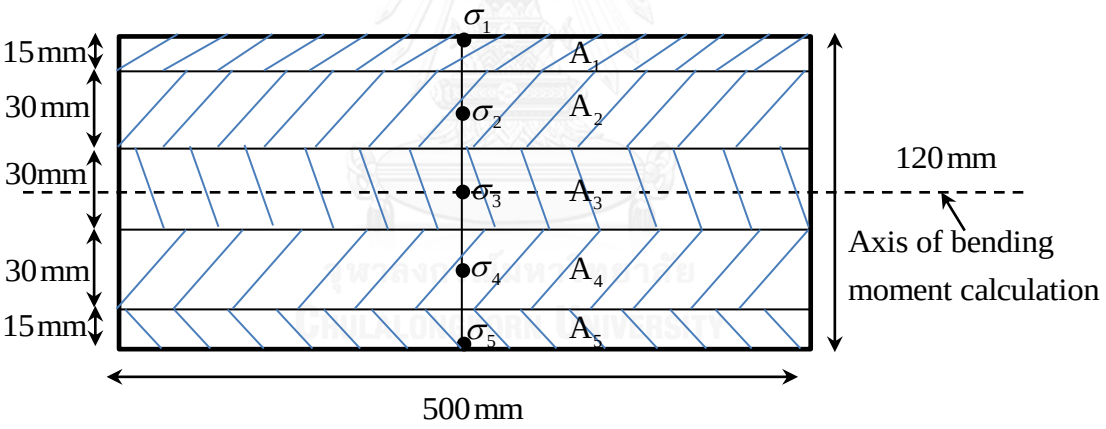

Figure B.1: Nodal stresses along the cross section of the wall on the middle strip.

The calculation of bending moments in the middle strip of wall SS at mid-height for different heating durations are shown below by using the normal stresses along the wall thickness as summarized in Table B.1.

For 6-min heating duration:

$$\begin{aligned} M &= \int_{A_1} Z_1\sigma_1 dA_1 + \int_{A_2} Z_2\sigma_2 dA_2 + \int_{A_4} Z_4\sigma_4 dA_4 + \int_{A_5} Z_5\sigma_5 dA_5 \\ &= (52.5\times 0.31\times 15\times 500) + (30\times 0.08\times 30\times 500) + (30\times 9.81\times 30\times 500) \\ &\quad + (52.5\times 16.33\times 15\times 500) \\ &= 11.01\,\text{kN.m} \end{aligned}$$

For 8-min heating duration:

$$\begin{aligned} M &= \int_{A_1} Z_1\sigma_1 dA_1 + \int_{A_2} Z_2\sigma_2 dA_2 + \int_{A_4} Z_4\sigma_4 dA_4 + \int_{A_5} Z_5\sigma_5 dA_5 \\ &= (52.5\times 3.19\times 15\times 500) + (30\times 0.12\times 30\times 500) + (30\times 9.55\times 30\times 500) \\ &\quad + (52.5\times 19.75\times 15\times 500) \\ &= 13.38\,\text{kN.m} \end{aligned}$$

For 10-min heating duration:

$$\begin{aligned} M &= \int_{A_1} Z_1\sigma_1 dA_1 + \int_{A_2} Z_2\sigma_2 dA_2 + \int_{A_4} Z_4\sigma_4 dA_4 + \int_{A_5} Z_5\sigma_5 dA_5 \\ &= (52.5\times 7.83\times 15\times 500) + (30\times 0.22\times 30\times 500) + (30\times 5.28\times 30\times 500) \\ &\quad + (52.5\times 23.49\times 15\times 500) \\ &= 14.81\,\text{kN.m} \end{aligned}$$

The bending moment calculations at the lower end of the middle strip of wall FS for different heating durations are shown below. Note that the normal stresses along the wall thickness used for the calculations are taken from Table B.2.

For 6-min heating duration:

$$\begin{aligned} M &= \int_{A_1} Z_1\sigma_1 dA_1 + \int_{A_2} Z_2\sigma_2 dA_2 + \int_{A_4} Z_4\sigma_4 dA_4 + \int_{A_5} Z_5\sigma_5 dA_5 \\ &= -(52.5\times 14.29\times 15\times 500) - (30\times 5.11\times 30\times 500) + (30\times 3.59\times 30\times 500) \\ &\quad + (52.5\times 1.68\times 15\times 500) \\ &= -5.65\,\text{kN.m} \end{aligned}$$

For 8-min heating duration:

$$\begin{aligned} M &= \int_{A_1} Z_1\sigma_1 dA_1 + \int_{A_2} Z_2\sigma_2 dA_2 + \int_{A_4} Z_4\sigma_4 dA_4 + \int_{A_5} Z_5\sigma_5 dA_5 \\ &= -(52.5\times 16.76\times 15\times 500) - (30\times 4.73\times 30\times 500) + (30\times 3.87\times 30\times 500) \\ &\quad + (52.5\times 0.26\times 15\times 500) \\ &= -6.88\,\text{kN.m} \end{aligned}$$

For 10-min heating duration:

$$\begin{aligned} M &= \int_{A_1} Z_1\sigma_1 dA_1 + \int_{A_2} Z_2\sigma_2 dA_2 + \int_{A_4} Z_4\sigma_4 dA_4 + \int_{A_5} Z_5\sigma_5 dA_5 \\ &= -(52.5\times 19\times 15\times 500) - (30\times 6.35\times 30\times 500) + (30\times 1.75\times 30\times 500) \\ &\quad - (52.5\times 0.91\times 15\times 500) \\ &= -9.91\,\text{kN.m} \end{aligned}$$

Based on the normal stresses along the wall thickness in Table B.3, the bending moments in the middle strip of wall FF at the lower end can be computed for different heating durations as follows.

For 6-min heating duration:

$$\begin{aligned} M &= \int_{A_1} Z_1\sigma_1 dA_1 + \int_{A_2} Z_2\sigma_2 dA_2 + \int_{A_4} Z_4\sigma_4 dA_4 + \int_{A_5} Z_5\sigma_5 dA_5 \\ &= -(52.5\times 7.88\times 15\times 500) - (30\times 1.89\times 30\times 500) - (30\times 0.43\times 30\times 500) \\ &\quad - (52.5\times 0.60\times 15\times 500) \\ &= -4.39\,\text{kN.m} \end{aligned}$$

For 8-min heating duration:

$$\begin{aligned} M &= \int_{A_1} Z_1\sigma_1 dA_1 + \int_{A_2} Z_2\sigma_2 dA_2 + \int_{A_4} Z_4\sigma_4 dA_4 + \int_{A_5} Z_5\sigma_5 dA_5 \\ &= -(52.5\times 10.11\times 15\times 500) - (30\times 2.55\times 30\times 500) - (30\times 0.66\times 30\times 500) \\ &\quad - (52.5\times 0.89\times 15\times 500) \\ &= -5.78\,\text{kN.m} \end{aligned}$$

For 10-min heating duration:

$$\begin{aligned} M &= \int_{A_1} Z_1\sigma_1 dA_1 + \int_{A_2} Z_2\sigma_2 dA_2 + \int_{A_4} Z_4\sigma_4 dA_4 + \int_{A_5} Z_5\sigma_5 dA_5 \\ &= -(52.5\times 12.18\times 15\times 500) - (30\times 3.24\times 30\times 500) - (30\times 0.86\times 30\times 500) \\ &\quad - (52.5\times 1.16\times 15\times 500) \\ &= -7.10\,\text{kN.m} \end{aligned}$$

Table B.1 Normal stresses along the thickness of wall SS at mid-height for different heating durations

Distance from exposed face (mm)	**Normal stresses for different heating durations (MPa)**		
	Stress at 6 min	**Stress at 8 min**	**Stress at 10 min**
0	0.31	3.19	7.83
30	0.08	0.12	0.22
60	-5.07	-4.94	-5.19
90	-9.81	-9.55	-5.28
120	-16.33	-19.75	-23.49

Table B.2 Normal stresses along the thickness of wall FS at lower end for different heating durations

Distance from exposed face (mm)	**Normal stresses for different heating durations (MPa)**		
	Stress at 6 min	**Stress at 8 min**	**Stress at 10 min**
0	-14.29	-16.76	-19.00
30	-5.11	-4.73	-6.35
60	-4.09	-4.18	-3.36
90	-3.59	-3.87	-1.75
120	-1.68	-0.26	0.91

Table B.3 Normal stresses along the thickness of wall FF at lower end for different heating durations

Distance from exposed face (mm)	**Normal stresses for different heating durations (MPa)**		
	Stress at 6 min	**Stress at 8 min**	**Stress at 10 min**
0	-7.88	-10.11	-12.18
30	-1.89	-2.55	-3.24
60	0.43	0.15	0.18
90	0.43	0.66	0.86
120	0.60	0.89	1.16

Appendix C Simplified Equations for Fire Resistance Rating (FRR)

A third-order polynomial function is used to estimate the fire resistance ratings (*FRR*) of the walls in terms of load ratio (L_r) and slenderness ratio (S_r) in accordance with Eq. (C-1)$\left[FRR = a_o + a_1 S_r + a_2 L_r + a_3 S_r^2 + a_4 L_r^2 + a_5 S_r^3 + a_6 L_r^3 \quad \text{(C-1)} \right]$. The least-squares technique is used to determine the best-fit polynomial to the *FRR* data obtained from the proposed model by minimizing the sum of squared residuals (S_e) between the predicted and the actual *FRR* data as defined by the following expressions. The standard error ($S_{y/x}$) and the correlation coefficient (r) estimated by Eq. (C-1) are determined by using Eq. (C-4) and Eq. (C-5), respectively.

$$S_e = \sum (FRR_i - a_o - a_1 S_{r,i} - a_2 L_{r,i} - a_3 S_{r,i}^2 - a_4 L_{r,i}^2 - a_5 S_{r,i}^3 - a_6 L_{r,i}^3)^2 \qquad \text{(C-2)}$$

Minimize total squared error:

$$\begin{cases} \frac{\partial S_e}{\partial a_o} = 0 \Rightarrow -2\sum (FRR_i - a_o - a_1 S_{r,i} - a_2 L_{r,i} - a_3 S_{r,i}^2 - a_4 L_{r,i}^2 - a_5 S_{r,i}^3 - a_6 L_{r,i}^3) = 0 \\ \frac{\partial S_e}{\partial a_1} = 0 \Rightarrow -2\sum S_{r,i} (FRR_i - a_o - a_1 S_{r,i} - a_2 L_{r,i} - a_3 S_{r,i}^2 - a_4 L_{r,i}^2 - a_5 S_{r,i}^3 - a_6 L_{r,i}^3) = 0 \\ \frac{\partial S_e}{\partial a_2} = 0 \Rightarrow -2\sum L_{r,i} (FRR_i - a_o - a_1 S_{r,i} - a_2 L_{r,i} - a_3 S_{r,i}^2 - a_4 L_{r,i}^2 - a_5 S_{r,i}^3 - a_6 L_{r,i}^3) = 0 \\ \frac{\partial S_e}{\partial a_3} = 0 \Rightarrow -2\sum S_{r,i}^2 (FRR_i - a_o - a_1 S_{r,i} - a_2 L_{r,i} - a_3 S_{r,i}^2 - a_4 L_{r,i}^2 - a_5 S_{r,i}^3 - a_6 L_{r,i}^3) = 0 \\ \frac{\partial S_e}{\partial a_4} = 0 \Rightarrow -2\sum L_{r,i}^2 (FRR_i - a_o - a_1 S_{r,i} - a_2 L_{r,i} - a_3 S_{r,i}^2 - a_4 L_{r,i}^2 - a_5 S_{r,i}^3 - a_6 L_{r,i}^3) = 0 \\ \frac{\partial S_e}{\partial a_5} = 0 \Rightarrow -2\sum S_{r,i}^3 (FRR_i - a_o - a_1 S_{r,i} - a_2 L_{r,i} - a_3 S_{r,i}^2 - a_4 L_{r,i}^2 - a_5 S_{r,i}^3 - a_6 L_{r,i}^3) = 0 \\ \frac{\partial S_e}{\partial a_6} = 0 \Rightarrow -2\sum L_{r,i}^3 (FRR_i - a_o - a_1 S_{r,i} - a_2 L_{r,i} - a_3 S_{r,i}^2 - a_4 L_{r,i}^2 - a_5 S_{r,i}^3 - a_6 L_{r,i}^3) = 0 \end{cases}$$

$$\Rightarrow \begin{bmatrix} n & \sum_{i=1}^{n} S_{r,i} & \sum_{i=1}^{n} L_{r,i} & \sum_{i=1}^{n} S_{r,i}^2 & \sum_{i=1}^{n} L_{r,i}^2 & \sum_{i=1}^{n} S_{r,i}^3 & \sum_{i=1}^{n} L_{r,i}^3 \\ \sum_{i=1}^{n} S_{r,i} & \sum_{i=1}^{n} S_{r,i}^2 & \sum_{i=1}^{n} S_{r,i}L_{r,i} & \sum_{i=1}^{n} S_{r,i}^3 & \sum_{i=1}^{n} S_{r,i}L_{r,i}^2 & \sum_{i=1}^{n} S_{r,i}^4 & \sum_{i=1}^{n} S_{r,i}L_{r,i}^3 \\ \sum_{i=1}^{n} L_{r,i} & \sum_{i=1}^{n} S_{r,i}L_{r,i} & \sum_{i=1}^{n} L_{r,i}^2 & \sum_{i=1}^{n} S_{r,i}^2L_{r,i} & \sum_{i=1}^{n} L_{r,i}^3 & \sum_{i=1}^{n} S_{r,i}^3L_{r,i} & \sum_{i=1}^{n} L_{r,i}^4 \\ \sum_{i=1}^{n} S_{r,i}^2 & \sum_{i=1}^{n} S_{r,i}^3 & \sum_{i=1}^{n} S_{r,i}^2L_{r,i} & \sum_{i=1}^{n} S_{r,i}^4 & \sum_{i=1}^{n} S_{r,i}^2L_{r,i}^2 & \sum_{i=1}^{n} S_{r,i}^5 & \sum_{i=1}^{n} S_{r,i}^2L_{r,i}^3 \\ \sum_{i=1}^{n} L_{r,i}^2 & \sum_{i=1}^{n} S_{r,i}L_{r,i}^2 & \sum_{i=1}^{n} L_{r,i}^4 & \sum_{i=1}^{n} S_{r,i}^2L_{r,i}^2 & \sum_{i=1}^{n} S_{r,i}^4 & \sum_{i=1}^{n} S_{r,i}^3L_{r,i}^2 & \sum_{i=1}^{n} L_{r,i}^5 \\ \sum_{i=1}^{n} S_{r,i}^3 & \sum_{i=1}^{n} S_{r,i}^4 & \sum_{i=1}^{n} S_{r,i}^3L_{r,i} & \sum_{i=1}^{n} S_{r,i}^5 & \sum_{i=1}^{n} S_{r,i}^3L_{r,i}^2 & \sum_{i=1}^{n} S_{r,i}^6 & \sum_{i=1}^{n} S_{r,i}^3L_{r,i}^3 \\ \sum_{i=1}^{n} L_{r,i}^3 & \sum_{i=1}^{n} S_{r,i}L_{r,i}^3 & \sum_{i=1}^{n} L_{r,i}^4 & \sum_{i=1}^{n} S_{r,i}^2L_{r,i}^3 & \sum_{i=1}^{n} L_{r,i}^5 & \sum_{i=1}^{n} S_{r,i}^3L_{r,i}^3 & \sum_{i=1}^{n} L_{r,i}^6 \end{bmatrix} \begin{Bmatrix} a_o \\ a_1 \\ a_2 \\ a_3 \\ a_4 \\ a_5 \\ a_6 \end{Bmatrix} = \begin{Bmatrix} \sum_{i=1}^{n} FRR_i \\ \sum_{i=1}^{n} S_{r,i}FRR_i \\ \sum_{i=1}^{n} L_{r,i}FRR_i \\ \sum_{i=1}^{n} S_{r,i}^2FRR_i \\ \sum_{i=1}^{n} L_{r,i}^2FRR_i \\ \sum_{i=1}^{n} S_{r,i}^3FRR_i \\ \sum_{i=1}^{n} L_{r,i}^3FRR_i \end{Bmatrix} \quad \text{(C-3)}$$

$$S_{y/x} = \sqrt{\frac{S_e}{n-(m+1)}} \quad \text{(C-4)}$$

where n is the number of observations (number of data points) and m is the number of polynomail order

$$r = \sqrt{\frac{S_t - S_e}{S_t}} \quad \text{(C-5)}$$

where S_t is defined as

$$S_t = \sum_{i=1}^{n} \left(FRR_i - \overline{FRR_i} \right)^2 ; \overline{FRR_i} = \frac{1}{n} \sum_{i=1}^{n} FRR_i \quad \text{(C-6)}$$

The *FRR* data for wall SS as obtained from the proposed model with respect to varying load levels and slenderness ratios are shown in Table C.1. Based on the data from Table C.1, the coefficients a_0, a_1, a_2, a_3, a_4, a_5 and a_6 can be determined from Eq. C-3 as 1460,-109, -2560, 4.25, 4080,-0.054 and -2170, respectively. Hence, the simplified equation for estimating the fire resistance rating of wall SS can be written as

$$FRR_{SS} = 1460 - 109S_r - 2560L_r + 4.25S_r^2 + 4080L_r^2 - 0.054S_r^3 - 2170L_r^3 \quad \text{(C-7)}.$$

The standard error ($S_{y/x}$) obtained from Eq. (C-4) by substituting n = 24 and m = 3 is found to be 8 min, while the correlation coefficient (r) computed from Eq. (C-5) is 0.98.

Table C.2 shows the *FRR* data for wall FS as obtained from the proposed model with respect to varying load levels and slenderness ratios. By substituting the data from Table C.2 in Eq. (C-3), the coefficients a_0, a_1, a_2, a_3, a_4, a_5 and a_6 can be

determined as 1820, -137, -2420, 5, 3500, -0.06 and -1720, respectively. Hence, the simplified equation for estimating the fire resistance rating of wall FS can be written as

$$FRR_{FS} = 1820 - 137S_r - 2420L_r + 5S_r^2 + 3500L_r^2 - 0.06S_r^3 - 1720L_r^3 \quad \text{(C-8)}$$

By substituting n = 28 and m = 3 into Eq. (C-4), the standard error ($S_{y/x}$) is found to be 9 min, while the correlation coefficient (r) obtained from Eq. (C-5) is 0.98.

Table C.3 shows *FRR* data for wall FF as obtained from the proposed model. Based on the data in Table C.3, the coefficients a_0, a_1, a_2, a_3, a_4, a_5 and a_6 can be determined from Eq. (C-3) as 600, -22, 1370, 0.86, 1700, -0.011 and -740, respectively. The simplified equation for estimating the fire resistance rating of wall FS can be written as

$$FRR_{FF} = 600\text{-}22S_r\text{-}1370L_r + 0.86S_r^2 + 1700L_r^2\text{-}0.011S_r^3\text{-}740L_r^3 \quad \text{(C-9)}$$

The standard error ($S_{y/x}$) computed from Eq. (C-4) by substituting n = 32 and m = 3 is 3 min, while the correlation coefficient (r) obtained from Eq. (C-5) is 0.99.

Table C.1 *FRR* of wall SS as obtained from the finite-element analyses

S_r	L_r	***FRR* (min)**
21	0.22	159
	0.24	132
	0.26	109
	0.28	91
	0.3	75
	0.32	62
25	0.31	67
	0.34	50
	0.37	40
	0.4	34
	0.43	28
	0.46	24
29	0.44	30
	0.48	24
	0.53	20
	0.57	17
	0.61	13
	0.66	10
33	0.55	16
	0.6	12
	0.66	8
	0.71	4
	0.77	3
	0.82	2

Table C.2 *FRR* of wall FS as obtained from the finite-element analyses

S_r	L_r	*FRR (min)*
21	0.25	175
	0.26	164
	0.27	153
	0.28	143
	0.3	133
	0.31	124
	0.32	114
25	0.36	77
	0.38	69
	0.39	61
	0.41	54
	0.42	46
	0.44	42
	0.46	38
29	0.5	31
	0.52	27
	0.54	24
	0.56	21
	0.58	19
	0.6	17
	0.62	15
33	0.65	14
	0.67	12
	0.7	9
	0.73	7
	0.76	4
	0.78	3
	0.81	2

Table C.3 *FRR* of wall FF as obtained from the finite-element analyses

S_r	L_r	*FRR (min)*
21	0.27	160
	0.28	152
	0.29	145
	0.30	139
	0.31	133
	0.32	128
	0.33	124
	0.34	120
25	0.39	98
	0.40	93
	0.42	88
	0.43	84
	0.45	80
	0.46	76
	0.48	74
	0.49	68
29	0.53	62
	0.55	59
	0.57	55
	0.59	52
	0.61	50
	0.63	47
	0.65	44
	0.67	41
33	0.69	41
	0.71	38
	0.74	36
	0.77	34
	0.80	32
	0.82	30
	0.85	28
	0.88	26

VITA

The author, Mr. Soklin Chou, was born in Kandal province, Cambodia in 1982. He graduated Bachelor's degree in Rural Engineering at Institute of Technology of Cambodia in 2009 and Master's degree in Materials and Mineral Resources Engineering in 2011 at Universiti Sains Malaysia. He has been granted the scholarship by AUN/SEED-Net to study PhD degree in the field of Structural Engineering, Department of Civil Engineering, Chulalongkorn University under the supervision of Associate Professor Dr. Thanyawat Pothisiri. During studying PhD degree, he had conducted a research work at Tokyo Institute of Technology (TIT) from August 2013 to March 2014 under the supervision of Associate Professor Dr. Anil C. Wijeyewickrema.